Development of novel *Staphylococcus aureus* biofilm treatment: A biomaterials approach to delay antibiotic tolerance and inhibit bacterial-mediated bone destruction

By

Thomas Joseph Spoonmore

Dissertation

Submitted to the Faculty of the
Graduate School of Vanderbilt University
in partial fulfillment of the requirements
for the degree of

DOCTOR OF PHILOSOPHY

in

Chemical and Biomolecular Engineering
May 31, 2020
Nashville, Tennessee

Approved:
Dr. Scott A. Guelcher, Ph.D.
Dr. James E. Cassat, M.D., Ph.D.
Dr. Ethan S. Lippmann, Ph.D.
Dr. John T. Wilson, Ph.D.

ACKNOWLEDGEMENTS

As I drafted this dissertation, I was overwhelmed with the number of people that contributed to my project, provided guidance, and offered support. I'd like to first extend my sincerest gratitude to Dr. Scott Guelcher and Dr. Jim Cassat for their leadership. Scott has stuck with me through a rigorous project and supported my curiosity in the microbiology field for over 5 years. Through his mentorship, I have felt comfortable accenting my strengths to collaborate and ask questions to those who have expertise outside of our own. To say that Jim has been a valuable resource would be an understatement. As an engineer, I am frequently overzealous and tend to chase solutions beyond my control. Jim has been very patient with me and coached me to be a better researcher, all while supporting my desire to develop something impossible. I am forever indebted to both of these great researchers. I would also like to thank the members of my Ph.D. committee: Dr. Ethan Lippmann and Dr. John Wilson. Their counsel and insights were invaluable in improving the content, impact, and direction of this work. I believe that the guidance that I have received from these mentors will serve me well in the next chapter of my career.

Thank you as well to the Guelcher laboratory, especially Katarzyna Zienkiewicz, who has been invaluable in maintaining the laboratory, providing mentorship, and incredible assistance with experiments. I'd also like to thank all of the current and former members of the Guelcher lab: Dr. Drew Harmata, Dr. Ushashi Dadwal, Dr. Anne Talley, Dr. Ruijing Guo, Dr. Sichang Lu, Dr. Madison McGough, Dr. Joseph Vanderburgh, Dr. Shanik Fernando, Cody Dykes, Dustin Groff, David Florian, Greg Lowen, and Lauren Boller for all of their support and comradery over the past 5 years. It was a pleasure working with this impressive group of individuals. I would also like to thank the undergraduate students that worked with me during my time at Vanderbilt: Hannah Kang, Patrick Gerber, and Mariah Arral. Working with these undergraduate students was truly a

rewarding process that I enjoyed thoroughly.

This work was highly collaborative and I would like to specifically thank the Cassat lab for their contribution. Thank you to Dr. Aimee Potter, Dr. Nicole Putnam, Jacob Curry, Laura Fulbright, Caleb Ford, Casey Butrico, Jenna Petronglo, Chris Peek, Theresa Torres, Virginia Cruz, Andrew Hendrix, and Daniel Markwalter for their teamwork, acceptance, and support of this work. Aimee and Niki were instrumental in my initial microbiology training and helped set the groundwork for this dissertation. I would specifically like to thank Caleb Ford for being an incredible teammate and friend. I believe that all researchers ask themselves difficult questions at difficult times. I had asked myself if continuing the pursuit of this degree was worth it and had become very discouraged by the middle of 2018. I decided to give a collaborative project with Caleb my full effort to decide if I wanted to continue in this career path. I wouldn't have gotten here without this partnership.

I would also like to thank all of the people and facilities that supported my research efforts over the past 5 years. I would like to thank Dr. Mukesh Gupta, Dr. Joseph Vanderburgh, and Dr. Craig Duvall for their support of the nanoparticle project and teaching me polymer synthesis, micro/nanoparticle preparation methods, and characterization techniques. I would also like to thank the Vanderbilt Center for Bone Biology, specifically Alyssa Merkel, Josh Johnson, and Sasidhar Uppuganti for their help with cell culture, histology and μCT work. I would also like to thank the Vanderbilt Institute for Nanoscale Science and Engineering (VINSE) for access to the DLS, NanoAssemblr, and SEM machines. I would also like to thank Dr. Joseph Wenke and Dr. Krystal Blanchette from the United States Army Institute for Surgical Research (USAISR) for their collaboration and support over the past 6 years. Discussing the biofilm problem with Dr. Wenke has provided invaluable insight into the understanding of the overall focus of this

dissertation.

I am also grateful for all of the funding sources that supported this research. This work was supported in part by the National Institutes of Health (RO1AR064772) as well as other collaborative funds.

Finally, I would like to thank my friends and family. My friends in Nashville have been integral to my passionate approach and have helped me endure difficult days both inside and outside the lab. I'd like to thank my brothers Ryan and J.P. Spoonmore for all of their support and for allowing me to dominate conversation with research-minded questions. Finally, I'd like to thank my parents. Both parents have supported me thoroughly before and during this endeavor and always showed patience in their guidance. I'm sure it's possible to count the minutes that we have spent on the phone, but I wouldn't volunteer to do so. They wouldn't allow me to quit, and they wouldn't allow me to accept anything that didn't adhere to my standards. "We're not going out to defend anything after this success, we're going out to play for it." This dissertation is dedicated to them.

TABLE OF CONTENTS

Page

ACKNOWLEDGEMENTS ii

TABLE OF CONTENTS v

LIST OF TABLES vii

LIST OF FIGURES viii

Chapter

I. INTRODUCTION 1

Specific Aims 2
Approach 4
References 7

II. BACKGROUND 8

References 15

III. EFFECTS OF SURFACE MORPHOLOGY ON THE DEVELOPMENT OF ADHERENT, ANTIBIOTIC-RECALCITRANT *STAPHYLOCOCCUS AUREUS* BIOFILMS *IN VITRO*. .. 19

Abstract 19
Introduction 20
Materials and Methods 22
Results 27
Discussion 38
References 41

IV. REPURPOSING THE NONSTEROIDAL ANTI-INFLAMMATORY DRUG DIFLUNISAL AS A CONJUNCTIVE ANTI-VIRULENCE THERAPY FOR *STAPHYLOCOCCUS AUREUS* OSTEOMYELITIS 47

Repurposing the nonsteroidal anti-inflammatory drug diflunisal as an osteoprotective, anti-virulence therapy for *Staphylococcus aureus* osteomyelitis. 47
Abstract 47
Introduction 48
Materials and Methods 50
Results 55
Discussion 64
Concurrent local delivery of diflunisal limits bone destruction but fails to improve systemic vancomycin efficacy during *Staphylococcus aureus* osteomyelitis 72

Abstract 72
Introduction 73
Materials and Methods 74
Results 79
Discussion 86
References 94

V. DIFLUNISAL-LOADED POLY(PROPYLENE SULFIDE) NANOPARTICLES OUTLINE A DRUG DELIVERY PLATFORM TO AMELIORATE *S. AUREUS*-INDUCED BONE LOSS DURING OSTEOMYELITIS 98

Abstract 98
Introduction 99
Materials and Methods 100
Results 107
Discussion 115
References 118

VI. SUMMARY AND CONCLUSIONS 124

VII. FUTURE DIRECTIONS 127

In vitro investigation of antibiotic-tolerant biofilm development 127
Enhancements to current approach 127
Intravital imaging of bacteria on 3D substrates 129
Poly(propylene sulfide) Nanoparticle Delivery Platform 129
Enhancements to Current Approach 129
Bone- and infection-targeted NP to reduce bacterial burdens during Osteomyelitis 130
References 133

APPENDIX 134

Relevant protocols 134
Biofilm *in vitro* assay 134
Bone Scanning 137
Bone Scanning Analysis 139
Analysis of Cortical Bone (Destruction) 140
PPS-*b*-P(Aln-*co*-DMA) SYNTHESIS PROTOCOL 141
POLYMER MICELLE SYNTHESIS PROTOCOL 144
SUPERNATANT PREPARATION PROTOCOL 146
MC3T3 SUPERNATANT INTOXICATION ASSAY PROTOCOL 147

LIST OF TABLES

Table 3.1. Characterization of experimental scaffolds. 34
Table 3.2. Characterization of trabecular reconstructions. 34
Table 4.1. Group identification of mice treated with vancomycin and diflunisal. 86

LIST OF FIGURES

Figure 3.1. Maximum density of adherent bacteria is present on well plate surface 24 h post-inoculation. (A) Representative images of bacterial growth on 2D plate. Imaging performed by confocal laser scanning microscopy (CLSM). *S. aureus* depicted in red. Scale bar = 50 μm. (B) Quantification of bacterial growth by fraction of area covered by bacteria. N=3 biologic replicates. **** denotes $p<0.0001$ as determined by student's *t* test. (C) Quantification of bacterial fluorescence intensity within bacterial region of interest 24 h post-inoculation. N=3 biologic replicates. *** denotes $p<0.001$ as determined by student's *t* test..... 28
Figure 3.2. Vancomycin treatment of adherent bacterial communities 24 h post-inoculation does not eradicate entire bacterial population. (A) Vancomycin delivery for 0-24 h post-colonization decreases bacterial population, but does not eradicate all bacteria in either UAMS-1 or LAC strains. * denotes $p<0.05$, ** denotes $p<0.01$, **** denotes $p<0.0001$ as determined by 2-way ANOVA. (B) Vancomycin resistance was characterized by vancomycin MIC. Dotted line at an MIC of 4 μg/ml represents vancomycin intermediate S. aureus (VISA). (C) Bacterial populations following resuspension of both S. aureus strains and treatment with various concentrations of vancomycin. # represents no detectable CFUs. (D) Representative images following BODIPY-FL vancomycin treatment of biofilms on 2D substrate. Imaging performed by confocal laser scanning microscopy (CLSM). S. aureus cells are depicted in red and BODIPY-FL vancomycin is depicted in green. (E) Colocalization of S. aureus and BODIPY-FL vancomycin was determined by ImageJ. (F) Fluorescence analysis of bacteria characterizes vancomycin binding within adherent bacteria compared to resuspended biofilm bacteria. ** represents $p < 0.01$, **** represents $p < 0.0001$ as determined by 2-way ANOVA with multiple comparisons. N=3..... 30
Figure 3.3. Time-dependent development of adherent, antibiotic-tolerant bacterial communities. Colonization and antibiotic tolerant populations of (A) UAMS-1 and (B) LAC bacteria on 2D substrate was enumerated by the CFUs cm^{-2} over time post-inoculation. Y-axis starts at the limit of detection ($10^{1.34}$ $CFUs/cm^2$). N=3..... 32
Figure 3.4. Characterization of 3D substrates. μCT reconstructions of CX (A), CV (B), FH (C), PT (D), and VB (E) constructs. Scale bar = 1mm. SEM images of CX (F), CV (G), FH (H) surfaces. Scale bar = 200 μm. Trabecular analysis performed on CV and CX substrates analyzed surface area (I), SMI (J), and Tb.Sp (K). * represents $p < 0.05$, ** represents $p < 0.01$ as determined by student's t test. Similarly, trabecular analysis was performed on trabecular reconstructions to analyze surface area (L), SMI (M), and Tb.Sp (N). * represents $p < 0.05$, ** represents $p < 0.01$, *** represents $p < 0.001$ as determined by one-way ANOVA with multiple comparisons. N=3..... 35
Figure 3.5. Colonization and antibiotic-recalcitrance on CV and CX substrates. Representative SEM images of UAMS-1 24h post-inoculation on CV (A) and CX (B) constructs. Scale bar = 100 μm. Adherent cells on CV and CX substrates analyzed by CFU cm^{-2} for UAMS-1 (C) and LAC (D) strains. N=3 for all time points. Tolerant UAMS-1 (E) and LAC (F) bacteria adherent to CV and CX substrates. **** represents $p < 0.0001$ as determined by student's t test. N=3 for all time points..... 36
Figure 3.6. Antibiotic-recalcitrance on trabecular reconstructions at 24 h post-inoculation. Tolerant UAMS-1 bacteria on TEBC surfaces 24h post-inoculation. N=3 for all groups. *** represents $p < 0.001$, **** represents $p < 0.0001$ as determined by 2-way ANOVA with multiple comparisons..... 37

Figure 4.1.1. Diflunisal inhibits *S. aureus* cytotoxicity toward human and murine osteoblasts without affecting bacterial growth. (A) MC3T3 murine osteoblastic cells were intoxicated with 20% or 30% volume / volume (v/v) of concentrated supernatant (SN) from *S. aureus* grown in the presence of vehicle control (DMSO) or the indicated concentrations of diflunisal. Percent cell viability is depicted relative to mock intoxication with sterile RPMI. Error bars represent SD. N=5 per group and data are representative of three independent trials. *** denotes $p<0.001$ relative to vehicle control. (B) Same as (A), except that Saos-2 human osteoblastic cells, primary murine osteoblasts, or primary human osteoblasts were intoxicated with 30% v/v concentrated SN. N=10 and data are representative of at least 2 independent

trials. Error bars represent SD. *** denotes $p<0.001$ relative to vehicle control. (C) Growth analysis (Optical density at 600nm = OD_{600}) of *S. aureus* cultured in glass Erlenmeyer flasks with a 1:5 volume to flask ratio, and in the presence of two different vehicle controls (100% ethanol or DMSO) or 10 μg/ml diflunisal. Error bars represent SD. (D) Same as (B), except that 100 μg/ml of synthetic PSMα2 was added to concentrated supernatant prior to intoxication of primary human osteoblasts or MC3T3 cells. Cells were treated with vehicle (DMSO) or 10 μg/ml diflunisal. N=10 and data are representative of 2 independent trials. Error bars represent SD. *** denotes $p<0.001$ relative to vehicle control and ### denotes $p<0.001$ relative to diflunisal treated cells without PSMα2. 58
Figure 4.1.2. Supplementation of host cells with diflunisal does not inhibit cytotoxicity of untreated *S. aureus* supernatant. MC3T3 cells were intoxicated with concentrated supernatant from *S. aureus* grown in the presence (left) or absence (right) of vehicle control (DMSO) or 10 μg/ml diflunisal. Host cells were then cultured in the absence (left) or presence (right) of vehicle control (DMSO) or 10 μg/ml diflunisal. More specifically, fresh diflunisal or DMSO-supplemented cell culture media was added back to the cell monolayers at the time of intoxication with concentrated supernatant. N=5 per group and data are representative of two independent trials. Error bars represent SD. *** denotes $p<0.001$ relative to vehicle control. NS = not significant. 59
Figure 4.1.3. Potent inhibition of *S. aureus* cytotoxicity towards osteoblasts is unique to diflunisal. (A) MC3T3 cells were intoxicated with 20% or 30% v/v of concentrated SN from *S. aureus* grown in the presence of vehicle control (ethanol) or 10 μg/ml of the indicated NSAIDs. (B) Same as (A) except that *S. aureus was* grown in the presence of vehicle control (DMSO) or 10 μg/ml of piroxicam or diflunisal, as piroxicam was not soluble in ethanol. (C) Same as (A) except that *S. aureus was* grown in the presence of vehicle control (ethanol), 10 μg/ml diflunisal, or 50 μg/ml salicylic acid. For (A-C), percent cell viability is depicted relative to mock intoxication with sterile RPMI. Error bars represent SD. N=10 per group and data are representative of two independent trials. *** denotes $p<0.001$ and ** denotes $p<0.01$ relative to vehicle control. D) Dose-response curves were performed with concentrated SNs grown in the presence of increasing amounts of diflunisal, piroxicam, and salicylic acid (in DMSO). 30% v/v concentrated SNs were then used to intoxicate MC3T3 monolayers. Percent cell viability relative to mock intoxication with sterile RPMI containing equivalent concentrations of each NSAID. N=10 per group. Error bars represent SD. E) Growth analysis (Optical density at 600nm = OD_{600}) of *S. aureus* cultured in glass Erlenmeyer flasks with a 1:5 volume to flask ratio, and in the presence of the indicated concentrations of diflunisal, piroxicam, or vehicle control (DMSO). Error bars represent SD. N=3 per group and the data represent the average of two independent trials. 61
Figure 4.1.4. PUR drug delivery foams are effective as local therapies for experimental osteomyelitis. Groups (n=5) of 7-8 week female C57BL/6J mice were subjected to experimental osteomyelitis by inoculation with S. aureus. Following inoculation, either an empty PUR foam, or a foam containing 8% weight / weight vancomycin was sutured into place around the inoculation site. At 14 days post-inoculation, femurs were harvested and processed for CFU enumeration. Log_{10} CFU per femur is depicted. Horizontal bar represents the mean. Dotted line depicts the limit of detection for bacterial burdens. *** denotes $p<0.001$ relative to mice administered an empty foam. 63
Figure 4.1.5. Local diflunisal therapy significantly decreases *S. aureus*-induced bone destruction during osteomyelitis. (A) MC3T3 cells were intoxicated with 20% or 30% v/v concentrated *S. aureus* supernatant prepared from cultures grown in the presence of either an empty PUR foam or a foam containing 10mM diflunisal. N=10 per group and data are representative of three independent trials. Error bars represent SD. Percent cell viability is depicted relative to mock intoxication with sterile RPMI. *** denotes $p<0.001$ relative to empty foam treatment. (B-D) Groups of 7-8 week female C57BL/6J mice were subjected to experimental osteomyelitis by inoculation with *S. aureus*. Following inoculation, either an empty PUR foam, or a foam containing 10 mM diflunisal was sutured into place around the inoculation site. At 14 days post-inoculation, femurs were harvested and either processed for CFU enumeration (B) or μCT analysis (C and D). For CFU enumeration, n=5 per group and log_{10} CFU per femur is depicted. Horizontal bar represents the mean. Dotted line depicts the limit of detection for bacterial burdens. For μCT analysis, n=9 or 10 per group (one mouse in the control group suffered a

pathologic fracture), and data are the average of two independent trials. (C) Anteroposterior μCT images of femurs subjected to either mock treatment (empty foam) or local diflunisal therapy. (D) Quantification of cortical bone destruction. Error bar represents SD. ** denotes $p<0.01$. 65

Figure 4.2.1. Characterization of PUR and diflunisal-loaded PUR. SEM images of PUR foams containing 0 (A), 10 (B), and 20 mM (C) diflunisal. Scale bar = 200 μm. SEM images of PUR foams were used to determine porosity (%) (D) and pore diameter (μm) (E). (F) Release of diflunisal from PUR. Cumulative release was quantified as the amount of diflunisal released in the leachate normalized by the original amount of diflunisal in the foams. Daily release was quantified as the amount of diflunisal in the leachate at each time point. Error bars represent SD. N=6 per group. 80
Figure 4.2.2. Diflunisal does not inhibit vancomycin activity against *S. aureus* in vitro. *S. aureus* was cultured overnight with (A) or without (B) 25 μg/ml diflunisal. Diflunisal concentration was based on the total amount of diflunisal released from the foams determined in Fig. 1. Vancomycin was delivered at concentrations near the minimum inhibitory concentration (MIC) with and without diflunisal to characterize the effect of combined delivery on the bactericidal capability of vancomycin. N=3 technical replicates per group and data are representative of 3 independent trials. Error bars represent standard deviation (SD). Significance determined by Student's *t* test. 81
Figure 4.2.3. Local diflunisal therapy does not inhibit systemic vancomycin activity in vivo. (A) Vancomycin was delivered at 4 different concentrations to determine a sub-optimal dose that would significantly decrease the bacterial burdens in murine femurs infected with S. aureus. N=5 mice per group. Horizontal lines represent the mean. Dotted line depicts the limit of detection (LOD) for bacterial burdens. Error bars represent SD. * denotes $p<0.05$, **** denotes $p<0.0001$. (B-C) Mice were treated with either PUR + Veh or PUR-Dif (see Table 1). At 14 days post-infection, femurs (B) and foams (C) were harvested for CFU enumeration. N=4 or 5 mice per group (one mouse in the PUR+Veh group had to be euthanized according to humane endpoints). Control group demonstrates bacterial burdens consistent with separate trials (data not shown). * denotes $p<0.05$ relative to PUR + Veh treatment as determined by Student's t test. 85
Figure 4.2.4. (A) MicroCT reconstructions of femurs treated with PUR + Veh, PUR-Dif + Veh, PUR + Vanc, or PUR-Dif + Vanc (see Table 1). N=5 mice per group. One control group mouse suffered pathologic fracture (second from left in PUR + Veh group). (B) Quantification of cortical bone destruction. Error bar represents SD. ** denotes $p<0.01$, *** denotes $p<0.001$ as determined by Student's t test. 87

Figure 5.1. PPS_{135}-b-P(Cy7-ran-DMA_{149}) NPs load diflunisal with no effect on nanoparticle size. (A) PPS_{135}-b-P(Cy7-ran-DMA_{149}) structure contains repeat units of PPS (orange), Cy7 (red), and DMA (blue). (B) Schematic of micellar PPS NP encapsulating a loaded agent (diflunisal). Upon oxidation by reactive oxygen species (ROS), PPS NPs becomes unstable and degrade to release loaded agent. Diflunisal encapsulation was quantified by (C) loading and (D) encapsulation efficiency. N=3. Error bars represent SEM. * denotes $p < 0.05$, ** denotes $p < 0.01$, **** denotes $p < 0.0001$ as determined by two-way ANOVA. (E) Nanoparticle diameter (D_h) was analyzed for Empty-NP and Dif-NP. 109
Figure 5.2. PPS_{135}-b-P(Cy7-ran-DMA_{149}) NPs selectively accumulate at infected femurs during osteomyelitis. (A) Whole-body IVIS images of Empty-NP in non-infected mice 1 and 24 h post-injection. ROI analysis of the entire animal was quantified at 1h and 24h post-injection. ** denotes $p<0.01$ as determined by a paired Student's t test. (B) Time course analysis of Cy7 fluorescent signal accumulated in organs during osteomyelitis. N=3 mice per group. Error bars represent SEM. * denotes $p < 0.05$ as determined by 2-way ANOVA. (C) IVIS image of mouse 14 days-post infection. Representative group received daily tail vein injections of Dif-NP or Empty-NP. Fluorescence of infected and contralateral femurs were assessed using ROI analysis of the limbs. N=10 mice per group. Error bars represent SEM. **** denotes $p < 0.0001$ as determined by Student's t test. (D) Quantification of organs ex vivo 14 days post-infection following daily tail vein injections of Dif-NP or Empty-NP. N=10 mice per group. Error bars represent SEM. ** denotes $p < 0.01$ and **** denotes $p < 0.0001$ as determined by 1-way ANOVA.

..... 111
Figure 5.3. Release of loaded agent from PPS_{135}-b-P(Cy7-ran-DMA_{149}) NP is mediated by ROS concentration. Cumulative release of Nile red from Nile red-loaded NP exposed to various concentrations of H_2O_2. Error bars represent SEM. **** denotes $p<0.0001$ between the individual 0.33% and 3.3% H_2O_2 groups and all other groups at the given timepoint as determined by 2-way ANOVA. 112
Figure 5.4. Dif-NP inhibits S. aureus cytotoxicity toward murine osteoblasts. (A) MC3T3 murine pre-osteoblast cells were intoxicated with 20% (v/v) of concentrated supernatant from S. aureus grown in the presence of vehicle control (DMSO), NP vehicle control (Empty-NP), diflunisal (10 µg/ml in DMSO), or diflunisal (10 µg/ml encapsulated in NP). Fractional MC3T3 viability is depicted relative to mock intoxication with sterile RPMI. N=3. Error bars represent SEM. ** denotes $p<0.01$ and *** denotes $p<0.001$ as determined by 2-way ANOVA. (B) CFU enumeration of S. aureus cultured in same groups as (A). N=3. Error bars represent SEM. * denotes $p<0.01$ and ** denotes $p<0.001$ as determined by 2-way ANOVA. 113
Figure 5.5. Dif-NPs ameliorate S. aureus-induced bone destruction during osteomyelitis. (A) Representative µCT reconstructions of infected femurs 14 days post-infection treated with Empty-NP or Dif-NP via tail vein injection. N=12 mice per group. One mouse in the Empty-NP experienced >20% weight loss and was euthanized. (B) Quantification of cortical bone destruction for mice treated with Empty-NP or Dif-NP via tail vein injection. Error bars represent SEM. * denotes $p<0.05$ as determined by 1-way ANOVA. 114

Figure 7.1. Delayed antibiotic therapy results in treatment-recalcitrant infection. Mice infected with S. aureus were treated with 0 (Vehicle Control) or 30 mg/kg vancomycin injected subcutaneously either immediately after infection (Acute) or 24 h post-infection (Delayed). Bacterial burdens were assessed 7 days post-infection. N=5 mice per group. Lines represent the calculated mean. Limit of detection (LOD) = 10^2 CFU/femur. **** denotes $p<0.0001$ as determined by 2-way ANOVA. 132

CHAPTER 1

INTRODUCTION

Biofilms originate from planktonic (free-floating) bacteria and are defined as an adherent assemblage of bacterial cells entrapped in an extracellular matrix (1). The development of antibiotic-tolerant bacterial biofilms in the bone microenvironment is associated with recurrent infections resulting in an increased likelihood of patient morbidity and mortality (2-4). Long-term antibiotic therapy is the current gold standard for bacterial eradication; however, biofilms manifest as antibiotic-tolerant communities both *in vitro* and *in vivo* (5). As a result, the increased antibiotic tolerance requires extended antibiotic treatment times for biofilm eradication compared to planktonic communities *in vitro* (6, 7). It has been well established that avascular foreign materials implanted in the body provide a haven for bacterial colonization (8). With over 1.5 million total hip and knee replacements performed annually, bone infection is the most devastating risk associated with orthopedic implants (9). Thus, the development of bacterial biofilms on avascular surfaces requires further investigation to understand the mechanisms underlying the associated treatment recalcitrance.

Osteomyelitis is a devastating infection of bone that can be caused by the contiguous spread of bacteria from implanted devices or during a traumatic injury (10). *Staphylococcus aureus* is among the most common pathogens in bone (11). Factors that contribute to *S. aureus* pathogenesis include the asymptomatic nasal colonization in 30% of the human population, an array of adhesins that promote attachment to host tissue, and production of factors like Staphylococcal protein A that inhibit immune clearance (12-15). Moreover, *S. aureus* boasts an arsenal of virulence factors including pore-forming toxins (*e.g.* phenol soluble modulins [PSMs]) that lyse host cells such as bone-forming osteoblasts resulting in bacterial-mediated bone loss during osteomyelitis (16).

Furthermore, the treatment recalcitrance associated with bacterial biofilms promotes the recurrence of osteomyelitis (4). Therefore, innovation in osteomyelitis treatment is necessary to prevent bacterial-mediated morbidity. The overall objective of this dissertation is to provide innovative strategies to inhibit biofilm formation and ameliorate osteomyelitis-induced morbidity.

Specific Aims

The overarching goals of this work are to further understand biofilm development on 3D substrates in the context of direct antibiotic exposure, to develop an adjunctive biomaterial-based treatment strategy to ameliorate bone destruction induced during osteomyelitis, and to establish a platform for improved small molecule accumulation in infected bone during osteomyelitis. These goals were achieved through completion of the following aims.

Aim I: Understand the influence of 3D substrate morphology on antibiotic tolerance development in an adherent biofilm community *in vitro*.

Although biofilms have been defined in the literature (1), the methods for characterizing such communities continues to improve. Biofilm research encompasses a wide array of strains and species; however, this dissertation will focus primarily on *Staphylococcus aureus* biofilms. Vancomycin is a clinically-relevant antibiotic used for *S. aureus* treatment; however, the efficacy of this compound is diminished against *S. aureus* biofilms (17). We therefore anticipated that vancomycin activity would serve as an ideal surrogate marker for biofilm identification to characterize and quantify antibiotic-tolerant populations on various surfaces *in vitro*. Because previous work had shown that mammalian cell physiology was affected by surface morphology in a 3D *in vitro* model (18), we hypothesized that surface morphology would affect bacterial cell physiology in the context of biofilm development. Therefore, the development of vancomycin-

tolerant biofilm communities on 2D substrates will be discussed to outline vancomycin as a surrogate marker for biofilm presence. Next, using similar methods, the development of biofilms on various 3D substrates will be utilized to illustrate the effect of substrate morphology on biofilm development.

Aim II: Evaluate the efficacy of skeletal protective strategies to inhibit *S. aureus*-mediated destruction of host bone tissue during osteomyelitis.

Osteomyelitis often results in bone loss caused in part by cytolytic factors excreted from bacteria (16). Phenol soluble modulins (PSMs) are cytolytic factors produced by *S. aureus* and regulated by the accessory gene regulator (*agr*) pathway that contribute to decreased bone-forming osteoblast viability (16). Previous work has identified diflunisal, an FDA-approved nonsteroidal anti-inflammatory drug (NSAID), as a small molecule approach to mitigate the cytotoxicity induced by Agr-mediated production of PSMs (19). Due to the fact that diflunisal has a limited aqueous solubility profile (14.5 mg/L), we hypothesized that local diflunisal therapy released from PUR foams would limit bacterial-mediated bone destruction during osteomyelitis. Furthermore, we hypothesized that adjunctive diflunisal therapy would inhibit *S. aureus*-mediated bone destruction and would not interfere with systemic antibiotic activity at the infectious focus. To this end, diflunisal activity *in vitro* will be described as well as the efficacy of locally administered diflunisal *in vivo*. Furthermore, development of a clinically-relevant model for antibiotic treatment of osteomyelitis will be discussed. Finally, as a basis for understanding the effect of diflunisal on antibiotic efficacy, local therapy of diflunisal will be assessed in combination with systemic vancomycin therapy during osteomyelitis *in vivo*.

Aim III: Develop a parenteral biomaterial-based delivery platform for hydrophobic small molecule therapy of osteomyelitis.

A common limitation in bacterial treatment is the vehicle upon which antibiotics are administered (8). Beyond systemic administration that is still commonplace, multiple local therapeutic devices have been tested for the ability to eradicate bacteria from bone (20-22). However, foreign materials are frequently colonized by bacteria, a result that was observed in Aim II of this dissertation. Complications associated with local administration of diflunisal during osteomyelitis, such as the spread of bacteria to the PUR surface and the limitation of a single diflunisal payload in the PUR device, necessitated innovation in diflunisal delivery. In an effort to overcome the limited aqueous solubility of diflunisal and circumnavigate the necessity of an avascular foreign body, a parenteral delivery approach was adopted that also allowed for repeated administration of diflunisal. We hypothesized that a nanoparticle-based delivery strategy previously tested in our lab would allow for effective diflunisal delivery to the infectious focus without the complications associated with local treatment. To this end, nanoparticle delivery to infected and non-infected femurs *in vivo* will be outlined as a platform for hydrophobic small molecule delivery to treat osteomyelitis. Delivery of diflunisal-loaded nanoparticles will outline the proficiency of a nanoparticle-based osteomyelitis treatment.

Approach

Chapter 1 of this work provides an introduction to *S. aureus* biofilms and osteomyelitis and the justification behind the undertaking of this dissertation. **Chapter 2** provides a background on biofilm development and biofilm treatment currently understood through *in vitro* and *in vivo* models. An overview of current biofilm markers *in vitro* and *in vivo* will be presented, where specific examples of successful biofilm characterization will be outlined. A discussion on decreased antibiotic efficacy against biofilms compared to planktonic bacteria will follow. A background on specific therapeutic targets involved in staphylococcal pathogenesis will also be

presented followed by a focused discussion on therapeutic agents and strategies to ameliorate bacterial-mediated bone destruction during osteomyelitis.

Chapter 3 of this work discusses the development of a novel assay for identifying *S. aureus* biofilms *in vitro*. Bacterial biofilm communities were characterized on a 2D surface to further understand the timeline for biofilm development from planktonic bacteria. Vancomycin was utilized as a surrogate marker to quantify vancomycin-tolerant communities at various points post-inoculation. Following biofilm characterization in 2D, colonization and antibiotic tolerance on experimental 3D substrates was analyzed. 3D substrates were first characterized by morphological properties such as surface curvature and spacing within the 3D architecture to understand the effect of substrate morphology on biofilm development. This approach was expanded to anatomically-unique trabecular reconstructions to quantify biofilm communities within trabecular networks as well.

Chapter 4 of this work discusses the development of diflunisal-loaded PUR foams to inhibit *S. aureus*-induced bone loss during osteomyelitis. The ability of diflunisal to mitigate the production of virulence factors that are responsible for decreased osteoblast viability was tested *in vitro* and *in vivo*. Solubilized diflunisal activity and diflunisal-eluting PUR foams were tested in for the ability to mitigate *S. aureus* cytotoxicity using bone-forming osteoblast viability as an output. Next, the ability for diflunisal-loaded PUR to inhibit the bacterial-mediated bone destruction was determined by quantifying bone loss during osteomyelitis *in vivo*. Because diflunisal does not have an effect on bacterial burdens, further investigation was performed to understand diflunisal therapy in the context of antimicrobial treatment. Systemic vancomycin treatment of acute osteomyelitis was first assessed *in vivo* to identify a suboptimal dose with which diflunisal would be delivered. Finally, with a clinically-relevant osteomyelitis model of systemic

antibiotic therapy, local diflunisal was co-administered to understand the potential effects of diflunisal on vancomycin efficacy.

Chapter 5 of this work discusses the development of a nanoparticle-based delivery platform for hydrophobic small molecule treatment of osteomyelitis. Based on previous work done in our lab, poly(propylene sulfide) (PPS) micellar nanoparticles (NP) were known to encapsulate hydrophobic compounds for solubility improvement and greater parenteral delivery potential of said compounds *in vivo*. Because a large portion of novel antibiotics are hydrophobic and require chemical manipulation or drug carriers for effective delivery, we sought to develop a synthetic carrier capable of delivering hydrophobic compounds to an infectious focus in the body. Diflunisal was used as a model compound as it demonstrates a limited aqueous solubility profile and was known to be effective *in vivo*. Encapsulation of diflunisal in PPS NP was optimized to allow for the highest parenteral dose possible. Biodistribution of Cy7-conjugated PPS NP was assessed in infected and non-infected mice using an *In Vitro* Imaging System (IVIS) to outline the preferential distribution of PPS NP to the infectious focus. Diflunisal-loaded PPS NP were then delivered to determine the influence of PPS NP delivery to ameliorate bacterial-mediated bone loss during osteomyelitis.

Chapter 6 summarizes this work and makes conclusions based on the demonstrated results. **Chapter 7** provides a discussion for the future directions of this project to continue characterizing biofilm development on various different morphologies as well as discusses the next steps for diflunisal delivery *in vivo*. Further discussion is provided outlining the potential studies to further develop the PPS NP platform and improve osteomyelitis therapy.

References

1. Hall-Stoodley L, Costerton JW, Stoodley P. 2004. Bacterial biofilms: from the natural environment to infectious diseases. Nat Rev Microbiol 2:95-108.
2. Wolcott RD, Rhoads DD, Bennett ME, Wolcott BM, Gogokhia L, Costerton JW, Dowd SE. 2010. Chronic wounds and the medical biofilm paradigm. J Wound Care 19:45-6, 48-50, 52-3.
3. Costerton W, Veeh R, Shirtliff M, Pasmore M, Post C, Ehrlich G. 2003. The application of biofilm science to the study and control of chronic bacterial infections. J Clin Invest 112:1466-77.
4. Brady RA, Leid JG, Calhoun JH, Costerton JW, Shirtliff ME. 2008. Osteomyelitis and the role of biofilms in chronic infection. FEMS Immunol Med Microbiol 52:13-22.
5. Hoiby N, Bjarnsholt T, Givskov M, Molin S, Ciofu O. 2010. Antibiotic resistance of bacterial biofilms. Int J Antimicrob Agents 35:322-32.
6. Post V, Wahl P, Richards RG, Moriarty TF. 2017. Vancomycin displays time-dependent eradication of mature Staphylococcus aureus biofilms. J Orthop Res 35:381-388.
7. Mah TF, O'Toole GA. 2001. Mechanisms of biofilm resistance to antimicrobial agents. Trends Microbiol 9:34-9.
8. Zimmerli W, Waldvogel FA, Vaudaux P, Nydegger UE. 1982. Pathogenesis of foreign body infection: description and characteristics of an animal model. J Infect Dis 146:487-97.
9. Kurtz SM, Lau E, Watson H, Schmier JK, Parvizi J. 2012. Economic burden of periprosthetic joint infection in the United States. J Arthroplasty 27:61-5 e1.
10. Lew DP, Waldvogel FA. 2004. Osteomyelitis. Lancet 364:369-79.
11. Hatzenbuehler J, Pulling TJ. 2011. Diagnosis and management of osteomyelitis. Am Fam Physician 84:1027-33.
12. Foster TJ, Hook M. 1998. Surface protein adhesins of Staphylococcus aureus. Trends Microbiol 6:484-8.
13. Sakr A, Bregeon F, Mege JL, Rolain JM, Blin O. 2018. Staphylococcus aureus Nasal Colonization: An Update on Mechanisms, Epidemiology, Risk Factors, and Subsequent Infections. Front Microbiol 9:2419.
14. Dossett JH, Kronvall G, Williams RC, Jr., Quie PG. 1969. Antiphagocytic effects of staphylococfcal protein A. J Immunol 103:1405-10.
15. Forsgren A, Nordstrom K. 1974. Protein A from Staphylococcus aureus: the biological significance of its reaction with IgG. Ann N Y Acad Sci 236:252-66.
16. Cassat JE, Hammer ND, Campbell JP, Benson MA, Perrien DS, Mrak LN, Smeltzer MS, Torres VJ, Skaar EP. 2013. A secreted bacterial protease tailors the Staphylococcus aureus virulence repertoire to modulate bone remodeling during osteomyelitis. Cell Host Microbe 13:759-72.
17. Stewart PS. 2002. Mechanisms of antibiotic resistance in bacterial biofilms. Int J Med Microbiol 292:107-13.
18. Vanderburgh JP, Fernando SJ, Merkel AR, Sterling JA, Guelcher SA. 2017. Fabrication of Trabecular Bone-Templated Tissue-Engineered Constructs by 3D Inkjet Printing. Adv Healthc Mater 6.
19. Khodaverdian V, Pesho M, Truitt B, Bollinger L, Patel P, Nithianantham S, Yu G, Delaney E, Jankowsky E, Shoham M. 2013. Discovery of antivirulence agents against methicillin-resistant Staphylococcus aureus. Antimicrob Agents Chemother 57:3645-52.
20. Guelcher SA, Brown KV, Li B, Guda T, Lee BH, Wenke JC. 2011. Dual-purpose bone grafts improve healing and reduce infection. J Orthop Trauma 25:477-82.
21. Li B, Brown KV, Wenke JC, Guelcher SA. 2010. Sustained release of vancomycin from polyurethane scaffolds inhibits infection of bone wounds in a rat femoral segmental defect model. J Control Release 145:221-30.
22. Wenke JC, Guelcher SA. 2011. Dual delivery of an antibiotic and a growth factor addresses both the microbiological and biological challenges of contaminated bone fractures. Expert Opin Drug Deliv 8:1555-69.

CHAPTER 2

BACKGROUND

Antimicrobial discovery and development in the 20th century are among the most important events in United States medical history. Paul Ehrlich envisioned a "magic bullet" approach to curing syphilis, among other diseases, in which a synthetic compound would potently kill invading pathogens and spare the host (1). In the 1920's, Alexander Fleming discovered penicillin, one of the earliest antibiotics to be discovered, using a screening method focused on inhibition zones of growth in lawns of pathogenic bacteria on the surface of agar plates (2). Thus, began the "antibiotic era" in which antibiotics were discovered and mass produced to skew the advantage towards humans in the war against microbes. The "golden age" of antibiotic discovery occurred between the 1950s and 1970s in which compounds such as vancomycin were discovered (3, 4). Unfortunately, parallel research also uncovered the developing resistance and persistence of microbes following exposure to antimicrobial compounds (5, 6). Consequently, development of antibiotic resistance has intensified the need for consistent antibiotic discovery; however, no new classes of antibiotics have been developed since the "golden age." Further limiting the development of novel therapeutic strategies to combat invading pathogens, it has been reported that 40% of approved drugs and 90% of drugs in the developmental pipeline are considered poorly soluble (7). Strategies focused on overcoming this limitation involve the development of drug delivery carriers such as local delivery devices and nanoparticle (NP) platforms (8-11). Therefore, further innovation is required to optimize delivery and efficacy of clinically-relevant antibiotics. This dissertation will focus on developing potential strategies to improve current treatment practices in the war against microbes.

It is well-established that avascular foreign materials provide a haven for bacterial

adherence and colonization (12). Concomitant antibiotic delivery has allowed for an increase in biomedical device implantation. Currently, more than 1.5 million total hip and total knee replacement procedures are performed annually (13). However, despite the current antibiotic treatment available, musculoskeletal infection remains the most severe risk associated with orthopedic implants. Consequently, increased effort has focused on developing prophylactic technology to inhibit the cardinal adherence step in bacterial colonization and ameliorate further infectious complications. One way that researchers have sought to inhibit bacterial colonization is through the modification of implant surfaces. Examples of surface modifications include applications of silver coatings and the implementation of polymer brushes that decrease bacterial adhesion over time (14-16). Despite the innovation in prophylaxis technology, it has been reported that infection rates for elective surgeries still can't be reduced below 1-2% and rates of recurrent or persistent infection following a two-stage revision surgery are still around 33% (17-20). Collectively, with the reliability on antibiotic efficacy decreasing and the increased number of biomedical devices being implanted, antimicrobial therapeutic strategies that inhibit device-related infections require further study and improvement. This dissertation seeks to further the field of implant technology to mitigate the development of treatment-recalcitrant infections.

Osteomyelitis is a debilitating infection of bone frequently caused by contiguous spread of infection from a medical device or a traumatic injury (21). In total, it is estimated that implant-associated osteomyelitis is projected to burden the healthcare system by more than $1.62 billion by 2020 (22). These infections typically result in significant morbidities such as bone loss and implant failure. Low-level or "acute" infections typically require debridement, antibiotics, irrigation, and retention (DAIR), while "chronic" osteomyelitis requires 1- or 2-stage revision surgeries (23, 24). A 2-stage revision typically involves device removal and insertion of antibiotic-

laded beads to eradicate the infection prior to reimplantation (25). However, reinfection rates in hip and knee arthroplasties are still reported as high as 40% (19, 26). *Staphylococcus aureus* is among the most common pathogens in bone based on the asymptomatic nasal colonization in 30% of the human population, an array of adhesins that promote attachment to host tissue, and production of factors like staphylococcal protein A that inhibit immune clearance (27-30). Moreover, *S. aureus* boasts an arsenal of virulence factors including pore-forming toxins (*e.g.* phenol soluble modulins [PSMs]) that lyse host cells such as bone-forming osteoblasts resulting in bacterial-mediated bone loss during osteomyelitis (31). Therefore, due to the extreme difficulty in eradicating these infections, it is crucial to inhibit osteomyelitis-induced morbidity. This dissertation furthers the field of osteomyelitis treatment by providing a novel treatment strategy for the mitigation of bacterial-mediated bone loss.

A major factor contributing to treatment failure of bacterial infections is the formation of bacterial biofilms. Biofilms arise from planktonic bacterial cells that adhere to a surface and become entrapped in an extracellular matrix (32). Antibiotic susceptibility decreases as biofilm formation occurs, with mature biofilms able to withstand drug dosing up to 10^3 times greater than a planktonic community (27, 28, 33). Previous work suggested 4 possible mechanisms of biofilm-dependent antibiotic tolerance: i.) slow or incomplete antibiotic penetration into the biofilm matrix, ii.) a concentration gradient of metabolic substrates leads to zones of slow or non-growing bacteria, iii.) an adaptive stress response is expressed by a fraction of biofilm bacteria, and iv.) a small fraction of the cells differentiate into a highly protected persister state (34). The possible mechanisms of action for biofilm-mediated tolerance can be sorted into extracellular- and cellular-based classifications. Limited antibiotic diffusion through the extracellular matrix has been modeled extensively as an extracellular-mediated tolerance mechanism (35-37). Studies utilizing

fluorescently-tagged vancomycin of *S. aureus* biofilms have provided visual representation of this limited diffusion profile by quantifying the delayed vancomycin interaction with biofilm bacteria compared to the timeline observed with planktonic cells (38). In contrast, extensive research has been done to characterize the altered phenotypic persister state of biofilm bacteria (39). It has been proposed that biofilm communities produce a subpopulation of dormant cells resulting in a cellular-based mechanism of tolerance (40). Cell dormancy results in decreased cell activity that manifests through multiple outcomes such as decreased cell wall biosynthesis rendering antibiotics such as vancomycin less effective (4, 39). While the biology of persister cell development is still being elucidated, studies have shown that very few persisters are present in early exponential cultures (41). Yet, there is strong evidence for the presence of persisters within biofilms (39, 42, 43). Despite the fact that biofilm mechanisms remain a major question and area of research, it can be deduced that antibiotic binding to biofilm bacteria is limited compared to the planktonic state. Thus, whether by extracellular- or cellular-mediated mechanisms, biofilms decrease antibiotic binding to bacteria compared to the planktonic counterpart. Therefore, given that antibiotic tolerance is a hallmark of biofilm communities, biofilm presence could be functionally characterized and quantified using an antibiotic as a surrogate marker. Current methods of biofilm quantification include crystal violet staining (44), confocal microscopy (38, 45), and quantification of eDNA in the extracellular matrix by qPCR (46-48). Although these methods provide insight into the presence and properties of adherent communities, there remains a gap between this characterization and the resulting antibiotic tolerance. This dissertation furthers the knowledge of this field through design of an *in vitro* assay using cell survival following a standardized antibiotic exposure timeline as a quantifiable output for antibiotic tolerance, a manifestation of biofilm bacteria.

While device surface modification has proven the ability to decrease microbial colonization of substrates, less is known about inhibiting the development of antibiotic tolerance within adherent communities. Previous work in our lab has researched human mesenchymal stem cell activity on different 3D substrates to further understand the influence of morphology on cellular function (49). This study chose to highlight the different morphology of trabecular bone across various anatomical sites within the human body such as structural model index (SMI) to characterize surface curvature. Anatomically-characteristic SMI values were determined to have an effect on cellular function. Specifically, cellular differentiation was limited on convex surfaces (high SMI values) compared to concave surfaces (low SMI values). Although surface roughness is known to play a role in colonization, the effect of surface morphology on colonization and subsequent biofilm development is largely unknown. Chapter 3 of this dissertation furthers the knowledge of device-related infections by investigating the antibiotic-tolerant profile of biofilms on different 3D surface morphologies versus planktonic communities. Furthermore, understanding this tolerance profile allowed us to identify a potentially advantageous substrate morphology able to delay the onset of antibiotic tolerance in an adherent community.

Once an infection spreads to the bone, bacterial virulence can induce significant morbidity such as bone loss. The *S. aureus* accessory gene regulator (*agr*) system is a master virulence regulator known to regulate the production of cytolytic virulence factors such as PSMs resulting in bone destruction during osteomyelitis (31, 50). Staphylococcal quorum sensing is also accomplished by the Agr system, with a primary function of monitoring local population densities via secretion and detection of small autoinducer molecules in order to modulate gene expression (51, 52). Due to the fact that *agr*-null *S. aureus* mutant strains demonstrated a decrease in bacterial-mediated cortical bone destruction during osteomyelitis *in vivo*, the Agr system has been proposed

as an effective therapeutic target for hyper-virulent *S. aureus* (31). Development of a class of small molecules called "quorum quenchers" has been proposed as a promising strategy to interfere with Agr activity, and many compounds have been tested *in vitro* for quorum-quenching activity (51, 53-56). Of particular interest is the nonsteroidal anti-inflammatory drug (NSAID) diflunisal, which was predicted to inhibit AgrA phosphorylation, a critical step in activation of PSM production (57). However, although quorum-quenching approaches show great pre-clinical promise, functional suppression of the Agr pathway could also have detrimental effects on antimicrobial therapy for *S. aureus*. Specifically, inactivation of the *agr* locus leads to enhanced biofilm formation *in vitro*, which could conceivably limit antibiotic diffusion into the infectious niche (58-60). Therefore, further investigation into the repurposing of this FDA-approved small molecule is necessary to understand i.) the ability for diflunisal to mitigate virulence factor-associated bone loss during osteomyelitis and ii.) the off-target effect of quorum quenching on a staphylococcal community in the context of standard-of-care antibiotics. Nevertheless, quorum-quenching compounds provide a promising approach to mitigate morbidity associated with osteomyelitis. Chapter 4 of this dissertation furthers the field of osteomyelitis treatment by demonstrating the benefit of local diflunisal delivery from polyurethane (PUR) foams to ameliorate *S. aureus*-induced bone loss during osteomyelitis.

Because diflunisal is a compound with limited aqueous solubility (14.5 mg/L), systemic delivery of diflunisal as a free drug is rather limited. Therefore, local delivery using a PUR foam was necessary. As the results from Chapter 4 demonstrate, PUR foams provide a nidus for infection as has been seen previously with other avascular surfaces before (12, 61). Nanoparticle delivery platforms offer an alternative approach to hydrophobic compound delivery to circumvent the complications associated with avascular surfaces near the infected site. Previous work in our lab

has shown that polypropylene sulfide (PPS) NP provide a reactive oxygen species (ROS)-responsive drug release platform for delivery of GANT-58, a hydrophobic chemotherapeutic compound, to sites of bone metastasis (62). This PPS NP technology employs the enhanced permeability and retention (EPR) effect to accumulate drug-loaded NP at the disease site, similar to previous NP research (63). Because numerous diseases such as infection result in increased ROS levels, ROS-responsive materials provide an inflammation-mediated degradative release mechanism to accomplish more targeted release (64, 65). Moreover, the ROS-responsive release of loaded compounds from PPS NP promotes uniform delivery of any loaded compounds to similar environments. Thus, development of a nanoparticle platform capable of delivering hydrophobic compounds to treat osteomyelitis would allow for future investigation of multiple novel small molecules currently in the developmental pipeline. Given that diflunisal represents a class of hydrophobic compounds, this work provides innovation in small molecule osteomyelitis therapy by providing a platform for delivery of compounds in the developmental pipeline that exhibit limited hydrophilicity. Chapter 5 of this dissertation furthers the field of osteomyelitis treatment by demonstrating the ability for diflunisal-loaded PPS NP to inhibit *S. aureus*-induced bone loss.

Taken together, this dissertation focuses on the overall treatment of biofilm-associated disease in bone. Aim I (Chapter 3) of this work utilizes antibiotic tolerance to identify, characterize, and quantify biofilm *in vitro* and outline the influence of substrate morphology on antibiotic tolerance within adherent communities at specific times post-inoculation. Aim II (Chapter 4) of this dissertation focuses on treatment and preservation of infected bone using diflunisal as an anti-virulence agent in the context of standard-of-care antibiotic therapy. Aim III (Chapter 5) of this work utilizes the results of Aim II to develop a small molecule delivery platform that is employed in cancer research for treatment of osteomyelitis. Overall, this work progresses the field of infection prevention and treatment by providing potential strategies to delay antibiotic-tolerance

within adherent bacterial communities and by outlining anti-virulence strategies using a repurposed FDA-approved compound.

References

1. Strebhardt K, Ullrich A. 2008. Paul Ehrlich's magic bullet concept: 100 years of progress. Nat Rev Cancer 8:473-80.
2. Fleming A. 2001. On the antibacterial action of cultures of a penicillium, with special reference to their use in the isolation of B. influenzae. 1929. Bull World Health Organ 79:780-90.
3. Levine DP. 2008. Vancomycin: understanding its past and preserving its future. South Med J 101:284-91.
4. Levine JF. 1987. Vancomycin: a review. Med Clin North Am 71:1135-45.
5. Bigger J. 1944. Treatment of Staphyloeoeeal Infections with Penicillin by Intermittent Sterilisation. Lancet:497-500.
6. Marston HD, Dixon DM, Knisely JM, Palmore TN, Fauci AS. 2016. Antimicrobial Resistance. JAMA 316:1193-1204.
7. Loftsson T, Brewster ME. 2010. Pharmaceutical applications of cyclodextrins: basic science and product development. J Pharm Pharmacol 62:1607-21.
8. Cong Y, Quan C, Liu M, Liu J, Huang G, Tong G, Yin Y, Zhang C, Jiang Q. 2015. Alendronate-decorated biodegradable polymeric micelles for potential bone-targeted delivery of vancomycin. J Biomater Sci Polym Ed 26:629-43.
9. Danhier F, Ansorena E, Silva JM, Coco R, Le Breton A, Preat V. 2012. PLGA-based nanoparticles: an overview of biomedical applications. J Control Release 161:505-22.
10. Karau MJ, Schmidt-Malan SM, Greenwood-Quaintance KE, Mandrekar J, Cai J, Pierce WM, Jr., Merten K, Patel R. 2013. Treatment of Methicillin-resistant Staphylococcus aureus experimental Osteomyelitis with bone-targeted Vancomycin. Springerplus 2:329.
11. Oerlemans C, Bult W, Bos M, Storm G, Nijsen JF, Hennink WE. 2010. Polymeric micelles in anticancer therapy: targeting, imaging and triggered release. Pharm Res 27:2569-89.
12. Zimmerli W, Waldvogel FA, Vaudaux P, Nydegger UE. 1982. Pathogenesis of foreign body infection: description and characteristics of an animal model. J Infect Dis 146:487-97.
13. Maradit Kremers H, Larson DR, Crowson CS, Kremers WK, Washington RE, Steiner CA, Jiranek WA, Berry DJ. 2015. Prevalence of Total Hip and Knee Replacement in the United States. J Bone Joint Surg Am 97:1386-97.
14. Roe D, Karandikar B, Bonn-Savage N, Gibbins B, Roullet JB. 2008. Antimicrobial surface functionalization of plastic catheters by silver nanoparticles. J Antimicrob Chemother 61:869-76.
15. Roosjen A, van der Mei HC, Busscher HJ, Norde W. 2004. Microbial adhesion to poly(ethylene oxide) brushes: influence of polymer chain length and temperature. Langmuir 20:10949-55.
16. Stevens KN, Crespo-Biel O, van den Bosch EE, Dias AA, Knetsch ML, Aldenhoff YB, van der Veen FH, Maessen JG, Stobberingh EE, Koole LH. 2009. The relationship between the antimicrobial effect of catheter coatings containing silver nanoparticles and the coagulation of contacting blood. Biomaterials 30:3682-90.
17. Cram P, Lu X, Kates SL, Singh JA, Li Y, Wolf BR. 2012. Total knee arthroplasty volume, utilization, and outcomes among Medicare beneficiaries, 1991-2010. JAMA 308:1227-36.
18. Kurtz SM, Lau E, Schmier J, Ong KL, Zhao K, Parvizi J. 2008. Infection burden for hip and knee arthroplasty in the United States. J Arthroplasty 23:984-91.

19. Schwarz EM, Parvizi J, Gehrke T, Aiyer A, Battenberg A, Brown SA, Callaghan JJ, Citak M, Egol K, Garrigues GE, Ghert M, Goswami K, Green A, Hammound S, Kates SL, McLaren AC, Mont MA, Namdari S, Obremskey WT, O'Toole R, Raikin S, Restrepo C, Ricciardi B, Saeed K, Sanchez-Sotelo J, Shohat N, Tan T, Thirukumaran CP, Winters B. 2019. 2018 International Consensus Meeting on Musculoskeletal Infection: Research Priorities from the General Assembly Questions. J Orthop Res 37:997-1006.
20. Stulberg JJ, Delaney CP, Neuhauser DV, Aron DC, Fu P, Koroukian SM. 2010. Adherence to surgical care improvement project measures and the association with postoperative infections. JAMA 303:2479-85.
21. Lew DP, Waldvogel FA. 2004. Osteomyelitis. Lancet 364:369-79.
22. Kurtz SM, Lau E, Watson H, Schmier JK, Parvizi J. 2012. Economic burden of periprosthetic joint infection in the United States. J Arthroplasty 27:61-5 e1.
23. Kuiper JW, Vos SJ, Saouti R, Vergroesen DA, Graat HC, Debets-Ossenkopp YJ, Peters EJ, Nolte PA. 2013. Prosthetic joint-associated infections treated with DAIR (debridement, antibiotics, irrigation, and retention): analysis of risk factors and local antibiotic carriers in 91 patients. Acta Orthop 84:380-6.
24. Kuiper JW, Willink RT, Moojen DJ, van den Bekerom MP, Colen S. 2014. Treatment of acute periprosthetic infections with prosthesis retention: Review of current concepts. World J Orthop 5:667-76.
25. Hanssen AD. 2004. Prophylactic use of antibiotic bone cement: an emerging standard--in opposition. J Arthroplasty 19:73-7.
26. Azzam K, McHale K, Austin M, Purtill JJ, Parvizi J. 2009. Outcome of a second two-stage reimplantation for periprosthetic knee infection. Clin Orthop Relat Res 467:1706-14.
27. Foster TJ, Hook M. 1998. Surface protein adhesins of Staphylococcus aureus. Trends Microbiol 6:484-8.
28. Sakr A, Bregeon F, Mege JL, Rolain JM, Blin O. 2018. Staphylococcus aureus Nasal Colonization: An Update on Mechanisms, Epidemiology, Risk Factors, and Subsequent Infections. Front Microbiol 9:2419.
29. Dossett JH, Kronvall G, Williams RC, Jr., Quie PG. 1969. Antiphagocytic effects of staphylococfcal protein A. J Immunol 103:1405-10.
30. Forsgren A, Nordstrom K. 1974. Protein A from Staphylococcus aureus: the biological significance of its reaction with IgG. Ann N Y Acad Sci 236:252-66.
31. Cassat JE, Hammer ND, Campbell JP, Benson MA, Perrien DS, Mrak LN, Smeltzer MS, Torres VJ, Skaar EP. 2013. A secreted bacterial protease tailors the Staphylococcus aureus virulence repertoire to modulate bone remodeling during osteomyelitis. Cell Host Microbe 13:759-72.
32. Hall-Stoodley L, Costerton JW, Stoodley P. 2004. Bacterial biofilms: from the natural environment to infectious diseases. Nat Rev Microbiol 2:95-108.
33. Mah TF, O'Toole GA. 2001. Mechanisms of biofilm resistance to antimicrobial agents. Trends Microbiol 9:34-9.
34. Stewart PS. 2002. Mechanisms of antibiotic resistance in bacterial biofilms. International Journal of Medical Microbiology 292:107-113.
35. Stewart PS. 1996. Theoretical aspects of antibiotic diffusion into microbial biofilms. Antimicrob Agents Chemother 40:2517-22.
36. Stewart PS. 1998. A review of experimental measurements of effective diffusive permeabilities and effective diffusion coefficients in biofilms. Biotechnol Bioeng 59:261-72.
37. Stewart PS. 2003. Diffusion in biofilms. J Bacteriol 185:1485-91.
38. Jefferson KK, Goldmann DA, Pier GB. 2005. Use of confocal microscopy to analyze the rate of vancomycin penetration through Staphylococcus aureus biofilms. Antimicrob Agents Chemother 49:2467-73.
39. Lewis K. 2010. Persister cells. Annu Rev Microbiol 64:357-72.
40. Spoering AL, Lewis K. 2001. Biofilms and planktonic cells of Pseudomonas aeruginosa have

similar resistance to killing by antimicrobials. J Bacteriol 183:6746-51.
41. Keren I, Kaldalu N, Spoering A, Wang Y, Lewis K. 2004. Persister cells and tolerance to antimicrobials. FEMS Microbiol Lett 230:13-8.
42. Conlon BP, Nakayasu ES, Fleck LE, LaFleur MD, Isabella VM, Coleman K, Leonard SN, Smith RD, Adkins JN, Lewis K. 2013. Activated ClpP kills persisters and eradicates a chronic biofilm infection. Nature 503:365-70.
43. Waters EM, Rowe SE, O'Gara JP, Conlon BP. 2016. Convergence of Staphylococcus aureus Persister and Biofilm Research: Can Biofilms Be Defined as Communities of Adherent Persister Cells? PLoS Pathog 12:e1006012.
44. Merritt JH, Kadouri DE, O'Toole GA. 2005. Growing and analyzing static biofilms. Curr Protoc Microbiol Chapter 1:Unit 1B 1.
45. Schlafer S, Meyer RL. 2017. Confocal microscopy imaging of the biofilm matrix. J Microbiol Methods 138:50-59.
46. Atshan SS, Shamsudin MN, Karunanidhi A, van Belkum A, Lung LT, Sekawi Z, Nathan JJ, Ling KH, Seng JS, Ali AM, Abduljaleel SA, Hamat RA. 2013. Quantitative PCR analysis of genes expressed during biofilm development of methicillin resistant Staphylococcus aureus (MRSA). Infect Genet Evol 18:106-12.
47. Magalhaes AP, Franca A, Pereira MO, Cerca N. 2019. RNA-based qPCR as a tool to quantify and to characterize dual-species biofilms. Sci Rep 9:13639.
48. Perez-Osorio AC, Franklin MJ. 2008. qRT-PCR of Microbial Biofilms. CSH Protoc 2008:pdb prot5066.
49. Vanderburgh JP, Fernando SJ, Merkel AR, Sterling JA, Guelcher SA. 2017. Fabrication of Trabecular Bone-Templated Tissue-Engineered Constructs by 3D Inkjet Printing. Adv Healthc Mater 6.
50. Gillaspy AF, Hickmon SG, Skinner RA, Thomas JR, Nelson CL, Smeltzer MS. 1995. Role of the accessory gene regulator (agr) in pathogenesis of staphylococcal osteomyelitis. Infect Immun 63:3373-80.
51. Khan BA, Yeh AJ, Cheung GY, Otto M. 2015. Investigational therapies targeting quorum-sensing for the treatment of Staphylococcus aureus infections. Expert Opin Investig Drugs 24:689-704.
52. Novick RP. 2003. Autoinduction and signal transduction in the regulation of staphylococcal virulence. Mol Microbiol 48:1429-49.
53. Cech NB, Horswill AR. 2013. Small-molecule quorum quenchers to prevent Staphylococcus aureus infection. Future Microbiol 8:1511-4.
54. Harraghy N, Kerdudou S, Herrmann M. 2007. Quorum-sensing systems in staphylococci as therapeutic targets. Anal Bioanal Chem 387:437-44.
55. Kaufmann GF, Park J, Janda KD. 2008. Bacterial quorum sensing: a new target for anti-infective immunotherapy. Expert Opin Biol Ther 8:719-24.
56. Martin CA, Hoven AD, Cook AM. 2008. Therapeutic frontiers: preventing and treating infectious diseases by inhibiting bacterial quorum sensing. Eur J Clin Microbiol Infect Dis 27:635-42.
57. Khodaverdian V, Pesho M, Truitt B, Bollinger L, Patel P, Nithianantham S, Yu G, Delaney E, Jankowsky E, Shoham M. 2013. Discovery of antivirulence agents against methicillin-resistant Staphylococcus aureus. Antimicrob Agents Chemother 57:3645-52.
58. Boles BR, Horswill AR. 2008. Agr-mediated dispersal of Staphylococcus aureus biofilms. PLoS Pathog 4:e1000052.
59. Lauderdale KJ, Boles BR, Cheung AL, Horswill AR. 2009. Interconnections between Sigma B, agr, and proteolytic activity in Staphylococcus aureus biofilm maturation. Infect Immun 77:1623-35.
60. Sakoulas G, Moellering RC, Jr., Eliopoulos GM. 2006. Adaptation of methicillin-resistant Staphylococcus aureus in the face of vancomycin therapy. Clin Infect Dis 42 Suppl 1:S40-50.
61. Barth RE, Vogely HC, Hoepelman AI, Peters EJ. 2011. 'To bead or not to bead?' Treatment of

osteomyelitis and prosthetic joint-associated infections with gentamicin bead chains. Int J Antimicrob Agents 38:371-5.
62. Vanderburgh JP, Kwakwa KA, Werfel TA, Merkel AR, Gupta MK, Johnson RW, Guelcher SA, Duvall CL, Rhoades JA. 2019. Systemic delivery of a Gli inhibitor via polymeric nanocarriers inhibits tumor-induced bone disease. J Control Release 311-312:257-272.
63. Greish K. 2010. Enhanced permeability and retention (EPR) effect for anticancer nanomedicine drug targeting. Methods Mol Biol 624:25-37.
64. Dunnill C, Patton T, Brennan J, Barrett J, Dryden M, Cooke J, Leaper D, Georgopoulos NT. 2017. Reactive oxygen species (ROS) and wound healing: the functional role of ROS and emerging ROS-modulating technologies for augmentation of the healing process. Int Wound J 14:89-96.
65. Gupta MK, Meyer TA, Nelson CE, Duvall CL. 2012. Poly(PS-b-DMA) micelles for reactive oxygen species triggered drug release. J Control Release 162:591-8.

CHAPTER 3

EFFECTS OF SURFACE MORPHOLOGY ON THE DEVELOPMENT OF ADHERENT, ANTIBIOTIC-RECALCITRANT *STAPHYLOCOCCUS AUREUS* BIOFILMS *IN VITRO*.

Abstract

The development of antibiotic-recalcitrant bacterial biofilms on implanted devices results in chronic infection that often requires device removal, thereby causing significant patient morbidity. Multiple methods inhibit bacterial adherence to promote anti-biofilm effects. However, despite development of prophylaxis technologies, 1-2% of orthopedic implants still experience infectious complications. Therefore, further investigation into the colonization and antibiotic tolerance that develops within bacteria adherent to 3D materials is necessary. Due to the recent discovery that substrate morphology influences mammalian cell physiology, we sought to determine the influence on bacterial physiology in the context of antibiotic-tolerant biofilm development. In this study, we used vancomycin, a clinically-relevant antibiotic, to model antibiotic tolerance within bacterial communities. 3D substrates were synthesized to mimic different morphological parameters including surface curvature (characterized by structure model index [SMI]) and trabecular spacing (Tb.Sp.). Vancomycin tolerance was investigated in bacteria colonizing a well plate and revealed a significant proportion of recalcitrant adherent bacteria. A similar investigation of biofilm communities on 3D substrates exhibited a difference in antibiotic recalcitrance between substrates with different SMI and Tb.Sp. properties. It has been reported that trabecular bone reconstructions of different anatomical sites possess unique SMI and Tb.Sp. values. Antibiotic tolerance within adherent bacterial communities on anatomically-unique trabecular reconstructions revealed a similar influence of surface morphology in the context of trabecular bone colonization. Collectively, these results demonstrate the influence of surface morphology on

biofilm development within adherent bacterial populations in a 3D *in vitro* model.

Introduction

Biofilms are defined as an assemblage of bacterial cells adherent to a surface and entrapped in an extracellular matrix (1). Establishment of mature biofilms renders bacterial communities highly recalcitrant to conventional antibiotic treatment at concentrations capable of eradicating planktonic communities, contributing to the chronicity of diseases such as osteomyelitis (2, 3). Non-resistant Planktonic (free-floating) bacteria are susceptible to antibiotic treatment; however, it is well established that orthopedic implants provide a haven for bacterial adherence, colonization, and biofilm development (1, 4). Several technologies have been developed to inhibit the cardinal adherence step in biofilm formation including anti-adhesive polymeric brushes (5), silver coatings (6, 7), and antibiotic-releasing scaffolds (8-11). Despite major advances in prophylaxis, 1-2% of total prosthetics experience infectious complications (12-15). Accordingly, anti-biofilm analysis generally investigates the presence of bacteria (e.g. CFU enumeration or crystal violet staining (16)) on the substrate in question or the presence of extracellular components (e.g. confocal analysis (17, 18), qPCR analysis of extracellular DNA [eDNA] (19-21)) within the adherent bacterial community. While this approach offers insight into the ability for experimental technologies to inhibit bacterial adherence or colonization, more research is necessary to investigate the mechanisms by which biofilm bacteria tolerate antibiotics. Understanding the antibiotic tolerance associated with adherent bacteria may offer greater insight into failure of clinical antibiotic treatment.

Several mechanisms have been proposed to explain the decreased efficacy of antibiotics against biofilm bacteria compared with planktonic bacteria (22). Theories explaining biofilm survival during antibiotic exposure can be categorized into extracellular-associated mechanisms,

such as decreased diffusion of small molecules through the EPS (17, 22-25), or cell-associated mechanisms within the biofilm, such as the development of bacterial subpopulations with altered metabolism that renders them more tolerant of antibiotics, often defined as 'persister' cells (26, 27). Regardless, each mechanism results in a decreased interaction of antibiotic and bacterial cell. Thus, understanding the antibiotic-tolerance of bacterial populations colonizing novel biomaterials may further the discovery of anti-biofilm technology.

Previous work in our laboratory has focused on the development of trabecular reconstructions for *in vitro* 3D-modeling of diseases such as tumor-induced bone disease (28). Morphological properties of trabecular reconstructions such as bone volume fraction (BV/TV), surface curvature (represented by structure model index [SMI]), and trabecular spacing (Tb.Sp.) were discovered to influence cellular function, consistent with previous findings (29). For example, the metabolic activity of human bone marrow-derived stem cells was influenced by BV/TV, SMI, and Tb.Sp, and SMI demonstrated a substantial influence on the activity of bone-forming osteoblast cells. Although the influence of substrate morphology on mammalian cell physiology has been characterized, less is known concerning the morphological influence on bacterial physiology in the context of biofilm development, and such knowledge could guide the rationale design of biomaterials. Therefore, we sought to investigate the influence of 3D substrate morphology on the colonization and antibiotic-tolerance profile within adherent bacterial communities.

Due to the fact that *Staphylococcus aureus* is the most common bacterium isolated from implant-associated osteomyelitis, *S. aureus* was used as a model pathogen in this study (30-32). We hypothesized that surface morphology would influence *S. aureus* biofilm formation on 3D substrates. To test our hypothesis, we evaluated bacterial colonization and the presence of

antibiotic-tolerant populations adherent to various 2D and 3D substrates at specific times post-inoculation *in vitro*. Vancomycin is a standard antibiotic used for invasive bacterial infections due to efficacy against multiple Gram-positive organisms, including *S. aureus,* and a limited resistance profile (33, 34). Previous studies have shown that biofilms have decreased vancomycin binding compared to planktonic bacteria, and that the biofilm-associated bacteria are more tolerant to vancomycin (17, 24, 26). We therefore used vancomycin treatment of established bacterial communities as a surrogate marker for biofilm quantification. Taken together, this chapter outlines the influence of substrate morphology on bacterial colonization and antibiotic tolerance within adherent bacterial populations.

Materials and Methods

Materials

Lysine triisocyanate (LTI) was purchased from Jinan Haohua Industry Co., Ltd (Jinan, China) and refluxed with a dispersion of activated carbon (Fisher Scientific, Pittsburgh, PA) in *t*-butyl methyl ether (TBME, Acros-Organic, Geel, Belgium) at 60°C for 22h to remove high-molecular weight impurities. For trabecular reconstructions, nano-hydroxyapatite (nHA)-grafted lysine diisocyanate was used instead of LTI. Vancomycin-HCl and poly(caprolactone) triol (300 g mol^{-1}) were purchased from Sigma-Aldrich (St. Louis, MO). A stock of vancomycin-HCl was made by dissolving in 100% dimethylsulfoxide (DMSO) at a final concentration of 10 mg/ml. 24-well non-treated tissue culture plates (4.5 cm^2 per well) were purchased from Fisher Scientific. 24-well glass plates for confocal microscopy analysis were purchased from MatTek Life Sciences (Ashland, MA).

Bacterial strains, reagents, and growth conditions

The methicillin-resistant *S. aureus* (MRSA) USA300 lineage strain LAC and the methicillin-susceptible *S. aureus* (MSSA) USA200 lineage strain UAMS-1 were used for all experiments. USA300 lineage strains represent the most commonly isolated clonal complex causing musculoskeletal infection in the United States (35, 36), whereas UAMS-1 is a prototypical biofilm forming clinical strain originally isolated from a patient with chronic osteomyelitis (37). Overnight cultures were grown in tryptic soy broth (TSB) at 37°C and 180 RPM shaking. Optical density at 600 nm (OD_{600}) was measured to determine bacterial cell concentration to calculate initial seeding density.

Bacterial biofilm assay

S. aureus colonization of 24-well plates (2D) and 3D surfaces was assessed at various time points post-inoculation by enumerating colony forming units (CFUs) per substrate surface area. Bacteria were inoculated at a concentration of 10^2 CFUs cm^{-2} for 2D plates or 10^5 CFUs cm^{-2} for 3D substrates. To ensure sterility of 3D surfaces prior to bacterial colonization, 3D substrates were incubated in 70% ethanol for 10 min and washed with sterile phosphate buffered saline (PBS). Samples were incubated for various times post-inoculation at 37°C with agitation at 180 RPM. Following incubation, surfaces were washed 3X with sterile PBS to remove any non-adherent *S. aureus*. To quantify populations of *S. aureus* that were tolerant to antibiotic treatment, bacterial viability was assessed following exposure to 100 μg/ml (100X the minimum inhibitory concentration [MIC]) vancomycin for various times up to 24 h. Non-adherent cells were again removed by washing 3X with PBS. Substrates were immersed in 1 ml sterile PBS and placed in a sonicator bath for 5 mins to remove adherent bacteria remaining on each surface for enumeration. Sonicated solutions were serial-diluted and plated on tryptic soy agar (TSA) plates to determine

cell density. Bacterial enumerations are reported as CFUs normalized to the respective substrate surface area.

Confocal Imaging of 2D biofilms

S. aureus bacteria adherent to 24-well glass plates were fixed for 30 minutes with neutral-buffered formalin and washed using sterile PBS. For all confocal microscope experiments, adherent bacteria were stained using BactoView Live Red stains purchased from Biotium (Fremont, CA) for 30 minutes at 37^{o}C per manufacturer's instructions. BactoView Live Red is a DNA-binding dye that stains both live and dead bacteria. To determine the vancomycin penetration and binding within an adherent bacterial community, adherent bacteria were exposed to 100 μg/ml BODIPY-FL vancomycin (ThermoFisher, Waltham, MA) for 24 h. A Zeiss LSM710 was used to image 2D biofilms grown on plate surfaces. BactoView Live Red stains were imaged using a 561 nm excitation laser and an emission range of 600-750 nm. BODIPY-FL vancomycin was imaged using a 488 nm excitation laser and an emission range of 500-540 nm. For each experiment, 3 individual wells were imaged, each containing a biologic replicate. 5 images were obtained at 20X magnification in various random parts of the well for colonization studies. Each image was analyzed 5 times with a region of interest of 100 μm x 100 μm for % area colonized and fluorescence intensity to characterize colonization. Similarly, 5 images were obtained at 63X magnification using an oil-inversion lens for samples treated with BODIPY-FL vancomycin. Colocalization of vancomycin and bacteria was analyzed using ImageJ and reported as % area of vancomycin in the total bacteria region-of-interest. The region of interest was determined by thresholding 10% of the maximum signal within each image. Analysis of signal overlap within the bacterial region of interest was calculated to quantify the colocalization of BODIPY-FL

vancomycin within the adherent bacterial community.

Determination of vancomycin MIC for resuspended biofilm bacteria

To characterize the vancomycin resistance profile of biofilm bacteria, vancomycin E-test strips (Biomerieux, Inc., Marcy-I'Étoile, France) were used to quantify vancomycin MIC. Colonized substrates were washed and sonicated into 1 mL sterile PBS as described above to suspend adherent bacteria. 500 µl of the sonicated cell solution was plated as a lawn on TSA plates and allowed to dry. 1 Vancomycin E-test strip was placed on the dried plate and incubated overnight. MIC was determined as the intersection point between the E-test strip and the edge of the zone of killing, per manufacturer's instructions. MIC values were quantified for three biological replicates.

Vancomycin treatment of resuspended biofilms

To determine the susceptibility of biofilm bacteria in a planktonic state, adherent bacterial communities were resuspended into 1 ml sterile PBS from the well plate using a sonicator bath. Resuspended samples were centrifuged at 14,000g for 3 minutes and resuspended in TSB. Samples were diluted 10X in solutions containing 0, 10, and 100 µg/ml vancomycin in fresh TSB and incubated at 37°C. Samples were shaken for 24 hours at 180 RPM to limit adherence and maintain the planktonic state. Following treatment, samples were centrifuged at 14,000g for 10 minutes to separate viable bacteria from vancomycin-containing media and resuspended in 5 mL sterile PBS. Bacteria were then plated on TSA plates for CFU enumeration.

BODIPY-FL vancomycin treatment of adherent and resuspended biofilm bacteria

To compare the vancomycin binding in biofilm bacteria to planktonic bacteria, fluorescent signal

of BODIPY-FL vancomycin bound to biofilm or biofilm-resuspended *S. aureus* was analyzed. Adherent bacteria were washed and treated with 10 μg/ml BODIPY-FL vancomycin for 1 h at 37°C with agitation at 80 RPM similar to vancomycin treatment described above. To analyze vancomycin binding to planktonic bacteria, adherent communities were washed and separated from the well surface into 1 mL sterile PBS containing 0 or 10 μg/ml BODIPY-FL vancomycin using a sonicator bath. Samples were incubated for 1 h at 37°C and shaken at 180 RPM to maintain planktonic state. Following treatment, samples were centrifuged at 14,000g for 10 minutes to separate bacteria from BODIPY-FL vancomycin-containing media and resuspended in 1 mL sterile PBS. The amount of BODIPY-FL vancomycin (ex: 470, em: 509) bound to bacteria was analyzed using a plate reader.

Synthesis and characterization of 3D substrates

3D Convex (CX) lattices were fabricated from poly(lactic acid) (PLA) by Fused Deposition Modeling (MakerBot Replicator 2 3D printer) as described previously (38). Concave (CV) lattice-like scaffolds were prepared by filling the pores of the CX scaffolds with a settable poly(ester urethane) (PEUR) comprising lysine triisocyanate and ε-caprolactone followed by extraction of PLA using chloroform (38). Scaffolds with morphometric properties mimicking those of specific skeletal sites were fabricated using a Solidscape 3Z Studio Inkjet 3D printer as we have described previously (28). Briefly, human cadaver samples from the femoral head (FH), proximal tibia (PT), and lumbar vertebral body (VB) were imaged by μCT and the images converted to STL files. Sulfonamide wax molds were printed from the STL files, filled with the settable PEUR resin, and extracted with dichloromethane to remove the wax. Trabecular reconstructions were synthesized using an LDI-nHA hybrid material containing 45% nHA. All

3D substrates were imaged by μCT (Scanco μCT50) and the bone morphometric properties of surface area (S_A), bone volume/total volume (BV/TV), trabecular separation (Tb.Sp.), and structure model index (SMI, related to surface curvature) were calculated from 3D reconstructions. Untreated 24-well tissue culture plates (2D) were used as a control surface for 2D and 3D comparisons.

Results

Confocal imaging of bacteria colonization of 2D surface

To investigate bacterial colonization of a 2D substrate over a 24 h time period, *S. aureus* colonization of the well plate was first analyzed similar to previous studies (18). Bacteria were inoculated at 10^2 CFUs cm^{-2} and incubated for 6, 10 (LAC), 12 (UAMS-1), or 24 h post-inoculation. Following incubation, bacteria were fixed and stained with BactoView Live Red to obtain images via confocal laser scanning microscopy (CLSM) (**Fig. 3.1A**). Bacterial surface colonization was quantified by the fraction of imaged area containing bacteria (**Fig. 3.1B**). Both strains demonstrate increasing colonization over time with a significantly different colonization area of bacteria adherent after 24 h (**Fig. 3.1C**). Therefore, we identified the maximum adherent assemblage of UAMS-1 and LAC bacterial communities 24 h post-inoculation for further biofilm study.

Resuspended biofilms demonstrate susceptibility to vancomycin

An increase in antibiotic recalcitrance is a known manifestation of bacterial biofilms (1). Given that an assemblage of bacterial cells was observed on the well plate surface 24 h post-inoculation, we sought to characterize the antibiotic recalcitrance of these bacteria. Vancomycin was used as a

surrogate marker to characterize antibiotic recalcitrance. First, adherent bacteria were exposed to

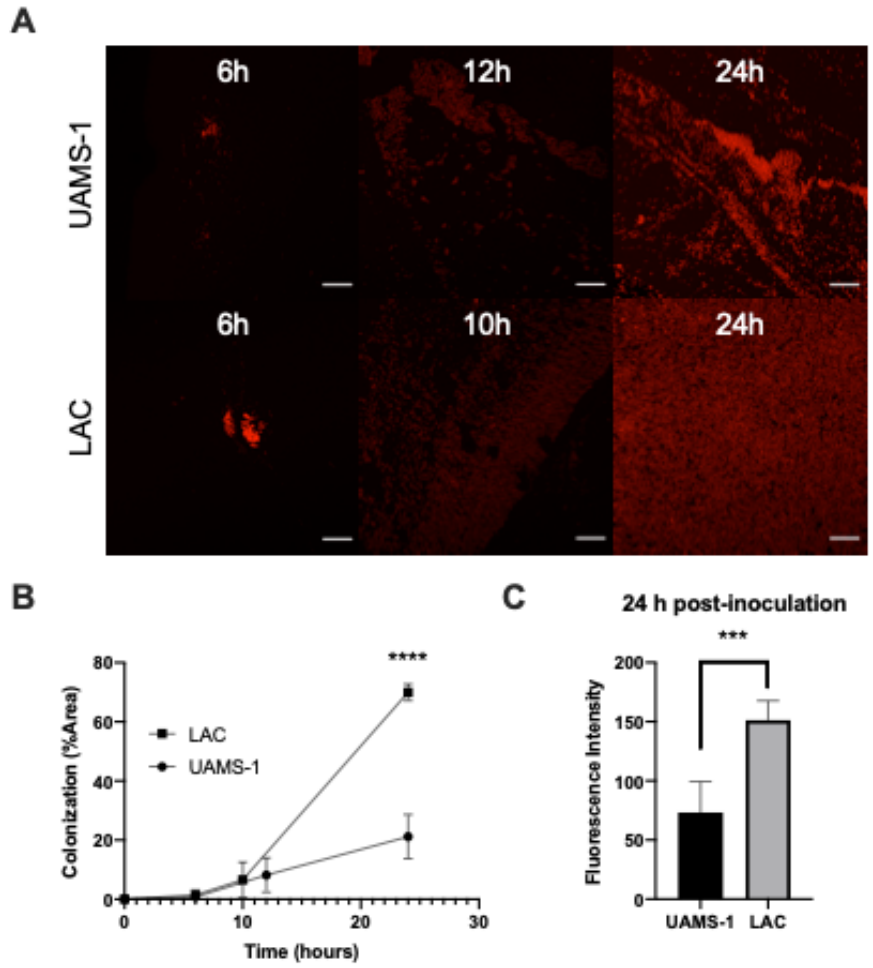

Figure 3.1. Maximum density of adherent bacteria is present on well plate surface 24 h post-inoculation. (A) Representative images of bacterial growth on 2D plate. Imaging performed by confocal laser scanning microscopy (CLSM). *S. aureus* depicted in red. Scale bar = 50 µm. (B) Quantification of bacterial growth by fraction of area covered by bacteria. N=3 biologic replicates. **** denotes $p<0.0001$ as determined by student's *t* test. (C) Quantification of bacterial fluorescence intensity within bacterial region of interest 24 h post-inoculation. N=3 biologic replicates. *** denotes $p<0.001$ as determined by student's *t* test.

0 or 100 µg/ml vancomycin (100X MIC) for various times post-colonization. Bacterial populations treated with 0 µg/ml vancomycin demonstrated a significantly greater population density than bacteria treated with 100 µg/ml vancomycin for 2 h or more (**Fig. 3.2A**). However, a substantial population of viable, adherent bacteria survived 100 µg/ml vancomycin treatment. We hypothesized that this population remained through either vancomycin resistance of bacteria

within the adherent population or the formation of a biofilm. To investigate the vancomycin susceptibility of the bacteria within adherent communities, vancomycin E-test strips were used to quantify the minimum inhibitory concentration (MIC) values of adherent UAMS-1 and LAC bacteria. Both strains exhibited MIC values below a vancomycin intermediate *S. aureus* (VISA, MIC=4-8 μg/ml) profile reported previously suggesting the bacteria were not vancomycin-resistant (**Fig. 3.2B**) (39). To test the vancomycin recalcitrance of the planktonic counterpart, biofilm bacteria were resuspended and treated with 0, 10, or 100 μg/ml vancomycin in the planktonic state. Antibiotic recalcitrance of the planktonic counterpart was not observed as vancomycin treatment eradicated planktonic bacteria at a dose that was incapable of eradicating an adherent community (**Fig. 3.2C**). Therefore, bacterial adherence promotes an antibiotic tolerance that is not observed in a planktonic community. Moreover, tolerance is not associated with an increase in the MIC of the community. It has been proposed that biofilm-mediated antibiotic tolerance results from mechanisms such as incomplete penetration of antibiotic in the biofilm that may reduce vancomycin binding to biofilm bacteria (22, 24, 25, 40). We therefore sought to characterize the vancomycin binding profile within an adherent community after 24 h of exposure. Adherent bacterial communities at 24 h post-inoculation were treated with BODIPY-FL vancomycin and imaged using CLSM as above. Confocal microscope images of the BODIPY-FL vancomycin signal within the adherent population were used to analyze the colocalization of vancomycin and bacteria (**Fig. 3.2D**). Interestingly, not all cells colocalized with vancomycin (**Fig. 3.2E**). In order to understand the incomplete vancomycin binding that may have occurred within the adherent population, vancomycin signal bound to adherent bacteria was compared with vancomycin signal bound to a planktonic counterpart. Resuspended communities exhibited substantially greater fluorescence compared to adherent populations for both UAMS-1 and LAC

strains suggesting decreased vancomycin binding in adherent communities compared to the planktonic counterpart (**Fig. 3.2F**). Notably, no substantial difference was detected between vancomycin signal within UAMS-1 or LAC biofilms. Therefore, adherent bacterial communities demonstrate non-resistant vancomycin recalcitrance due to decreased vancomycin binding. Taken together, the assemblage of antibiotic-recalcitrant bacteria adherent to the well plate outline the manifestation of a biofilm at 24 h post-inoculation.

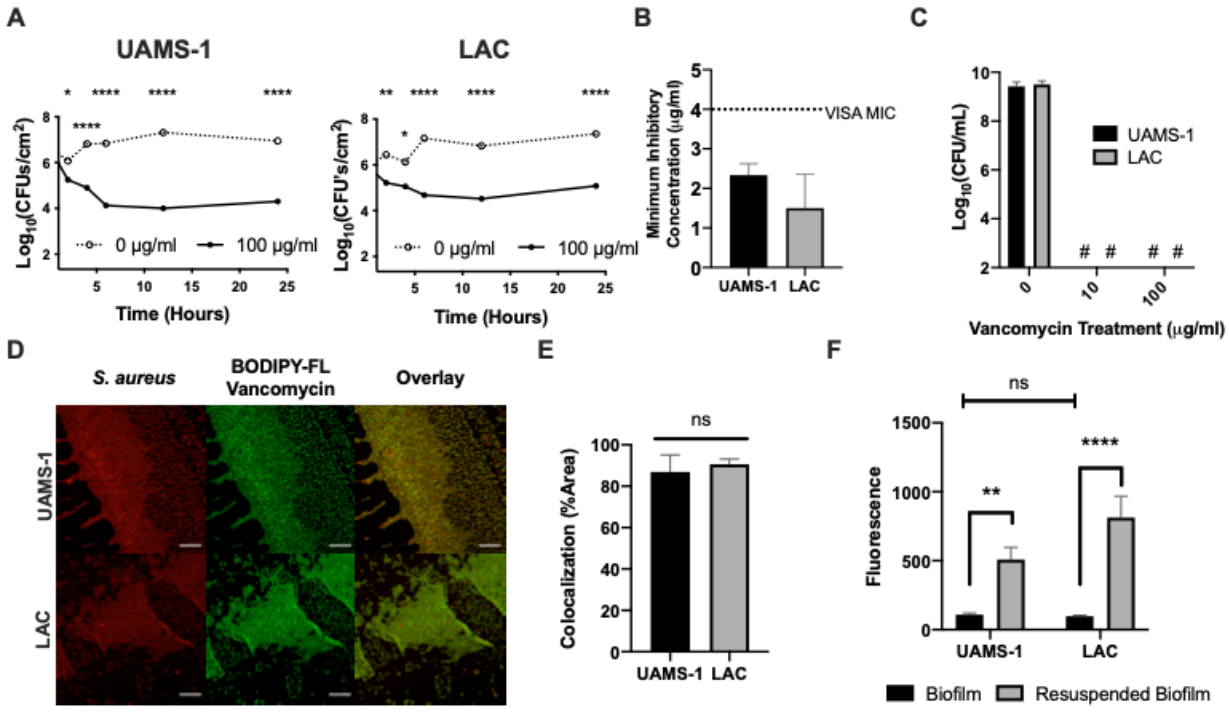

Figure 3.2. Vancomycin treatment of adherent bacterial communities 24 h post-inoculation does not eradicate entire bacterial population. (A) Vancomycin delivery for 0-24 h post-colonization decreases bacterial population, but does not eradicate all bacteria in either UAMS-1 or LAC strains. * denotes $p<0.05$, ** denotes $p<0.01$, **** denotes $p<0.0001$ as determined by 2-way ANOVA. (B) Vancomycin resistance was characterized by vancomycin MIC. Dotted line at an MIC of 4 µg/ml represents vancomycin intermediate S. aureus (VISA). (C) Bacterial populations following resuspension of both S. aureus strains and treatment with various concentrations of vancomycin. # represents no detectable CFUs. (D) Representative images following BODIPY-FL vancomycin treatment of biofilms on 2D substrate. Imaging performed by confocal laser scanning microscopy (CLSM). S. aureus cells are depicted in red and BODIPY-FL vancomycin is depicted in green. (E) Colocalization of S. aureus and BODIPY-FL vancomycin was determined by ImageJ. (F) Fluorescence analysis of bacteria characterizes vancomycin binding within adherent bacteria compared to resuspended biofilm bacteria. ** represents $p < 0.01$, **** represents $p < 0.0001$ as determined by 2-way ANOVA with multiple comparisons. N=3.

Colonization and biofilm development on 2D surface

Given that vancomycin-recalcitrant communities adhere and establish by 24 h post-inoculation, we sought to understand the kinetic colonization and development of antibiotic-recalcitrant communities on the well plate. To quantify the time-dependent colonization of the well plate, bacteria were enumerated at various points post-inoculation. Antibiotic recalcitrance was defined over time by enumerating bacterial populations that survived subsequent treatment with vancomycin for 24 hours. Consistent with qualitative results from CLSM analysis, both UAMS-1 and LAC colonization of 2D surfaces increased over time post-inoculation (**Fig. 3.3A-B**). For each strain, a bacterial density of approximately 10^7 CFUs cm^{-2} was observed following 24 h of incubation. An exponential colonization phase occurred between 4 - 12 h (colonization rate = 0.51 ± 0.04 $\log_{10}$(CFUs cm^{-2}) h^{-1}) for UAMS-1 and 2 - 12 h for LAC (colonization rate = 0.38 ± 0.09 $\log_{10}$(CFUs cm^{-2}) h^{-1}). Consistent with the above results analyzing adherent bacterial populations that survived vancomycin exposure, a large population of approximately 10^5 CFU cm^{-2} remained following vancomycin treatment (**Fig. 3.3A-B**). Interestingly, recalcitrant populations are present as early as 10 h post-inoculation for UAMS-1 and recalcitrant LAC populations were present as early as 6 h post-inoculation. Similar to the kinetics of bacterial colonization, exponential recalcitrance population development occurred between 10 – 24 h post-inoculation (recalcitrant population development rate = 0.28 ± 0.04 $\log_{10}$(CFUs cm^{-2}) h^{-1}) for UAMS-1 and 6 – 12 h (recalcitrant population development rate = 0.44 ± 0.07 $\log_{10}$(CFUs cm^{-2}) h^{-1}) for LAC. Collectively, these results demonstrate the time-dependent progression of sterile substrates colonized by vancomycin-recalcitrant biofilm communities.

Characterization of 3D Structures

In order to model bacterial colonization of implanted substrates more accurately, multiple 3D

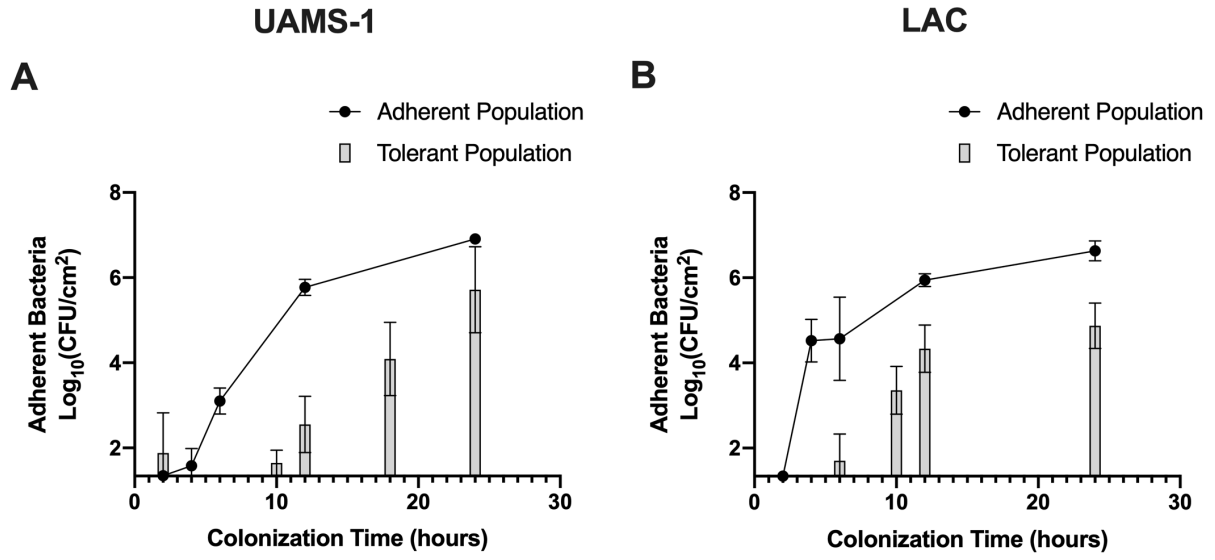

Figure 3.3. Time-dependent development of adherent, antibiotic-tolerant bacterial communities. Colonization and antibiotic tolerant populations of (A) UAMS-1 and (B) LAC bacteria on 2D substrate was enumerated by the CFUs cm^{-2} over time post-inoculation. Y-axis starts at the limit of detection ($10^{1.34}$ CFUs/cm^2). N=3.

substrates were synthesized to resemble different morphological parameters. 3D substrates representing different morphological parameters of anatomically-unique trabecular reconstructions were synthesized as previously reported (28). To model different surface curvature (characterized by structure model index [SMI]) and trabecular spacing (Tb.Sp.), CV and CX substrates were synthesized and the morphological properties assessed using μCT analysis. CX scaffolds were directly 3D printed, while CV scaffolds were molded from CX templates and extracted to remove the PLA material. CX substrates were designed as a network of rod-like structures (**Fig. 3.4A**), while CV substrates were designed as an inverse network of concave pores (**Fig. 3.4B**). Similarly, FH, PT, and VB trabecular reconstructions were molded from wax templates using an inkjet 3D printer as reported previously (41) and μCT reconstructions of FH (**Fig. 3.4C**), PT (**Fig. 3.4D**), and VB (**Fig. 3.4E**) were used to assess morphological properties. SEM images for each substrate are also shown, with FH surface representing the surface of all

trabecular reconstructions (**Fig. 3.4F-H**). Substantial differences in surface area (**Fig. 3.4I**), Tb.Sp. (**Fig. 3.4J**), and SMI (**Fig. 3.4K**) were observed between CV and CX substrates. CV and CX substrates exhibited Tb.Sp of 0.326 ± 0.002 mm and 0.45 ± 0.03 mm, respectively. SMI values of CV and CX constructs were 0.6 ± 0.2 and 1.19 ± 0.12, respectively. SMI values are reported as a value on a scale between 0 and 3 with an SMI value of 3 representing completely rod-like trabecular construction and a value of 0 representing plate-like structure (42). The SMI value of the concave structure is indicative of a plate-like network; however, scaffolds were synthesized as an inverse of CX constructs and qualitatively demonstrate a concave lattice (**Fig. 3.4B, 3.4G**). The properties of 2D, CV, and CX substrates are described in **Table 3.1**. Similarly, substantial differences in surface area (**Fig. 3.4L**), Tb.Sp. (**Fig. 3.4M**), and SMI (**Fig. 3.4N**) were observed between FH constructs compared to PT and VB reconstructions. FH, PT, and VB substrates demonstrated Tb. Sp values of 0.72 ± 0.03, 0.84 ± 0.02, and 0.96 ± 0.04 mm, respectively. SMI values for trabecular reconstructions were also quantified as 1.06 ± 0.08 for FH, 1.94 ± 0.06 for PT, and 2.20 ± 0.09 for VB. The properties of the trabecular reconstructions are described in **Table 3.2**. Collectively, the characterization of experimental 3D substrates demonstrates the scope of surface area, Tb.Sp, and SMI values within 3D printed constructs.

Effects of substrate morphology on biofilm development

Given that previously published results outline the effect of surface morphology on mammalian cell physiology (28), we sought to determine the effect of surface morphology on bacterial cell physiology in the context of biofilm development. CV and CX substrates were used to analyze the influence of SMI and Tb.Sp. on antibiotic tolerance in adherent communities 24 h post-inoculation. Vancomycin treatment of adherent bacteria on 2D substrates of the different materials used (poly(lactic acid), poly(ester-urethane), polystyrene) revealed no significant difference between

Table 0.1. Characterization of experimental scaffolds.

Name	Polymer	S_A (cm^2)	Tb.Sp (mm)	Tb.N (mm^{-1})	Tb.Th (mm)	SMI
2D (Well plate)	PS	4.5	N/A	N/A	N/A	N/A
CV (Concave)	PEUR	1.9 ± 0.3	0.326 ± 0.002	3.05 ± 0.15	0.38 ± 0.02	0.6 ± 0.2
CX (Convex	PLA	1.11 ± 0.08	0.45 ± 0.03	1.63 ± 0.05	0.290 ± 0.008	1.19 ± 0.12

Table 0.2. Characterization of trabecular reconstructions.

Name	Polymer	S_A (cm^2)	Tb. Sp. (mm)	Tb. N. (mm^{-1})	Tb.Th (mm)	SMI
FH (Femoral Head)	PEUR	2.8 ± 0.3	0.72 ± 0.03	1.23 ± 0.03	0.247 ± 0.012	1.06 ± 0.08
PT (Proximal Tibia)	PEUR	1.64 ± 0.02	0.84 ± 0.02	1.05 ± 0.04	0.201 ± 0.008	1.94 ± 0.06
VB (Vertebral Body)	PEUR	1.40 ± 0.03	0.96 ± 0.04	0.96 ± 0.04	0.204 ± 0.009	2.20 ± 0.09

bacterial communities 24 h post-inoculation suggesting material chemistry was not a major factor in colonization or tolerance development (**Supp. Fig. 3.1**). To investigate the vancomycin-resistance of bacteria colonizing 3D substrates 24 h post-inoculation, analysis of vancomycin MIC was tested as above. Bacteria grown on 3D substrates did not exceed an average MIC value of 4 µg/ml suggesting these bacteria were not resistant (**Supp. Fig. 3.2**). To accommodate the different surface area between each substrate, inoculation and analysis of CFU enumeration was normalized by substrate surface area. Bacteria were seeded on CV or CX substrates at 10^5 CFUs cm^{-2} and incubated for various times, replicating the 2D assay protocol. Bacterial populations were imaged 24 h post-inoculation by SEM on CV (**Fig. 3.5A**) and CX (**Fig. 3.5B**) substrates to qualitatively analyze an assemblage of bacterial cells on the substrate surface. Analysis of bacterial populations adherent to the 3D substrates revealed similar colonization to that of the 2D well plate; planktonic

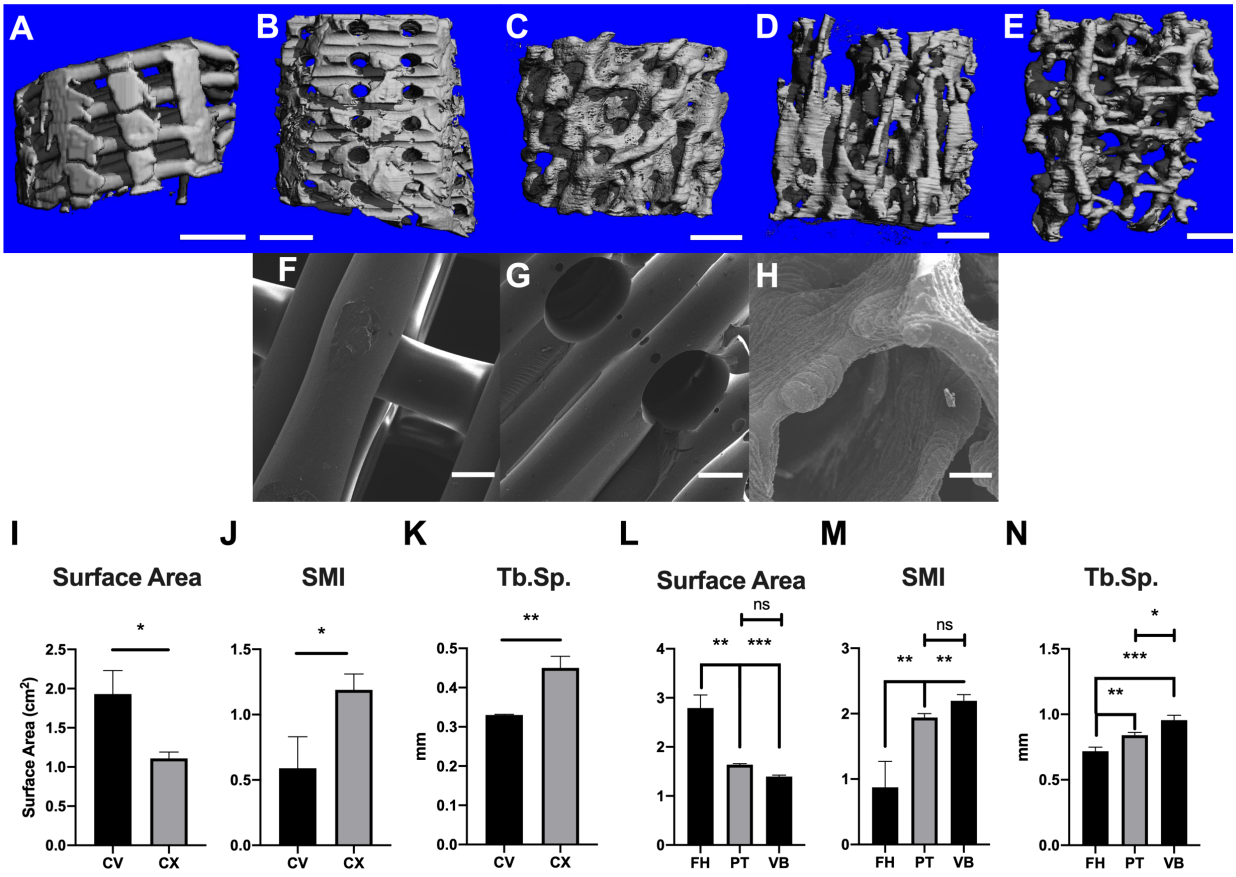

Figure 3.4. Characterization of 3D substrates. µCT reconstructions of CX (A), CV (B), FH (C), PT (D), and VB (E) constructs. Scale bar = 1mm. SEM images of CX (F), CV (G), FH (H) surfaces. Scale bar = 200 µm. Trabecular analysis performed on CV and CX substrates analyzed surface area (I), SMI (J), and Tb.Sp (K). * represents $p < 0.05$, ** represents $p < 0.01$ as determined by student's t test. Similarly, trabecular analysis was performed on trabecular reconstructions to analyze surface area (L), SMI (M), and Tb.Sp (N). * represents $p < 0.05$, ** represents $p < 0.01$, *** represents $p < 0.001$ as determined by one-way ANOVA with multiple comparisons. N=3.

cells exhibit a time-dependent increase in adherent bacteria on the substrate surface (**Fig. 3.5C-D**). Importantly, adherent bacterial populations of both UAMS-1 and LAC strains 24 h post-inoculation on CV and CX substrates were not significantly different when normalized by substrate surface area. However, vancomycin treatment of adherent biofilms revealed a substantially greater antibiotic-recalcitrant population for UAMS-1 bacteria adherent to a CV substrate compared to a CX substrate (**Fig. 3.5E**). This phenomenon was not observed in LAC communities incubated on both substrates (**Fig. 3.5F**). Therefore, substrates containing greater SMI and Tb.Sp. (CX) result

in a decreased antibiotic recalcitrance within adherent UAMS-1 biofilm communities 24 h post-inoculation.

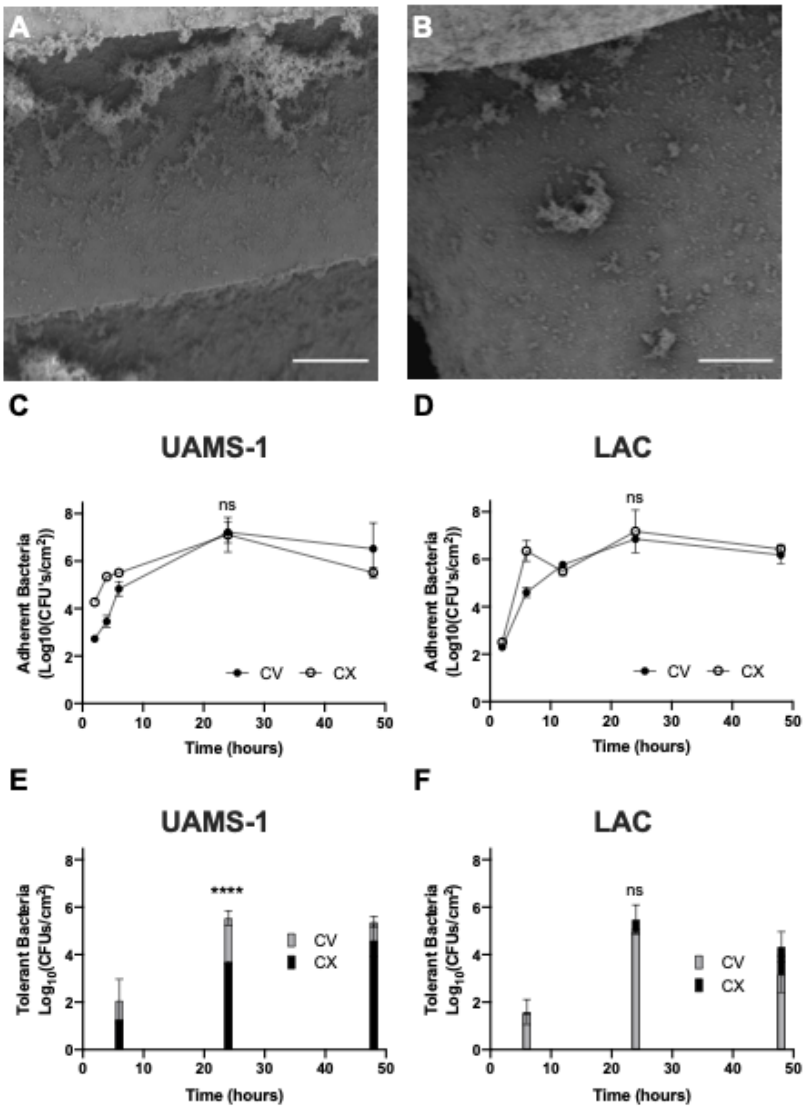

Figure 3.5. Colonization and antibiotic-recalcitrance on CV and CX substrates. Representative SEM images of UAMS-1 24h post-inoculation on CV (A) and CX (B) constructs. Scale bar = 100 μm. Adherent cells on CV and CX substrates analyzed by CFU cm^{-2} for UAMS-1 (C) and LAC (D) strains. N=3 for all time points. Tolerant UAMS-1 (E) and LAC (F) bacteria adherent to CV and CX substrates. **** represents $p < 0.0001$ as determined by student's t test. N=3 for all time points.

Effects of anatomic trabecular morphology on S. aureus *tolerance*

Given that surface morphology influences antibiotic tolerance development within UAMS-1 biofilm communities 24 h post-inoculation, we investigated the effect of trabecular morphology

on antibiotic tolerance using trabecular reconstructions published previously (28). UAMS-1 bacteria were inoculated on FH, PT, and VB reconstructions at a density of 10^5 CFUs cm^{-2} and incubated for 24 h prior to treatment with 100 μg/ml vancomycin. 2D plate surfaces as well as 3D CV and CX lattices were compared as controls. Bacteria attained similar surface densities of approximately 10^7-10^8 CFUs cm^{-2} across all morphologies (**Fig. 3.6**). Vancomycin-treated cells grown on the CX substrates demonstrated the lowest population of antibiotic-recalcitrant cells, with a surviving cell count $<10^4$ CFUs cm^{-2}. UAMS-1 bacteria grown on CV substrates exhibited communities with the highest population of antibiotic-recalcitrant cells. Bacteria adherent to PT and VB reconstructions exhibited substantially decreased antibiotic-recalcitrant communities compared to the CV substrate. Importantly, FH reconstructions did not demonstrate a substantially different antibiotic-recalcitrance compared to the CV substrate. Therefore, bacteria grown on PT and VB substrates are more susceptible to vancomycin exposure at 24 h post-inoculation.

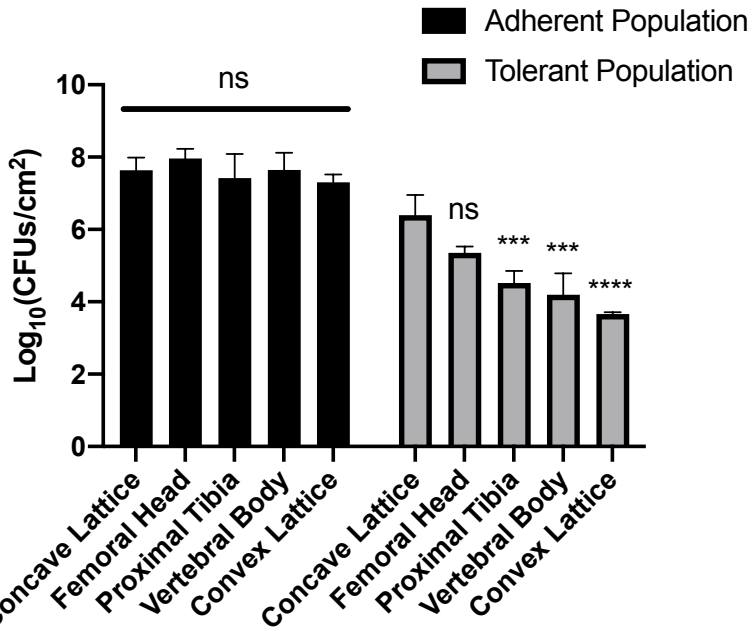

Figure 3.6. Antibiotic-recalcitrance on trabecular reconstructions at 24 h post-inoculation. Tolerant UAMS-1 bacteria on TEBC surfaces 24h post-inoculation. N=3 for all groups. *** represents $p < 0.001$, **** represents $p < 0.0001$ as determined by 2-way ANOVA with multiple comparisons.

Discussion

Bacterial biofilms in the bone microenvironment have been associated with the development of recurrent infections and osteomyelitis (43, 44). It is well known that a major complication in bacterial eradication is the antibiotic tolerance that manifests within biofilm communities (1). Current detection and identification techniques of biofilms *in vitro* include crystal violet imaging (16), confocal analysis (17, 18), and characterization of the extracellular matrix by qPCR or qRT-PCR (19-21). Although these methods are able to define the presence of adherent bacteria and characterize the cellular and extracellular composition of biofilm-like populations, further investigation is needed to determine the associated antibiotic tolerance within biofilm communities. Therefore, use of a clinically-relevant antibiotic such as vancomycin as a surrogate marker for antibiotic-tolerance may progress the understanding of biofilm development on various substrates and outline methods to improve contemporary therapeutics.

In this study, we evaluated biofilm development on 2D and 3D substrates using vancomycin as a surrogate biofilm marker. We identified the limited vancomycin binding within adherent communities as a secondary output for biofilm classification based on previous research suggesting cellular- or EPS-associated vancomycin tolerance within biofilm communities (17, 26). With the ability to functionally quantify tolerant biofilm communities, we hypothesized that biofilm development would be influenced by morphological properties of 3D substrates similar to previous studies that outlined the effect of morphology on bone cell activity (41, 45). Reconciling this hypothesis and potential outcome is important to understand i.) the influence of implant morphology on biofilm development and ii.) biofilm development on trabecular bone in various anatomical sites. We discovered that bacteria adherent to 3D substrates with greater Tb.Sp and SMI values resulted in a substantially reduced antibiotic-recalcitrant population compared to

substrates with lower Tb.Sp and SMI values. Because the adherent communities were similar at the time points tested, we can conclude that vancomycin susceptibility on 3D substrates is greater at 24 h post-colonization on morphologies exhibiting greater Tb.Sp and SMI values. Importantly, trabecular reconstructions representing a range of morphological properties correlating to different sites within the human anatomy also demonstrate an influence on biofilm development. Therefore, *S. aureus* develops biofilm communities with greater recalcitrance on concave surfaces with lower Tb.Sp properties based on the conditions of this study. Given that greater SMI and Tb.Sp results in decreased vancomycin-tolerant biofilm development 24 h post-inoculation, further investigation into morphological influence on tolerance should be performed to optimize implant substrates to decrease biofilm development on medical devices. Similarly, further investigation should be done to completely understand the timeline for antibiotic tolerance within biofilm communities on each substrate to establish an optimal substrate morphology that will allow for the efficacy of antibiotics to eradicate adherent bacteria at later time points post-inoculation. As biofilm research continues to develop an understanding of altered bacterial physiology within a biofilm, further research should be performed to characterize the mechanisms in which biofilm bacteria become recalcitrant.

Because the detection and treatment of biofilms remains a major challenge, an effective strategy to decrease biofilm-related disease is to inhibit the initial biofilm formation. Poly(ester-urethane) (PEUR) materials provide a bio-resorbable platform for regenerating bone tissue that circumnavigates infectious complications associated with non-resorbable materials such as poly(methyl methacrylate) PMMA bone cements (46-50); however, inhibiting infectious complications on PEUR surfaces is still a major research focus (8, 11, 51). Because the design of these biomaterials focuses on complete resorption and elimination from the body, eliminating biofilm colonization on the material surface at earlier timepoints is paramount. Antibiotic-loaded

PEUR foams have been shown to decrease bacterial burdens on the bone graft and surrounding area using a bolus release of antibiotics such as vancomycin from the polymer scaffold (8, 10, 11). However, the avascular scaffold provides a nidus for infection by bacteria not eliminated by the bolus antibiotic release (8, 51). Given that systemic antibiotic prophylaxis traditionally accompanies device implantation to prevent any biofilm formation, implantation of materials offering an extended timeline for effective bacterial removal by either systemic or device-released antibiotic therapy may decrease the number of biofilms formed on resorbable bone grafts. Further investigation into the impact of substrate morphology on bacterial communication is also important to understand biofilm development. Quorum quenching is currently being researched as a small molecule treatment method for preventing biofilm infections by targeting the quorum sensing locus in staphylococcal communities (52-56). While small molecule input is becoming better understood, the influence of substrate morphology on quorum sensing between bacteria is unknown. Therefore, further research into the morphologic input for antibiotic potentiation at later timepoints, the mechanism of action for tolerance development within biofilm communities, and the morphologic effect on quorum sensing is necessary and possible with this antibiotic-focused biofilm assay.

Limitations of this study include the use of only one antibiotic, investigation of biofilm formation using only one bacterial species, and the evaluation of a single time point for bacterial tolerance on TEBCs. Future studies should extend the investigative capabilities of this assay to define biofilm formation using other antibiotics to gain further understanding of biofilm recalcitrance timelines and time-dependent tolerance profiles to other clinically-used compounds. Similarly, use of this model to understand the colonization and development of biofilms by other bacterial species should be investigated. Although vancomycin binding was used as a surrogate

marker for biofilm classification in this model, the precise mechanisms of antibiotic tolerance within biofilms remains a major research focus. Moreover, investigation of bacteria that are adherent to morphologically-unique 3D substrates *in vivo* will be performed to characterize antibiotic activity in combination with the immune system.

References

1. Hall-Stoodley L, Costerton JW, Stoodley P. 2004. Bacterial biofilms: from the natural environment to infectious diseases. Nat Rev Microbiol 2:95-108.
2. Luppens SB, Reij MW, van der Heijden RW, Rombouts FM, Abee T. 2002. Development of a standard test to assess the resistance of Staphylococcus aureus biofilm cells to disinfectants. Appl Environ Microbiol 68:4194-200.
3. O'Gara JP, Humphreys H. 2001. Staphylococcus epidermidis biofilms: importance and implications. J Med Microbiol 50:582-7.
4. Zimmerli W, Waldvogel FA, Vaudaux P, Nydegger UE. 1982. Pathogenesis of foreign body infection: description and characteristics of an animal model. J Infect Dis 146:487-97.
5. Roosjen A, van der Mei HC, Busscher HJ, Norde W. 2004. Microbial adhesion to poly(ethylene oxide) brushes: influence of polymer chain length and temperature. Langmuir 20:10949-55.
6. Roe D, Karandikar B, Bonn-Savage N, Gibbins B, Roullet JB. 2008. Antimicrobial surface functionalization of plastic catheters by silver nanoparticles. J Antimicrob Chemother 61:869-76.
7. Stevens KN, Crespo-Biel O, van den Bosch EE, Dias AA, Knetsch ML, Aldenhoff YB, van der Veen FH, Maessen JG, Stobberingh EE, Koole LH. 2009. The relationship between the antimicrobial effect of catheter coatings containing silver nanoparticles and the coagulation of contacting blood. Biomaterials 30:3682-90.
8. Guelcher SA, Brown KV, Li B, Guda T, Lee BH, Wenke JC. 2011. Dual-purpose bone grafts improve healing and reduce infection. J Orthop Trauma 25:477-82.
9. Hafeman AE, Zienkiewicz KJ, Carney E, Litzner B, Stratton C, Wenke JC, Guelcher SA. 2010. Local delivery of tobramycin from injectable biodegradable polyurethane scaffolds. J Biomater Sci Polym Ed 21:95-112.
10. Li B, Brown KV, Wenke JC, Guelcher SA. 2010. Sustained release of vancomycin from polyurethane scaffolds inhibits infection of bone wounds in a rat femoral segmental defect model. J Control Release 145:221-30.
11. Wenke JC, Guelcher SA. 2011. Dual delivery of an antibiotic and a growth factor addresses both the microbiological and biological challenges of contaminated bone fractures. Expert Opin Drug Deliv 8:1555-69.
12. Cram P, Lu X, Kates SL, Singh JA, Li Y, Wolf BR. 2012. Total knee arthroplasty volume, utilization, and outcomes among Medicare beneficiaries, 1991-2010. JAMA 308:1227-36.
13. Kurtz SM, Lau E, Schmier J, Ong KL, Zhao K, Parvizi J. 2008. Infection burden for hip and knee arthroplasty in the United States. J Arthroplasty 23:984-91.
14. Schwarz EM, Parvizi J, Gehrke T, Aiyer A, Battenberg A, Brown SA, Callaghan JJ, Citak M, Egol K, Garrigues GE, Ghert M, Goswami K, Green A, Hammound S, Kates SL, McLaren AC, Mont MA, Namdari S, Obremskey WT, O'Toole R, Raikin S, Restrepo C, Ricciardi B, Saeed K, Sanchez-Sotelo J, Shohat N, Tan T, Thirukumaran CP, Winters B. 2019. 2018 International

Consensus Meeting on Musculoskeletal Infection: Research Priorities from the General Assembly Questions. J Orthop Res 37:997-1006.
15. Stulberg JJ, Delaney CP, Neuhauser DV, Aron DC, Fu P, Koroukian SM. 2010. Adherence to surgical care improvement project measures and the association with postoperative infections. JAMA 303:2479-85.
16. Merritt JH, Kadouri DE, O'Toole GA. 2005. Growing and analyzing static biofilms. Curr Protoc Microbiol Chapter 1:Unit 1B 1.
17. Jefferson KK, Goldmann DA, Pier GB. 2005. Use of confocal microscopy to analyze the rate of vancomycin penetration through Staphylococcus aureus biofilms. Antimicrob Agents Chemother 49:2467-73.
18. Schlafer S, Meyer RL. 2017. Confocal microscopy imaging of the biofilm matrix. J Microbiol Methods 138:50-59.
19. Atshan SS, Shamsudin MN, Karunanidhi A, van Belkum A, Lung LT, Sekawi Z, Nathan JJ, Ling KH, Seng JS, Ali AM, Abduljaleel SA, Hamat RA. 2013. Quantitative PCR analysis of genes expressed during biofilm development of methicillin resistant Staphylococcus aureus (MRSA). Infect Genet Evol 18:106-12.
20. Magalhaes AP, Franca A, Pereira MO, Cerca N. 2019. RNA-based qPCR as a tool to quantify and to characterize dual-species biofilms. Sci Rep 9:13639.
21. Perez-Osorio AC, Franklin MJ. 2008. qRT-PCR of Microbial Biofilms. CSH Protoc 2008:pdb prot5066.
22. Stewart PS. 1996. Theoretical aspects of antibiotic diffusion into microbial biofilms. Antimicrob Agents Chemother 40:2517-22.
23. Stewart PS, White B, Boegli L, Hamerly T, Williamson KS, Franklin MJ, Bothner B, James GA, Fisher S, Vital-Lopez FG, Wallqvist A. 2019. Conceptual Model of Biofilm Antibiotic Tolerance that Integrates Phenomena of Diffusion, Metabolism, Gene Expression, and Physiology. J Bacteriol doi:10.1128/JB.00307-19.
24. Stewart PS. 2003. Diffusion in biofilms. J Bacteriol 185:1485-91.
25. Stewart PS. 1998. A review of experimental measurements of effective diffusive permeabilities and effective diffusion coefficients in biofilms. Biotechnol Bioeng 59:261-72.
26. Lewis K. 2010. Persister cells. Annu Rev Microbiol 64:357-72.
27. Lechner S, Lewis K, Bertram R. 2012. Staphylococcus aureus persisters tolerant to bactericidal antibiotics. J Mol Microbiol Biotechnol 22:235-44.
28. Vanderburgh JP, Fernando SJ, Merkel AR, Sterling JA, Guelcher SA. 2017. Fabrication of Trabecular Bone-Templated Tissue-Engineered Constructs by 3D Inkjet Printing. Adv Healthc Mater 6.
29. Zadpoor AA. 2015. Bone tissue regeneration: the role of scaffold geometry. Biomater Sci 3:231-45.
30. Arciola CR, An YH, Campoccia D, Donati ME, Montanaro L. 2005. Etiology of implant orthopedic infections: a survey on 1027 clinical isolates. Int J Artif Organs 28:1091-100.
31. Darouiche RO. 2004. Treatment of infections associated with surgical implants. N Engl J Med 350:1422-9.
32. Pulido L, Ghanem E, Joshi A, Purtill JJ, Parvizi J. 2008. Periprosthetic joint infection: the incidence, timing, and predisposing factors. Clin Orthop Relat Res 466:1710-5.
33. Levine DP. 2008. Vancomycin: understanding its past and preserving its future. South Med J 101:284-91.
34. Levine JF. 1987. Vancomycin: a review. Med Clin North Am 71:1135-45.
35. Boles BR, Thoendel M, Roth AJ, Horswill AR. 2010. Identification of genes involved in polysaccharide-independent Staphylococcus aureus biofilm formation. PLoS One 5:e10146.
36. Diekema DJ, Richter SS, Heilmann KP, Dohrn CL, Riahi F, Tendolkar S, McDanel JS, Doern GV. 2014. Continued emergence of USA300 methicillin-resistant Staphylococcus aureus in the United States: results from a nationwide surveillance study. Infect Control Hosp Epidemiol

35:285-92.
37. Gillaspy AF, Hickmon SG, Skinner RA, Thomas JR, Nelson CL, Smeltzer MS. 1995. Role of the accessory gene regulator (agr) in pathogenesis of staphylococcal osteomyelitis. Infect Immun 63:3373-80.
38. Guo R, Lu S, Page JM, Merkel AR, Basu S, Sterling JA, Guelcher SA. 2015. Fabrication of 3D Scaffolds with Precisely Controlled Substrate Modulus and Pore Size by Templated-Fused Deposition Modeling to Direct Osteogenic Differentiation. Adv Healthc Mater 4:1826-32.
39. McGuinness WA, Malachowa N, DeLeo FR. 2017. Vancomycin Resistance in Staphylococcus aureus. Yale J Biol Med 90:269-281.
40. Stewart PS. 2002. Mechanisms of antibiotic resistance in bacterial biofilms. Int J Med Microbiol 292:107-13.
41. Vanderburgh J, Sterling JA, Guelcher SA. 2017. 3D Printing of Tissue Engineered Constructs for In Vitro Modeling of Disease Progression and Drug Screening. Ann Biomed Eng 45:164-179.
42. Hildebrand T, Ruegsegger P. 1997. Quantification of Bone Microarchitecture with the Structure Model Index. Comput Methods Biomech Biomed Engin 1:15-23.
43. Costerton W, Veeh R, Shirtliff M, Pasmore M, Post C, Ehrlich G. 2003. The application of biofilm science to the study and control of chronic bacterial infections. J Clin Invest 112:1466-77.
44. Wolcott RD, Rhoads DD, Bennett ME, Wolcott BM, Gogokhia L, Costerton JW, Dowd SE. 2010. Chronic wounds and the medical biofilm paradigm. J Wound Care 19:45-6, 48-50, 52-3.
45. Vanderburgh JP, Guelcher SA, Sterling JA. 2018. 3D bone models to study the complex physical and cellular interactions between tumor and the bone microenvironment. J Cell Biochem 119:5053-5059.
46. Guelcher SA, Patel V, Gallagher KM, Connolly S, Didier JE, Doctor JS, Hollinger JO. 2006. Synthesis and in vitro biocompatibility of injectable polyurethane foam scaffolds. Tissue Eng 12:1247-59.
47. Li B, Davidson JM, Guelcher SA. 2009. The effect of the local delivery of platelet-derived growth factor from reactive two-component polyurethane scaffolds on the healing in rat skin excisional wounds. Biomaterials 30:3486-94.
48. Li B, Yoshii T, Hafeman AE, Nyman JS, Wenke JC, Guelcher SA. 2009. The effects of rhBMP-2 released from biodegradable polyurethane/microsphere composite scaffolds on new bone formation in rat femora. Biomaterials 30:6768-79.
49. Talley AD, Boller LA, Kalpakci KN, Shimko DA, Cochran DL, Guelcher SA. 2018. Injectable, compression-resistant polymer/ceramic composite bone grafts promote lateral ridge augmentation without protective mesh in a canine model. Clin Oral Implants Res 29:592-602.
50. Talley AD, Kalpakci KN, Shimko DA, Zienkiewicz KJ, Cochran DL, Guelcher SA. 2016. Effects of Recombinant Human Bone Morphogenetic Protein-2 Dose and Ceramic Composition on New Bone Formation and Space Maintenance in a Canine Mandibular Ridge Saddle Defect Model. Tissue Eng Part A 22:469-79.
51. Spoonmore TJ, Ford CA, Curry JM, Guelcher SA, Cassat JE. 2020. Concurrent local delivery of diflunisal limits bone destruction but fails to improve systemic vancomycin efficacy during Staphylococcus aureus osteomyelitis. Antimicrob Agents Chemother doi:10.1128/AAC.00182-20.
52. Cech NB, Horswill AR. 2013. Small-molecule quorum quenchers to prevent Staphylococcus aureus infection. Future Microbiol 8:1511-4.
53. Harraghy N, Kerdudou S, Herrmann M. 2007. Quorum-sensing systems in staphylococci as therapeutic targets. Anal Bioanal Chem 387:437-44.
54. Kaufmann GF, Park J, Janda KD. 2008. Bacterial quorum sensing: a new target for anti-infective immunotherapy. Expert Opin Biol Ther 8:719-24.
55. Khan BA, Yeh AJ, Cheung GY, Otto M. 2015. Investigational therapies targeting quorum-sensing for the treatment of Staphylococcus aureus infections. Expert Opin Investig Drugs 24:689-704.

56. Martin CA, Hoven AD, Cook AM. 2008. Therapeutic frontiers: preventing and treating infectious diseases by inhibiting bacterial quorum sensing. Eur J Clin Microbiol Infect Dis 27:635-42.

Supplementary Figures:

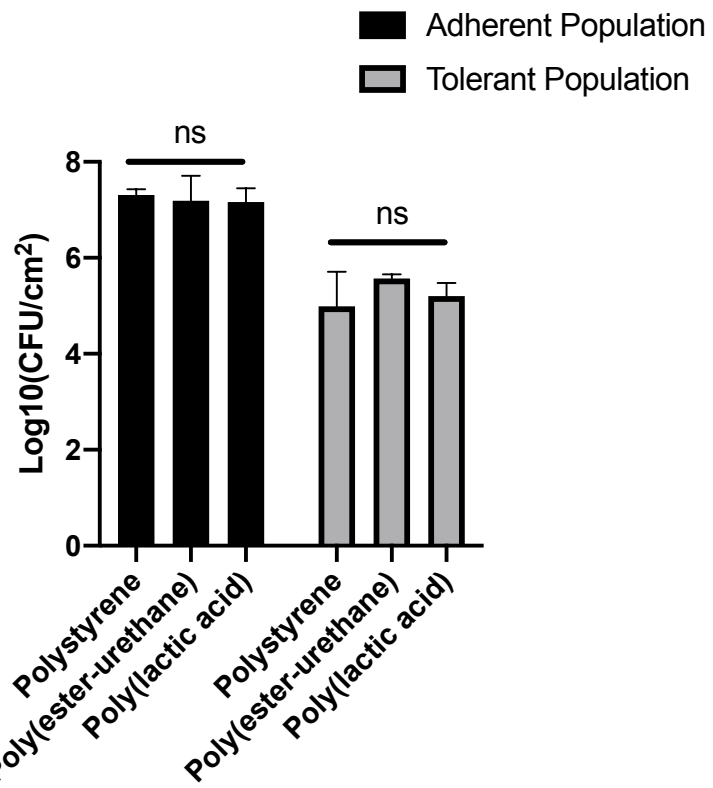

Supplementary Figure 3.1. Substrate material chemistry does not influence colonization density or vancomycin tolerance in vitro 24 h post-inoculation. Bacteria were grown on 2D substrates of polystyrene, poly(ester-urethane), and poly(lactic acid) for 24 h and subsequently treated with 100 μg/ml vancomycin. Adherent and tolerant communities were assessed as before. Ns denotes no significance as determined by Student's t test. N=3.

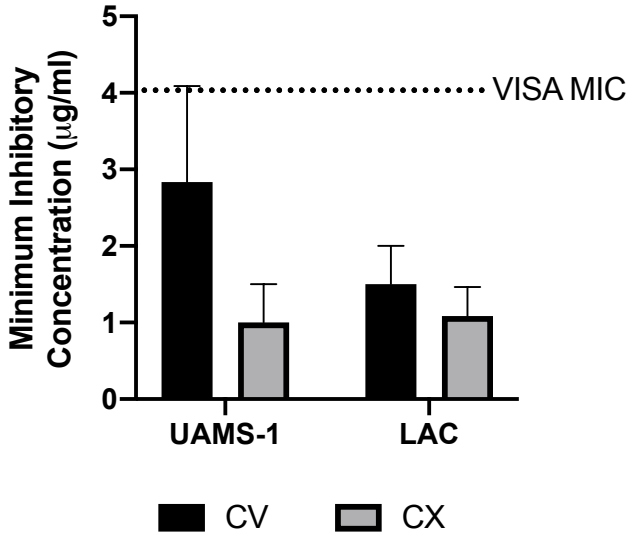

Supplementary Figure 3.2. UAMS-1 and LAC bacteria do not demonstrate resistance-associated MIC values 24 h post-inoculation. Bacteria grown on CV and CX substrates were characterized by vancomycin MIC using vancomycin E-test strips. Dotted line represents the MIC of vancomycin intermediate *S. aureus* MIC. N=3.

CHAPTER 4

REPURPOSING THE NONSTEROIDAL ANTI-INFLAMMATORY DRUG DIFLUNISAL AS A CONJUNCTIVE ANTI-VIRULENCE THERAPY FOR *STAPHYLOCOCCUS AUREUS* OSTEOMYELITIS

Repurposing the nonsteroidal anti-inflammatory drug diflunisal as an osteoprotective, anti-virulence therapy for *Staphylococcus aureus* osteomyelitis.

Adapted from:

> Hendrix AS, **Spoonmore TJ**, et al. Repurposing the Nonsteroidal Anti-inflammatory Drug Diflunisal as an Osteoprotective, Antivirulence Therapy for Staphylococcus aureus Osteomyelitis. *Antimicrob Agents Chemother*. 2016;60(9):5322–5330. Published 2016 Aug 22.

Abstract

Staphylococcus aureus osteomyelitis is a common and debilitating invasive infection of bone. Treatment of osteomyelitis is confounded by widespread antimicrobial resistance and the propensity of bacteria to trigger pathologic changes in bone remodeling that limit antimicrobial penetration to the infectious focus. Adjunctive therapies that limit pathogen-induced bone destruction could therefore limit morbidity and enhance traditional antimicrobial therapies. In this study, we evaluate the efficacy of the FDA-approved, nonsteroidal anti-inflammatory (NSAID) compound diflunisal in limiting *S. aureus* cytotoxicity toward skeletal cells, and in preventing bone destruction during staphylococcal osteomyelitis. Diflunisal is known to inhibit *S. aureus* virulence factor production by the accessory gene regulator (*agr*) locus, and we have previously demonstrated that the Agr system plays a substantial role in pathologic bone remodeling during staphylococcal osteomyelitis. Consistent with these observations, we find that diflunisal potently inhibits osteoblast cytotoxicity caused by *S. aureus* secreted toxins independently of effects on bacterial growth. Compared to commonly used NSAIDs, diflunisal is uniquely potent in the inhibition of skeletal cell death *in vitro*. Moreover, local delivery of

diflunisal by means of a drug-eluting, bioresorbable foam significantly limits bone destruction during *S. aureus* osteomyelitis *in vivo*. Collectively, these data demonstrate that diflunisal potently inhibits skeletal cell death and bone destruction associated with *S. aureus* infection, and may therefore be a useful adjunctive therapy for osteomyelitis.

Introduction

Osteomyelitis is an invasive infection of bone, most frequently caused by the Gram-positive pathogen *Staphylococcus aureus* (1). Treatment of osteomyelitis is confounded by an increasing prevalence of antimicrobial resistance, as well as the propensity for patients to develop pathologic changes in bone remodeling that limit antimicrobial penetration to the infectious focus. For this reason, patients suffering from osteomyelitis often undergo multiple surgical debridements to remove infected and necrotic bone, while also receiving prolonged antimicrobial therapy (1, 2). Despite these aggressive measures, a subset of patients with acute osteomyelitis will progress to chronic infection, which is highly refractory to further intervention and may require months to years of antimicrobial treatment. Moreover, although adult osteomyelitis is often secondary to comorbidities such as trauma, surgery, diabetes, or vascular insufficiency, hematogenous osteomyelitis in previously healthy children is more prevalent in the current era of community-acquired staphylococcal infections (3). Children are inherently vulnerable to adverse outcomes during osteomyelitis given the presence of active epiphyseal plates, and thus have the potential to develop limb-length discrepancy (4). Taken together, these facts illustrate the need for adjunctive therapies that lessen the morbidity of staphylococcal osteomyelitis and promote the efficacy of traditional antimicrobials through inhibition of destructive bone remodeling.

S. aureus is capable of producing numerous virulence factors, including host-binding

proteins, secreted toxins and superantigens, degradative enzymes, and immune evasion factors. We recently defined the secreted alpha-type phenol soluble modulins (PSMs) as key contributors to the pathogenesis of staphylococcal osteomyelitis (5). Alpha PSMs were both necessary and sufficient to elicit destruction of osteoblasts, the skeletal cells responsible for synthesis of new bone and regulation of bone-resorbing osteoclasts. Moreover, inactivation of the alpha-type PSMs led to significantly decreased bone destruction in a murine model of *S. aureus* osteomyelitis, despite not having a significant effect on bacterial burdens. Production of PSMs in *S. aureus* is regulated by the accessory gene regulator protein AgrA, which is a component of the quorum-sensing *agr* regulatory locus. In contrast to most *agr*-regulated virulence factors, the PSMs are regulated directly by AgrA, rather than via the regulatory RNA molecule *RNAIII* (6). Accordingly, inactivation of the *agr* locus also leads to a significant reduction in bone destruction during osteomyelitis (5). These data suggest that the *agr* locus might be an attractive target for adjunctive therapies that lessen the morbidity of staphylococcal osteomyelitis.

To date, a number of studies have shown preclinical efficacy of *agr* inhibitory compounds in limiting *S. aureus* virulence (7-10). One such study identified the FDA-approved nonsteroidal anti-inflammatory drug (NSAID) diflunisal as a potent inhibitor of AgrA-mediated transcriptional regulation (11). In an *in silico* screen, diflunisal was predicted to inhibit AgrC-mediated phosphorylation of AgrA. Consistent with this prediction, diflunisal treatment inhibited rabbit red blood cell lysis, and significantly lowered transcript levels of *hla, RNAIII, and psm*α without affecting bacterial growth (7, 11). However, the efficacy of diflunisal in mitigating staphylococcal virulence *in vivo* has yet to be determined.

Based on the critical role of *agr*-regulated virulence factors in the pathogenesis of staphylococcal osteomyelitis, we hypothesized that diflunisal treatment would limit skeletal cell

death and cortical bone destruction during *S. aureus* infection. Here we test this hypothesis by evaluating the effects of diflunisal and other commonly used NSAIDs on staphylococcal growth, virulence factor production, and host cell cytotoxicity. We also test the preclinical efficacy of local diflunisal therapy during staphylococcal osteomyelitis by synthesizing drug-eluting polyurethane foams for direct delivery to infected bone. Collectively, our results suggest that diflunisal treatment is a promising strategy for adjunctive therapy of osteomyelitis given its osteoprotective and anti-virulence properties.

Materials and Methods

Bacterial strains, reagents, and growth conditions

An erythromycin-sensitive derivative of the USA300-lineage strain LAC was used for all experiments unless otherwise noted (12). Strain Newman was also used to test whether diflunisal could limit the cytotoxic potential of other clinical strains of *S. aureus* (13). For growth curve analysis, overnight cultures were back-diluted 1:1000 into Tryptic Soy Broth (TSB) supplemented with various NSAIDs or vehicle control. Cultures were grown in glass Erlenmeyer flasks at 37°C and 180 rpm shaking at a flask to volume ratio of 5:1. Optical density at 600 nm (OD_{600}) was measured at the indicated timepoints. Diflunisal, ibuprofen, ketorolac, piroxicam, and salicylic acid were purchased from Sigma and dissolved in either 100% ethanol or dimethyl sulfoxide (DMSO) at a final concentration of 10 mg/ml. PSMα2 was synthesized to >95% purity by AAPPTec (Louisville, KY) and resuspended in DMSO. Lysine triisocyanate (LTI) was purchased from Kyowa Hakko USA (New York, NY) and contained 42.2% NCO. For polyester triol synthesis, ε-caprolactone and stannous octoate were purchased from Sigma-Aldrich, and D,L-lactide and glycolide were purchased from Polysciences (Warrington, PA). Triethylene diamine

(TEDA) catalyst was received from Goldschmidt (TEGOAMIN33, Hopewell, VA). All other reagents including calcium stearate and turkey red oil were purchased from Sigma-Aldrich.

Osteoblast cell culture

Primary human osteoblasts were obtained from Lonza (Basel, Switzerland) and cultured per manufacturer's recommendations. To isolate primary murine osteoblasts, murine femurs were extracted, bone marrow was flushed, and the diaphysis was cut into small pieces. The bone pieces were digested twice in 0.01% Trypsin-EDTA and 2mg/ml collagenase for 30 minutes at 37°C. Following digestion, bone pieces were plated in αMEM supplemented with 10% fetal bovine serum (FBS), and cells were allowed to migrate from the bone for 10-14 days prior to harvest and plating for cytotoxicity assays. Cell lines were obtained from the American Type Culture Collection (ATCC) and propagated at 37°C and 5% CO_2 according to ATCC recommendations. Media was replaced every 2-3 days. All cell culture media was prepared with 1X penicillin/streptomycin and sterilized using a 0.22 μm filter prior to use. MC3T3 E-1 murine osteoblastic cells were cultured in α-MEM, supplemented with 10% FBS. Saos-2 human osteoblastic cells were grown in McCoy's 5A medium with 15% FBS. The following cell densities were used for cytotoxicity assays: MC3T3 E1 murine pre-osteoblastic cells and primary murine osteoblasts at 5,000 cells per well, Saos-2 human osteoblastic cells at 10,000 cells per well, and primary human osteoblasts at 3,500 cells per well.

Preparation of concentrated supernatants

To prepare concentrated bacterial supernatants, 3 colonies were inoculated into triplicate 15 ml cultures in loosely-capped 50 ml conical tubes and grown for 15 hrs in RPMI supplemented with

1% casamino acids and various NSAIDs or vehicle control. For some experiments, bacteria were alternatively grown in glass Erlenmeyer flasks that were tightly sealed with a rubber stopper. Bacteria were grown for 15 hours at 37°C and 180 rpm, after which time triplicate cultures were combined, an aliquot was taken for colony forming unit (CFU) enumeration, and supernatants were harvested by centrifugation. Supernatants were sterilized by passage through a 0.22 μm filter, and then concentrated to a final volume of approximately 1.5 ml using Amicon Ultra 3 kD nominal molecular weight columns. Following concentration, supernatants were again filter sterilized and either used immediately or frozen at -80°C. For some experiments, 100 μg/ml of synthetic PSMα2 was added to concentrated supernatants prior to intoxication of cells.

Osteoblast cytotoxicity assay

The cytotoxic potential of concentrated supernatants towards MC3T3-E1 murine osteoblastic cells, Saos-2 human osteoblastic cells, primary murine osteoblasts, and primary human osteoblasts was determined as previously described (5, 14). Briefly, cells were seeded into 96-well tissue culture plates 12-24 hours prior to intoxication and grown at 37°C and 5% CO_2. Tissue culture media was then replaced with fresh media containing various concentrations of concentrated supernatants. Cells were incubated an additional 22 hours, at which time cell viability was determined using CellTiter AQueous One solution (Promega, Madison, WI) according to manufacturer's instructions. For some experiments, diflunisal was added to the cell culture medium at the time of intoxication at a final concentration of either 10 μg/ml.

Synthesis of polyurethane (PUR) foams for local drug delivery

LTI, tertiary amine catalyst, polyester triol, and turkey red oil were all dried at 10mm Hg for 3

hours at 80°C to avoid excess amounts of water during PUR foam synthesis. The polyol component (70% ε-caprolactone, 20% glycolide, 10% lactide) of the PUR foam comprised a polyester triol of 900 g/mol that was synthesized using previously published techniques (15, 16). Appropriate amounts of ε-caprolactone, glycolide, D,L-lactide, dried glycerol, and stannous octoate were mixed in a 250 mL round bottom flask and stirred under dry argon for 36 hours at 140°C. The polyol was then washed with hexane and vacuum-dried at 80°C for 14 hours. Foams were synthesized using a formulation that maintained constant ratios relative to the polyol component and premixed with diflunisal. Formulations of foams included 100 pphp (parts per hundred part polyol) polyol 7C2G1L900 mixed with 1.0 pphp Water, 4.5 pphp tertiary catalyst, 1.5 pphp turkey red oil, 6.0 pphp calcium stearate and the appropriate amount of LTI. Appropriate ratios of LTI and polyol were mixed to ensure foams contained targeted index values (100 × NCO equivalents / OH equivalents) of 115. Reactants were mixed in a 5 mL plastic container for 1.5 minutes using a Hauschild SpeedMixer DAC 150 FVZ-K vortex mixer (Flacktek) and left overnight to cure. The foams synthesized included blank foams and foams loaded with 10 mM diflunisal. Foams were cut into prisms (6 mm × 4.5 mm × 4.5 mm) for *in vivo* testing and sterilized by ethylene oxide (EO) treatment.

In vitro release kinetics of diflunisal PUR foams

Foams containing 10 mM (10.8 mg) of diflunisal were synthesized and cut into 4 equal slices. The foams were approximately 4.35 cm^3 before being cut into slices at approximate sizes of 1.09 cm^3. Each foam slice was then placed in a 65 mL vial and immersed in 60 mL of phosphate-buffered saline (PBS) solution. All vials were placed on a mixer and incubated at 37˚C. 50 mL samples were withdrawn at 4, 8, 24, 32, 48, 56, 72, and 144 hrs post incubation and replaced with 50 mL

of fresh PBS. The samples were kept at 4˚C until analyzed by HPLC using a system that contained a Waters 1525 binary pump and a 2487 Dual-Absorbance Detector at 255 nm. Samples were analyzed using published techniques (17). Diflunisal samples were eluted through an Xterra RP18 column containing 5 μm particle size and measured 4.6 mm diameter × 250 mm length. The mobile phase for this analysis contained a ratio A40:B60 of acetonitrile (A) and 50 mM acetate buffer (pH = 4.2) containing sodium acetate anhydrous and distilled water (B) flowing at 0.35 mL/min. The injection volume was 15 μl and the column temperature was maintained at 30°C.

Murine model of osteomyelitis

Osteomyelitis was induced in 7-8 week female C57BL/6J mice as previously described (5). An inoculum of $1x10^6$ colony-forming units (CFU) in 2 μl PBS was delivered into murine femurs. For evaluation of local diflunisal therapy, 6 mm × 4.5 mm × 4.5 mm PUR foams loaded with 10 mM diflunisal were fabricated, sterilized, and wrapped around the femur at the inoculation site and sutured into place. Empty PUR foams served as a mock treatment control. As a positive control for the feasibility of local therapy using PUR foams, 8% wt / wt vancomycin foams were synthesized and used in the osteomyelitis model. At various times post-infection, mice were euthanized and the infected femur was removed and either processed for CFU enumeration or imaged by micro-computed tomography (μCT). For CFU enumeration, femurs were homogenized in a Bullet Blender® (Next Advance, Averill, NY) using the Navy Bead Lysis Kit and plated at limiting dilution on Tryptic Soy Agar (TSA). Analysis of cortical bone destruction was determined by μCT imaging as previously described (5). Specifically, axial images of each femur were acquired with 5.0 μm voxels at 70 kV, 200 μA, 2000 projections per rotation, and an integration time of 350 msec in a 10.24 mm field-of-view. Each imaging scan comprised 1635 slices (8.125

mm) of the length of the femur, centered on the inoculation site as visualized in the scout-view radiographs. A volume of interest (VOI) including only the original cortical bone and any destruction was selected by drawing inclusive contours on the periosteal surface and excluding contours on the endosteal surface. New bone formed during the course of infection was excluded from this analysis. This process was repeated iteratively for all of the 1635 slices of the μCT scan (comprising the entire diaphysis) using the manufacturer's analytical software. Volume of cortical bone destruction was determined by segmenting the image with a lower threshold of 0 and an upper threshold of 595 mg HA/ccm, sigma 1.3 and support 1, to exclude bone in the analysis. The direct voxel counting method was used for all reported calculations in each analysis.

Statistical evaluation

Differences in cytotoxicity, cortical bone destruction, and CFU counts were analyzed by Student's *t* test. A p value of ≤ 0.05 was considered significant.

Results

Diflunisal inhibits S. aureus cytotoxicity toward human and murine osteoblasts without affecting bacterial growth.

In silico analyses identified the NSAID diflunisal as a potent inhibitor of AgrA-mediated gene expression (11). We previously demonstrated that Agr-dependent virulence factor production, and in particular synthesis of alpha-type PSMs, significantly contributes to skeletal cell death and bone destruction associated with *S. aureus* osteomyelitis (5, 14, 18). Accordingly, we hypothesized that diflunisal treatment would limit PSM production, and therefore abrogate osteoblast cytotoxicity. To test this hypothesis, a USA300-lineage strain of *S. aureus* was grown in the presence of various

concentrations of diflunisal or vehicle control, after which concentrated supernatants were prepared and tested for cytotoxicity towards murine and human osteoblasts. Treatment with diflunisal significantly limited the cytotoxicity of supernatant from strain LAC towards murine osteoblastic MC3T3 cells in a dose-dependent manner (**Fig. 4.1.1A**). Moreover, this effect was not strain-dependent, as diflunisal also significantly limited the cytotoxicity of supernatant from strain Newman (**Supp. Fig. 4.1.1A**). Diflunisal treatment also potently inhibited staphylococcal killing of human Saos-2 osteoblastic cells, primary murine osteoblasts, and primary human osteoblasts (**Fig. 4.1.1B**). The diminution of cytotoxicity in the presence of diflunisal was not a result of decreased bacterial density, as diflunisal treatment did not significantly affect staphylococcal growth kinetics (**Fig. 4.1.1C**). Collectively these data indicate that diflunisal treatment significantly limits the ability of *S. aureus* to destroy osteoblasts.

During the completion of these experiments, we discovered that oxygenation significantly impacts the cytotoxic potential of *S. aureus* cultures (14). Specifically, growth of *S. aureus* in tightly capped Erlenmeyer flasks, and thus lower oxygenation, led to enhanced cytotoxicity relative to culture in flasks loosely covered by foil. We therefore conducted additional assays to test whether diflunisal could inhibit the cytotoxic potential of staphylococcal cultures grown under altered oxygenation. In staphylococcal cultures grown in tightly capped flasks, diflunisal still significantly inhibited the cytotoxicity of concentrated supernatants toward MC3T3 cells (**Supp. Fig. 4.1.1B**). This result suggests that diflunisal can inhibit staphylococcal virulence factor production under conditions of lower oxygenation, and therefore may have efficacy in the hypoxic environment of infected bone.

Replenishment of alpha-type PSMs restores cytotoxicity to diflunisal-treated S. aureus

supernatants

Structural modeling predicted that diflunisal binds to AgrA and inhibits phosphorylation by AgrC, thereby halting quorum sensing and virulence factor production (11). Given the critical role of AgrA in transcription of the alpha-type PSMs (6), we reasoned that supplementation of diflunisal-treated staphylococcal supernatants with alpha-type PSMs would restore cytotoxicity toward osteoblasts. Three of the alpha-type PSMs were previously noted to be dose-dependently cytotoxic toward osteoblasts, with PSMα2 being most potent (5). To test if PSM supplementation could restore cytotoxicity to diflunisal-treated *S. aureus*, synthetic PSMα2 was added to concentrated supernatants harvested from diflunisal-treated cultures. Supplementation with PSMα2 restored the cytotoxicity of diflunisal-treated supernatants toward both MC3T3 cells and primary human osteoblasts (**Fig. 4.1.1D**), providing further evidence that the anti-virulence effects of diflunisal reflect AgrA inhibition.

Treatment of host cells with diflunisal fails to prevent staphylococcal osteoblast cytotoxicity

Diflunisal treatment significantly inhibits *S. aureus*-induced osteoblast cell death. However, given that this drug is an anti-inflammatory compound, it is possible that diflunisal treatment modulates host cell death in a manner that is partially independent of bacterial factors. To investigate this possibility, supernatants were prepared from *S. aureus* cultures grown in the absence of diflunisal. The supernatants were subsequently combined with fresh cell culture media containing diflunisal or vehicle control, and then applied to osteoblast cell monolayers to assess cytotoxicity. Supplementation of cell culture media with diflunisal failed to inhibit the cytotoxicity of diflunisal-naïve *S. aureus* supernatants (**Fig. 4.1.2**). Thus, inhibition of staphylococcal cytotoxicity by diflunisal is largely independent of anti-inflammatory effects on host cells.

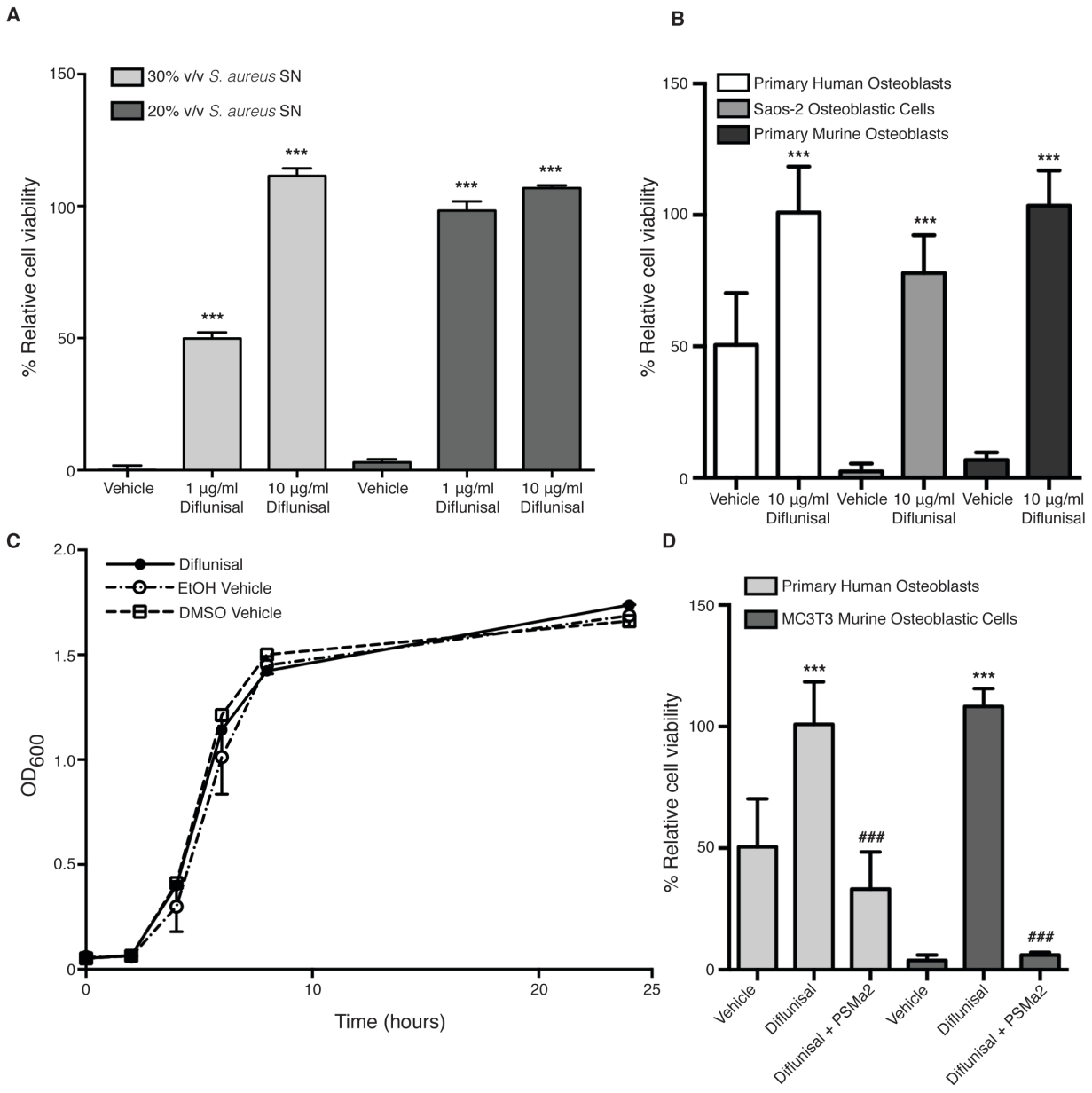

Figure 4.1.1. Diflunisal inhibits *S. aureus* cytotoxicity toward human and murine osteoblasts without affecting bacterial growth. (A) MC3T3 murine osteoblastic cells were intoxicated with 20% or 30% volume / volume (v/v) of concentrated supernatant (SN) from *S. aureus* grown in the presence of vehicle control (DMSO) or the indicated concentrations of diflunisal. Percent cell viability is depicted relative to mock intoxication with sterile RPMI. Error bars represent SD. N=5 per group and data are representative of three independent trials. *** denotes $p<0.001$ relative to vehicle control. (B) Same as (A), except that Saos-2 human osteoblastic cells, primary murine osteoblasts, or primary human osteoblasts were intoxicated with 30% v/v concentrated SN. N=10 and data are representative of at least 2 independent trials. Error bars represent SD. *** denotes $p<0.001$ relative to vehicle control. (C) Growth analysis (Optical density at 600nm = OD_{600}) of *S. aureus* cultured in glass Erlenmeyer flasks with a 1:5 volume to flask ratio, and in the presence of two different vehicle controls (100% ethanol or DMSO) or 10 µg/ml diflunisal. Error bars represent SD. (D) Same as (B), except that 100 µg/ml of synthetic PSMα2 was added to concentrated supernatant prior to intoxication of primary human osteoblasts or MC3T3 cells. Cells were treated with vehicle (DMSO) or 10 µg/ml diflunisal. N=10 and data are representative of 2 independent trials. Error bars represent SD. *** denotes $p<0.001$ relative to vehicle control and ### denotes $p<0.001$ relative to diflunisal treated cells without PSMα2.

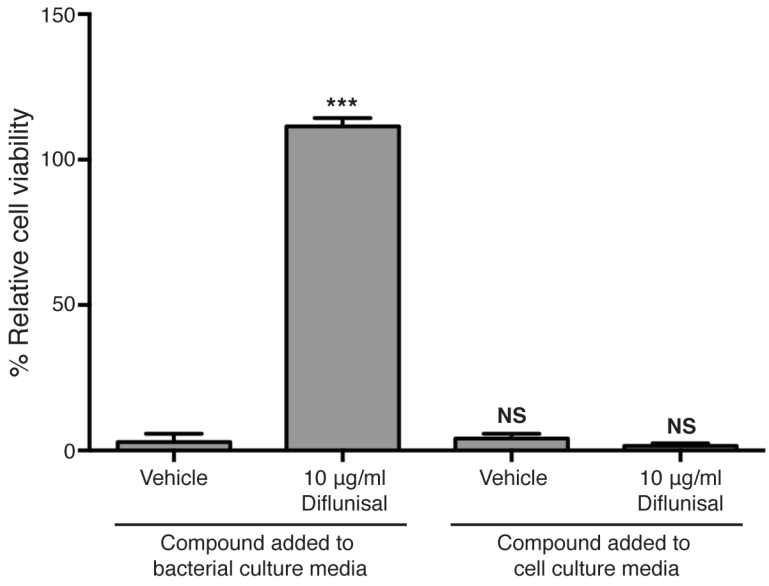

Figure 4.1.2. Supplementation of host cells with diflunisal does not inhibit cytotoxicity of untreated *S. aureus* supernatant. MC3T3 cells were intoxicated with concentrated supernatant from *S. aureus* grown in the presence (left) or absence (right) of vehicle control (DMSO) or 10 µg/ml diflunisal. Host cells were then cultured in the absence (left) or presence (right) of vehicle control (DMSO) or 10 µg/ml diflunisal. More specifically, fresh diflunisal or DMSO-supplemented cell culture media was added back to the cell monolayers at the time of intoxication with concentrated supernatant. N=5 per group and data are representative of two independent trials. Error bars represent SD. *** denotes $p<0.001$ relative to vehicle control. NS = not significant.

Potent inhibition of S. aureus cytotoxicity towards osteoblasts is unique to diflunisal

Diflunisal is a member of the salicylate class of non-steroidal anti-inflammatory compounds. It was therefore postulated that other NSAIDs with similar chemical properties might also inhibit staphylococcal cytotoxicity toward osteoblasts. To test this, a panel of commonly used anti-inflammatory drugs representing the major classes of NSAIDs was tested for the ability to limit *S. aureus* cytotoxicity. Aspirin (salicylate class), its active metabolite salicylic acid, ibuprofen (propionic acid derivative class), ketorolac (acetic acid derivative class), and piroxicam (enolic acid derivative class) were included in the analysis. All compounds except piroxicam were tested

using two different solvents, DMSO and 100% ethanol. Piroxicam was only soluble in DMSO at 10 mg/ml. None of the compounds significantly inhibited *S. aureus* growth at 10 μg/ml (**Supp. Fig. 4.1.2**). Interestingly, although these compounds share similar mechanisms of action, only diflunisal potently inhibited staphylococcal cytotoxicity toward osteoblastic cells (**Fig. 4.1.3A-B**). Piroxicam partially inhibited cytotoxicity at 10 μg/ml (**Fig. 4.1.3B**), but also caused the most pronounced lag in exponential growth (**Supp. Fig. 4.1.2**). Salicylic acid modestly inhibited cytotoxicity when dissolved in ethanol at a concentration of 50 μg/ml (**Fig. 4.1.3C**), which is consistent with previous reports showing efficacy of this compound in limiting staphylococcal virulence factor production (19-21). To further investigate the relative potency of diflunisal, piroxicam, and salicylic acid in preventing cytotoxicity, dose-response studies were performed using 10, 25, 50, or 100 μg/ml of each compound dissolved in DMSO. Diflunisal potently inhibited cytotoxicity toward MC3T3 cells at all concentrations tested (**Fig. 4.1.3D**). Salicylic acid did not inhibit cytotoxicity at any of the tested concentrations, suggesting that its effects on staphylococcal virulence may be solvent-dependent. Piroxicam again inhibited cytotoxicity at higher concentrations (**Fig. 4.1.3D**), but growth curve analysis indicated that this diminution of cytotoxicity was likely related to inhibition of bacterial growth (**Fig. 4.1.3E**). Diflunisal also inhibited bacterial growth at concentrations above 50 μg/ml. Collectively, these data indicate that diflunisal potently inhibits staphylococcal cytotoxicity toward osteoblasts, likely reflecting the important role of AgrA and alpha-type PSMs in inducing cell death of these host cells.

PUR drug delivery foams are effective as local therapies for experimental osteomyelitis

Given the potent blockade of PSM-induced osteoblast cell death by diflunisal *in vitro*, we sought to test whether diflunisal would limit the pathogenesis of *S. aureus* osteomyelitis *in vivo* in a murine model. We reasoned that a local drug delivery system would achieve clinical efficacy while

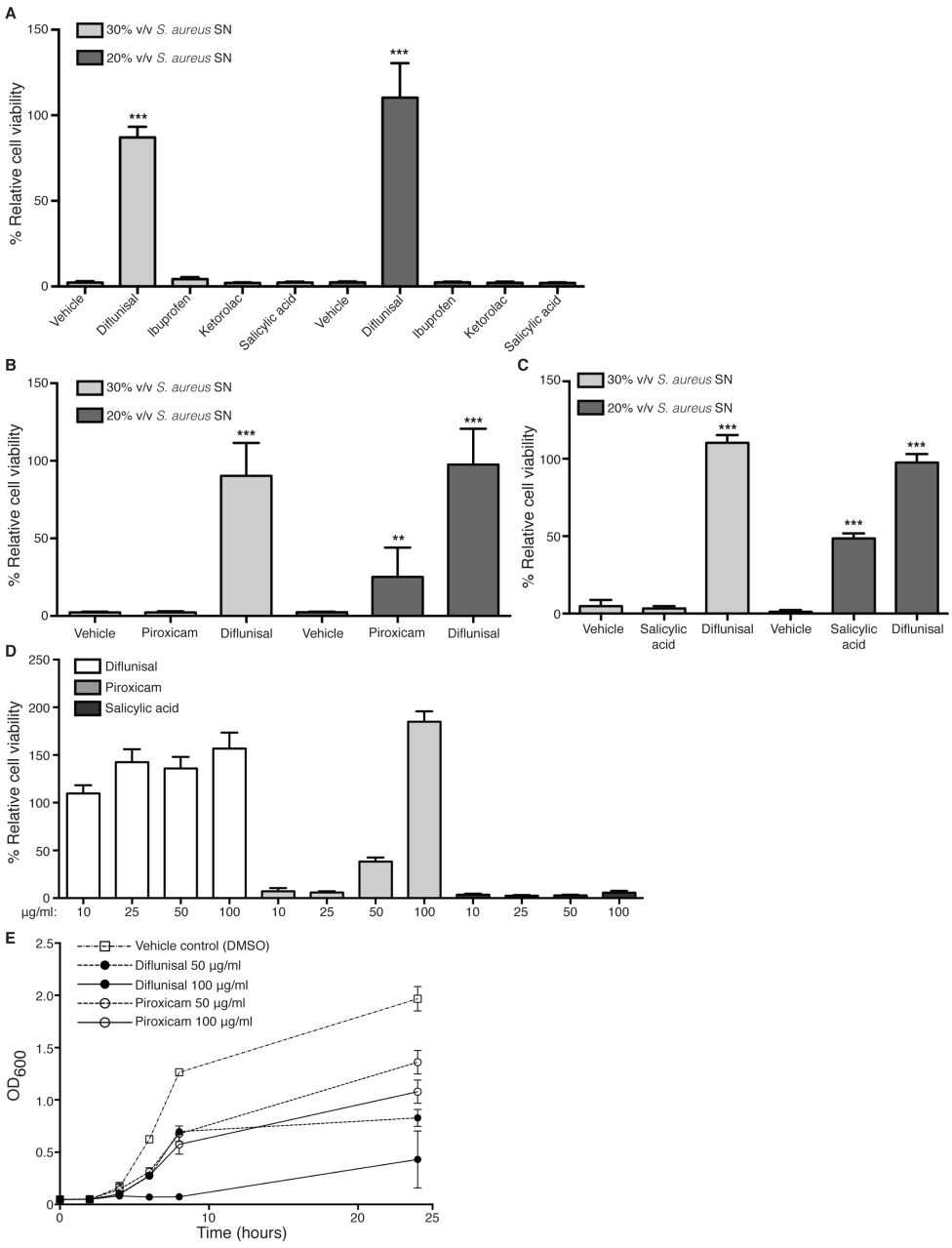

Figure 4.1.3. **Potent inhibition of *S. aureus* cytotoxicity towards osteoblasts is unique to diflunisal.** (A) MC3T3 cells were intoxicated with 20% or 30% v/v of concentrated SN from *S. aureus* grown in the presence of vehicle control (ethanol) or 10 µg/ml of the indicated NSAIDs. (B) Same as (A) except that *S. aureus was* grown in the presence of vehicle control (DMSO) or 10 µg/ml of piroxicam or diflunisal, as piroxicam was not soluble in ethanol. (C) Same as (A) except that *S. aureus was* grown in the presence of vehicle control (ethanol), 10 µg/ml diflunisal, or 50 µg/ml salicylic acid. For (A-C), percent cell viability is depicted relative to mock intoxication with sterile RPMI. Error bars represent SD. N=10 per group and data are representative of two independent trials. *** denotes $p<0.001$ and ** denotes $p<0.01$ relative to vehicle control. D) Dose-response curves were performed with concentrated SNs grown in the presence of increasing amounts of diflunisal, piroxicam, and salicylic acid (in DMSO). 30% v/v concentrated SNs were then used to intoxicate MC3T3 monolayers. Percent cell viability relative to mock intoxication with sterile RPMI containing equivalent concentrations of each NSAID. N=10 per group. Error bars represent SD. E) Growth analysis (Optical density at 600nm = OD_{600}) of *S. aureus* cultured in glass Erlenmeyer flasks with a 1:5 volume to flask ratio, and in the presence of the indicated concentrations of diflunisal, piroxicam, or vehicle control (DMSO). Error bars represent SD. N=3 per group and the data represent the average of two independent trials.

avoiding the potential untoward effects of NSAIDs on the gastrointestinal, renal, and cardiovascular systems. PUR drug delivery foams were therefore fabricated to deliver diflunisal directly to the infectious focus. To test the feasibility of PUR as a drug delivery system in the murine model of *S. aureus* osteomyelitis, we first synthesized foams containing 8% wt / wt of vancomycin. Groups of mice were subjected to experimental *S. aureus* osteomyelitis, and either an empty foam or vancomycin-loaded foam was sutured into place around the affected femur, centered on the inoculation site, at the time of wound closure. Mice received no additional antibiotic therapy throughout the experiment. At 14 days post-infection, mice were euthanized and the infected femur was harvested and processed for CFU enumeration. Local vancomycin therapy dramatically reduced the bacterial burdens in affected femurs relative to mock-treated animals (**Fig. 4.1.4**). In fact, 4 of 5 vancomycin-treated animals had bacterial burdens that were below the limit of detection, suggesting that these mice may have cleared the infection completely. Therefore, PUR drug delivery foams have therapeutic efficacy in a murine model of *S. aureus* osteomyelitis.

Local diflunisal therapy significantly decreases S. aureus-induced bone destruction during osteomyelitis

Having established the feasibility of local drug delivery in a murine model of osteomyelitis, we next sought to determine if local diflunisal therapy could limit bone destruction during *S. aureus* infection. PUR foams were synthesized with a final concentration of approximately 10 mM diflunisal. To assure that the diflunisal-loaded foams would elute the drug at a sufficient concentration to inhibit skeletal cell death without impacting bacterial growth, the foams were first tested *in vitro* for the ability to block staphylococcal osteoblast cytotoxicity. Cultures grown in the

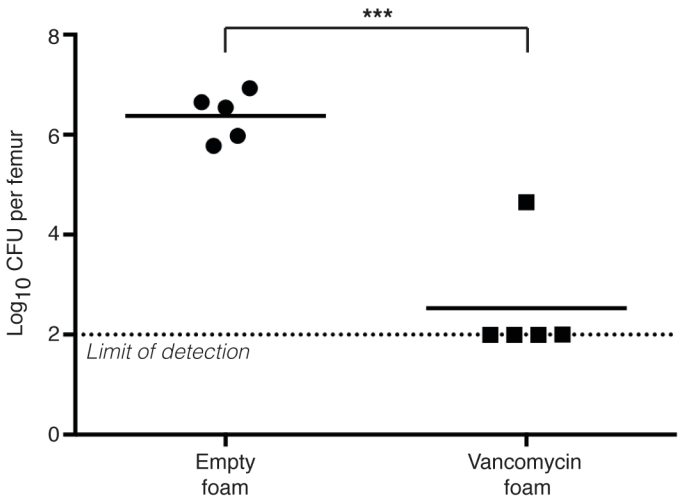

Figure 4.1.4. PUR drug delivery foams are effective as local therapies for experimental osteomyelitis. Groups (n=5) of 7-8 week female C57BL/6J mice were subjected to experimental osteomyelitis by inoculation with S. aureus. Following inoculation, either an empty PUR foam, or a foam containing 8% weight / weight vancomycin was sutured into place around the inoculation site. At 14 days post-inoculation, femurs were harvested and processed for CFU enumeration. Log_{10} CFU per femur is depicted. Horizontal bar represents the mean. Dotted line depicts the limit of detection for bacterial burdens. *** denotes $p<0.001$ relative to mice administered an empty foam.

presence of diflunisal-loaded foams achieved similar bacterial densities when compared to cultures incubated with empty foams (9.93 ± 0.1008 $\log_{10}$ CFU/ml for diflunisal treatment versus 9.81 ± 0.1307 $\log_{10}$ CFU/ml for mock; n=3). However, supernatants prepared from cultures incubated in the presence of diflunisal-loaded foams had substantially less cytotoxicity towards osteoblastic cells in comparison to cultures incubated with empty foams (**Fig. 4.1.5A**). Of note, the potency of concentrated *S. aureus* supernatant was lower in the presence of empty foams relative to experiments with other vehicle controls, which may reflect non-specific binding or inhibition of the amphipathic phenol soluble modulins by the foams. Nevertheless, diflunisal-loaded foams still showed significant inhibition of cytotoxicity relative to empty foams. Additionally, the *in vitro* release kinetics of diflunisal indicated an initial burst release from the foam in the first 24-48 hrs, with approximately 50% of the loaded diflunisal having released within the first day followed by a sustained release until day 7 (**Supp. Fig. 4.1.3**). From these results we concluded that diflunisal-loaded PUR foams elute the drug within the range of therapeutic efficacy.

To test the ability of diflunisal to inhibit pathogen-induced bone destruction, groups of mice were subjected to staphylococcal osteomyelitis and administered a diflunisal-loaded or empty foam. At 14 days post-infection, infected femurs were removed and either imaged by μCT or processed for CFU enumeration. There were no significant differences in bacterial burdens in the femurs of mice receiving local diflunisal therapy versus those receiving mock treatment (**Figure 4.1.5B**). However, mice treated with diflunisal experienced significantly less cortical bone destruction than mock-treated mice, with an average reduction in bone destruction of 36% in two independent trials (**Fig. 4.1.5C-D**). In sum, these data show that diflunisal therapy ameliorates the pathogenesis of staphylococcal osteomyelitis by blocking osteoblast cell cytotoxicity and limiting cortical bone destruction. We therefore propose that diflunisal could be a promising adjunctive therapy for invasive staphylococcal disease, and particularly musculoskeletal infections.

Discussion

Invasive *S. aureus* infections are a considerable source of global morbidity and mortality. Treatment of staphylococcal infections is hindered by intrinsic antimicrobial resistance, as well as by extrinsic factors that lessen the clinical efficacy of antimicrobial agents with proven activity *in vitro*. Staphylococcal osteomyelitis is perhaps most demonstrative of these barriers to treatment, as many musculoskeletal infections in the United States are caused by antibiotic-resistant *S. aureus* (3), and pathogen-induced bone destruction limits antimicrobial penetration to the infectious focus. Osteomyelitis therefore requires prolonged antibiotic therapy and invasive debridement procedures, after which a proportion of patients still progress to chronic infection.

Given that *S. aureus* accounts for nearly half of all deaths caused by antibiotic-resistant pathogens in the United States, there is an urgent focus on the development of new antimicrobial therapies. This includes new and improved antibiotics for treatment of resistant pathogens, as well

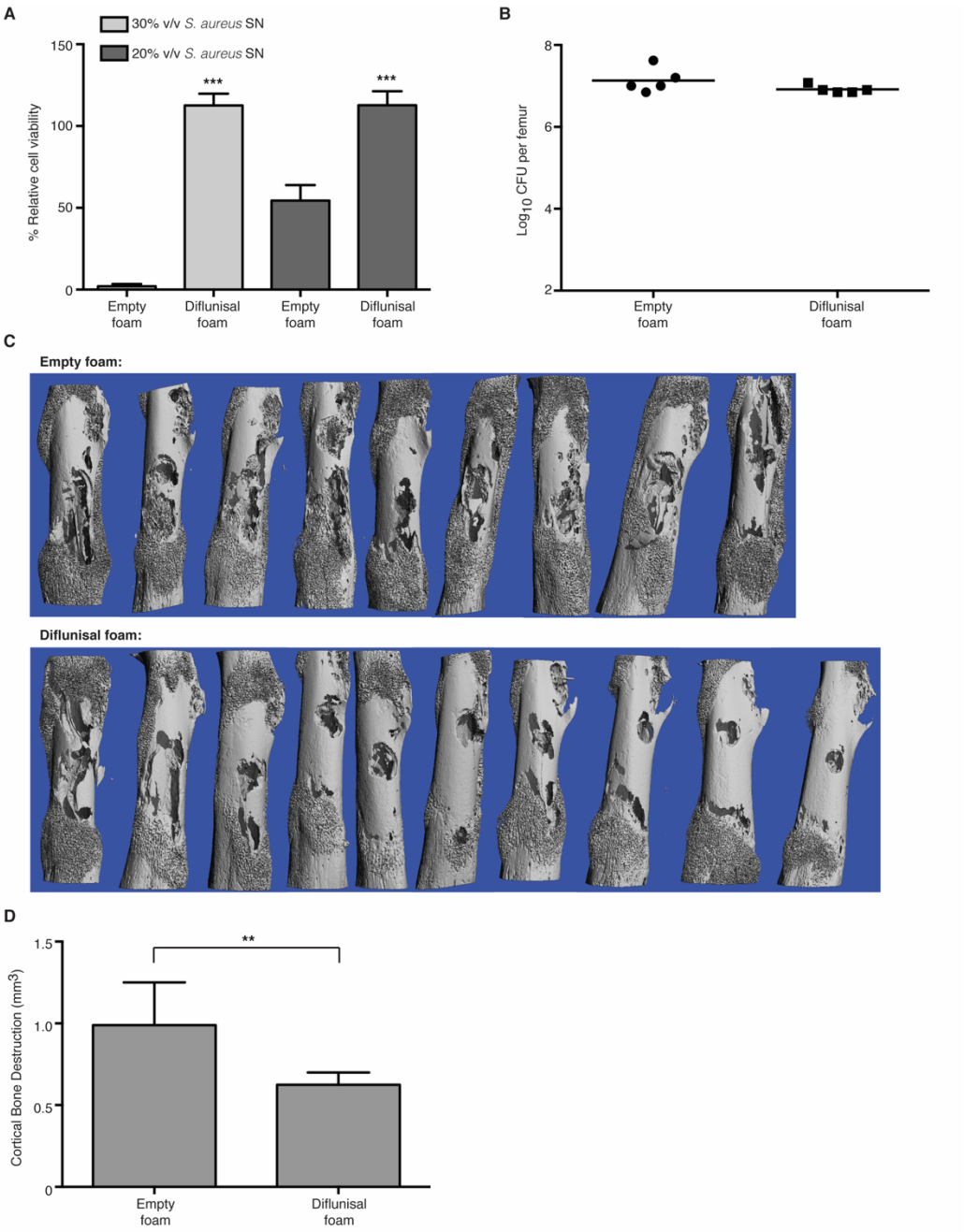

Figure 4.1.5. Local diflunisal therapy significantly decreases *S. aureus*-induced bone destruction during osteomyelitis. (A) MC3T3 cells were intoxicated with 20% or 30% v/v concentrated *S. aureus* supernatant prepared from cultures grown in the presence of either an empty PUR foam or a foam containing 10mM diflunisal. N=10 per group and data are representative of three independent trials. Error bars represent SD. Percent cell viability is depicted relative to mock intoxication with sterile RPMI. *** denotes $p<0.001$ relative to empty foam treatment. (B-D) Groups of 7-8 week female C57BL/6J mice were subjected to experimental osteomyelitis by inoculation with *S. aureus*. Following inoculation, either an empty PUR foam, or a foam containing 10 mM diflunisal was sutured into place around the inoculation site. At 14 days post-inoculation, femurs were harvested and either processed for CFU enumeration (B) or µCT analysis (C and D). For CFU enumeration, n=5 per group and $\log_{10}$ CFU per femur is depicted. Horizontal bar represents the mean. Dotted line depicts the limit of detection for bacterial burdens. For µCT analysis, n=9 or 10 per group (one mouse in the control group suffered a pathologic fracture), and data are the average of two independent trials. (C) Anteroposterior µCT images of femurs subjected to either mock treatment (empty foam) or local diflunisal therapy. (D) Quantification of cortical bone destruction. Error bar represents SD. ** denotes $p<0.01$.

as complementary therapies aimed at boosting host immune responses or limiting the extrinsic factors that promote treatment failure. In regards to staphylococcal osteomyelitis, therapies that limit pathologic bone destruction and improve antibiotic delivery to the infectious focus could significantly enhance traditional antimicrobial therapy. Such complementary therapies could shorten the duration of therapy for osteomyelitis while also limiting progression to chronic infection, thereby lessening the likelihood of a pathogen developing intrinsic antimicrobial resistance. In this study, we tested the FDA-approved NSAID diflunisal as a potential complementary therapy for *S. aureus* osteomyelitis. Diflunisal potently inhibited staphylococcal cytotoxicity toward murine and human osteoblasts *in vitro*, and significantly reduced bone destruction during experimental osteomyelitis. Because the *agr* system is necessary for expression of critical virulence factors by *S. aureus*, blockade of AgrA activity by diflunisal may also have therapeutic efficacy in other invasive staphylococcal diseases. Our *in vivo* studies likely underestimate the efficacy of diflunisal as an osteoprotective agent, as the release kinetics of diflunisal-loaded foams indicated the majority of the compound is released in the first week of the two week experiment. In future studies, we will tune the foams to deliver the most efficacious release pattern *in vivo*.

Since surgical debridement of infected bone is a standard practice in the treatment of acute osteomyelitis, a unique opportunity exists for administration of local therapies. In order to create a preclinical model to evaluate local therapies for staphylococcal infection, we utilized drug-eluting PUR foams in a murine model of osteomyelitis. PUR foams effectively delivered both vancomycin and diflunisal to the infectious focus, resulting in efficient bacterial killing and amelioration of bone destruction, respectively. Since PUR foams can be synthesized in a variety of shapes and sizes, are readily compressible, and can be loaded with a variety of antimicrobial

and tissue regenerative compounds, they may be particularly useful for the delivery of local therapies to infected tissues (22). The murine model of osteomyelitis did not allow for testing the efficacy of diflunisal in limiting the pathogenesis of established infections, as this would require stabilization of the induced fracture with a fixator device to facilitate multiple surgical procedures. Instead, we are currently developing alternative delivery vehicles for diflunisal to facilitate percutaneous administration to the infectious focus.

Future studies will determine if local diflunisal therapy enhances systemic antimicrobial therapy, in terms of reducing the necessary duration of therapy, limiting the outgrowth of resistant pathogens, or by decreasing the progression to chronic infection. One limitation of the current study is the inability to parse out the anti-virulence effects of diflunisal from its anti-inflammatory properties. NSAIDs are known to affect bone remodeling, and specifically impact osteoclast biology via inhibition of the synthesis of pro-resorptive, inflammatory mediators such as prostaglandins (23). Additional studies are required to further investigate the cellular mechanisms underlying the osteoprotective effects of diflunisal in the context of osteomyelitis, and whether osteoprotection is mediated by osteoblasts, osteoclasts, or both. Nevertheless, as NSAIDs are a mainstay of therapy for patients recovering from osteomyelitis, any anti-virulence effects that can be added by diflunisal will be valuable. Another potential limitation of diflunisal therapy is that AgrA inhibition may have the unintended consequence of increasing biofilm formation. Inactivation of the *agr* system leads to enhanced *in vitro* biofilm formation in a number of *S. aureus* strains, and Agr-defective strains have been isolated from patients with chronic musculoskeletal infection (24-27). It may therefore be prudent to only use diflunisal in combination with traditional antibiotics, and perhaps to focus on patients with acute osteomyelitis, rather than those with implant-associated infection or established chronic disease. Despite these caveats, our work

suggests that diflunisal may be a promising adjunctive therapy for osteomyelitis with anti-virulence and osteoprotective effects.

Supplementary Figures:

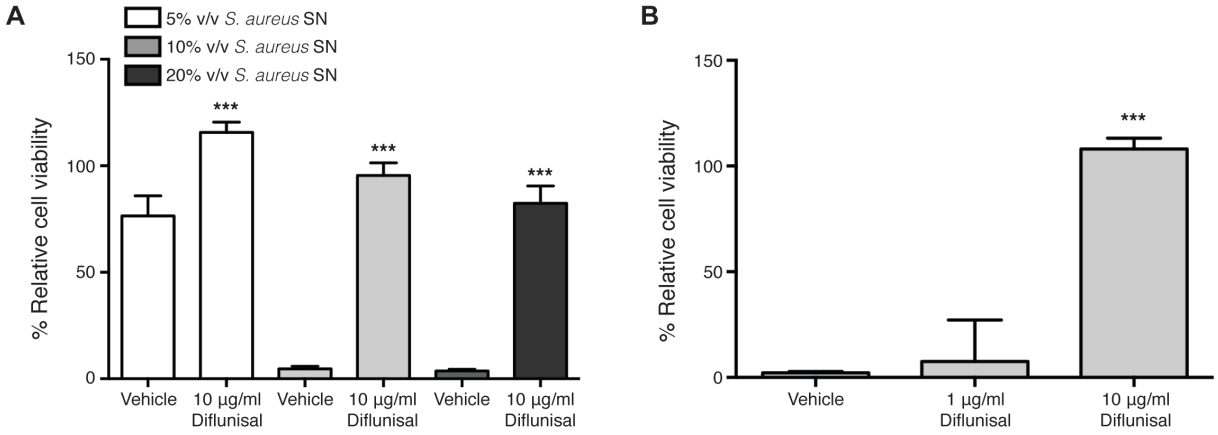

Supplementary Figure 0.1. Diflunisal maintains efficacy in cultures with decreased oxygenation. (**A**) To test the efficacy of diflunisal in limiting non-USA300 strains of *S.* aureus, concentrated supernatants from strain Newman were prepared in the presence or absence of 10 µg/ml diflunisal or vehicle control (DMSO). Percent cell viability is depicted relative to mock intoxication with sterile RPMI. Error bars represent SD. N=10 per group and data are representative of two independent trials. *** denotes $p<0.001$ relative to vehicle control. (**B**) To test the efficacy of diflunisal under hypoxic culture conditions that increase the cytotoxic potential of *S. aureus*, bacteria were grown in tightly-capped glass Erlenmeyer flasks with a 1:5 volume to flask ratio. MC3T3 murine osteoblastic cells were intoxicated with 30% volume/volume (v/v) of concentrated supernatant (SN) from *S. aureus* grown as above in the presence of vehicle control (ethanol) or the indicated concentrations of diflunisal. Percent cell viability is depicted relative to mock intoxication with sterile ROMI. Error bars represent SD. N=10 per group and data are representative of two independent trials. *** denotes $p<0.001$ relative to vehicle control.

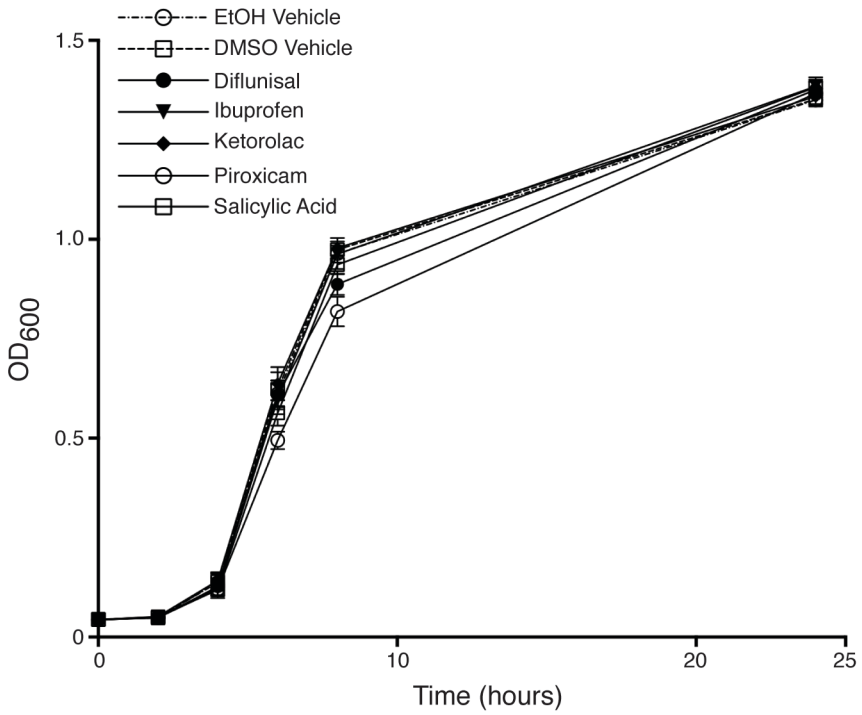

Supplementary Figure 0.2. Growth analysis of S. aureus cultured in the presence of select 19 NSAIDs. Growth analysis (Optical density at 600nm = OD600) of S. aureus cultured in glass Erlenmeyer flasks with 1:5 volume to flask ratio, and in the presence of two different vehicle controls (100% ethanol or DMSO) or 10 µg/ml of the indicated NSAIDs. Piroxicam and Ketorolac were dissolved in DMSO, all other compounds were dissolved in ethanol. Error bars represent SD. The average of 3 independent trials is depicted.

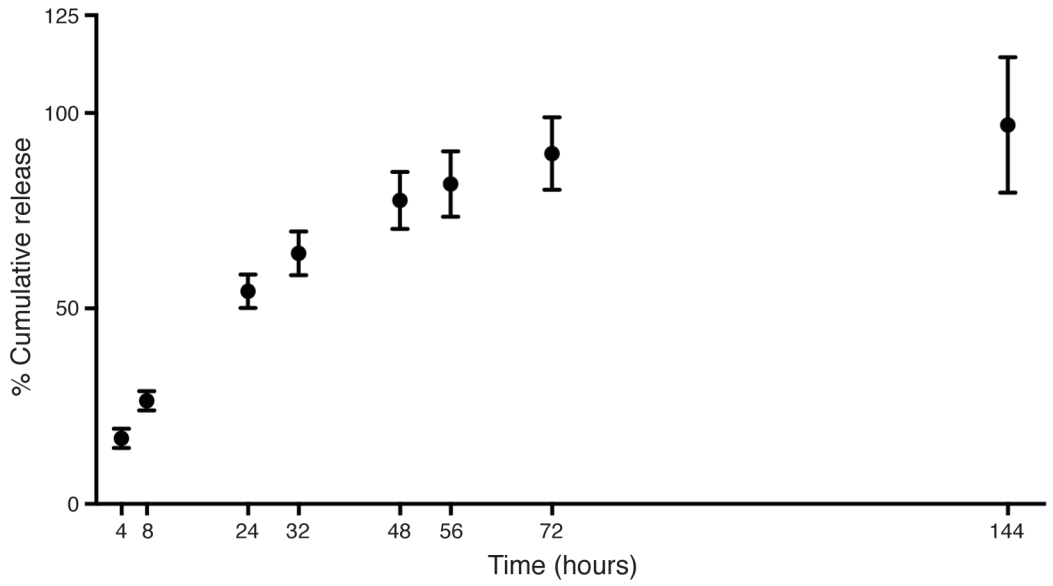

Supplementary Figure 0.3. Release kinetics of diflunisal-loaded foams. PUR foams containing 10 mM diflunisal were incubated in 50 ml of PBS at 37°C on a mixer. Samples were withdrawn for analysis at 4, 8, 24, 32, 48, 56, 72, and 144 hrs post-incubation. The amount of diflunisal in each eluate was determined by HPLC. Error bars represent SD. N=4 for each timepoint.

Concurrent local delivery of diflunisal limits bone destruction but fails to improve systemic vancomycin efficacy during *Staphylococcus aureus* osteomyelitis

Adapted from:

Spoonmore, TJ, Ford, CA, Curry, JM, Guelcher, SA, Cassat, JE. "Concurrent local delivery of diflunisal limits bone destruction but fails to improve systemic vancomycin efficacy during *Staphylococcus aureus* osteomyelitis." *Antimicrobial Agents Chemotherapy*. Accepted 22 April, 2020.

Abstract

The nonsteroidal anti-inflammatory drug diflunisal was previously identified as an osteoprotective adjunctive therapy for osteomyelitis, based on the ability of this compound to inhibit *S. aureus* quorum sensing and subsequent quorum-dependent toxin production. When delivered locally during experimental osteomyelitis, diflunisal significantly limits bone destruction without affecting bacterial burdens. However, because diflunisal's "quorum-quenching" activity could theoretically increase antibiotic recalcitrance, it is critically important to evaluate this adjunctive therapy in the context of standard of care antibiotics. The objective of this study is to evaluate the efficacy of vancomycin to treat osteomyelitis during local diflunisal treatment. We first determined that systemic vancomycin effectively reduces bacterial burdens in a murine model of osteomyelitis, and identified a dosing regimen that decreases bacterial burdens without eradicating infection. Using this dosing scheme, we found that vancomycin activity is unaffected by the presence of diflunisal *in vitro* and *in vivo*. Similarly, locally-delivered diflunisal still potently inhibits osteoblast cytotoxicity *in vitro* and bone destruction *in vivo* in the presence of sub-therapeutic vancomycin. However, we also found that the resorbable polyurethane foams used to deliver diflunisal serve as a nidus for infection. Taken together, these data demonstrate that diflunisal does not significantly impact standard of care antibiotic therapy for *S. aureus* osteomyelitis, but also highlight potential pitfalls encountered with local drug delivery.

Introduction

We recently used a murine model of staphylococcal osteomyelitis to confirm the seminal findings of Gillaspy et al, who discovered a key role for the *S. aureus* quorum sensing accessory gene regulator (*agr*) locus in mediating bone destruction during experimental osteomyelitis in rabbits (5, 28). Based on these findings, we then tested the efficacy of local delivery of the nonsteroidal anti-inflammatory drug (NSAID) diflunisal in the murine osteomyelitis model (29). Diflunisal is a salicylic acid derivative that was identified in an *in silico* screen for compounds that might inhibit histidine kinase (AgrC)-mediated phosphorylation of the response regulator AgrA, and was found to mitigate virulence factor production without having an effect on bacterial growth (11). Consistent with these findings, we found that diflunisal potently inhibited Agr-mediated cytotoxicity toward osteoblasts (29). Moreover, local delivery of diflunisal *in vivo* in a murine model of *S. aureus* osteomyelitis decreased cortical bone destruction independently of changes in bacterial burden. Collectively, these findings outlined the feasibility of diflunisal as an adjunctive therapy for staphylococcal osteomyelitis, which adds to a growing body of literature suggesting that so-called "quorum quenching" might be an effective strategy to limit staphylococcal virulence during invasive infection (30-34).

Although quorum-quenching approaches have shown great pre-clinical promise for the treatment of staphylococcal disease, functional suppression of the Agr pathway could also have detrimental effects on antimicrobial therapy for *S. aureus*. Inactivation of the *agr* locus leads to enhanced biofilm formation *in vitro*, which could conceivably limit antibiotic diffusion into the infectious niche (24, 35, 36). Moreover, clinical isolates obtained from patients suffering from chronic, invasive staphylococcal infections, including osteomyelitis, frequently have inactivating mutations in the *agr* locus (37-40). Thus, functional suppression of Agr-mediated gene regulation

may represent an adaptation to host tissues during chronic infection. These observations suggest that quorum-quenching agents could potentially exacerbate staphylococcal disease, and therefore these compounds should be evaluated in the context of standard-of-care antibiotic therapy.

The objective of this study was to evaluate the efficacy of the quorum-quenching drug diflunisal in the context of systemic antibiotic therapy during *S. aureus* osteomyelitis. We hypothesized that adjunctive diflunisal therapy would inhibit *S. aureus*-mediated bone destruction and would not interfere with systemic antibiotic activity at the infectious focus. However, we also entertained the hypothesis that diflunisal would decrease antibiotic efficacy, resulting in an infection that is more recalcitrant to standard-of-care antibiotic therapy. To test these hypotheses, we evaluated vancomycin treatment of *S. aureus* in the presence and absence of diflunisal, both *in vitro* and *in vivo*.

Materials and Methods

Bacterial strains, reagents, and growth conditions

An erythromycin-sensitive derivative of the methicillin-resistant *S. aureus* (MRSA) USA300-lineage strain LAC was used for all experiments, as it represents the most commonly isolated clonal complex causing musculoskeletal infection in the United States (12, 41). Overnight cultures were grown in Tryptic Soy Broth (TSB) at 37°C and 180 RPM shaking. Optical density at 600 nm (OD_{600}) was measured to determine bacterial growth prior to infection. Diflunisal was purchased from Sigma-Aldrich (St. Louis, MO) and dissolved in 100% DMSO at a final concentration of 10 mg/ml. Lysine triisocyanate (LTI) was purchased from Jinan Haohua Industry Co., Ltd (Jinan, China) and refluxed with a dispersion of activated carbon (Fisher Scientific) in *t*-butyl methyl ether (TBME, Across-Organic) at 60C for 22 h to remove high-molecular weight impurities (42). For

polyester triol synthesis, ε-caprolactone and stannous octoate were purchased from Sigma-Aldrich, and $_{D,L}$-lactide and glycolide were purchased from Polysciences (Warrington, PA). Triethylene diamine (TEDA) catalyst was received from Goldschmidt (TEGOAMIN33, Hopewell, VA). All other reagents including calcium stearate and turkey red oil were purchased from Sigma-Aldrich. Vancomycin-HCl was purchased from GoldBio (St. Louis, MO).

Synthesis of poly(ester urethane) (PUR) foams for local drug delivery

PUR foams were synthesized as previously reported (29). Briefly, a polyester triol (polyol) was synthesized containing 70% ε-caprolactone, 20% glycolide, and 10% lactide (M_n = 900 g mol^{-1}). The polyester triol and LTI were reacted to form a settable PUR foam. Polymer components were mixed in a 5 ml plastic container for 1.5 minutes using a Hauschild SpeedMixer DAC 150FVZ-K vortex mixer (Flacktek) and left overnight to cure. Blank foams and foams loaded with 10 mM (1.3wt%) or 20 mM (2.6wt%) diflunisal (based on foam volume) were tested. Foams were cut into prisms (8 mm × 4.5 mm × 2 mm) for *in vivo* testing and sterilized by γ-irradiation (25 kGy). Foams were imaged by SEM to characterize pore size and porosity using ImageJ.

In vitro release kinetics of diflunisal PUR foams

Specimens for *in vitro* testing were cut to match the size of those tested *in vivo*. Foams containing 20 mM diflunisal were submerged in 8 ml of PBS in a glass vial and incubated at 37°C with slight agitation. 4 ml of leachate was removed on days 1, 2, 3, 5, 11, and 14 and replaced with 4 ml of fresh PBS. We previously evaluated the release of diflunisal from PUR by HPLC (29). We previously analyzed the cumulative diflunisal release relative to the total amount released from the foam by day 14. In the current study, we instead evaluated diflunisal release by the amount of

diflunisal released as a fraction of the theoretical mass loaded in each foam. Diflunisal concentration was quantified using a UV/vis plate reader with a fluorescence reading at 420 nm and excitation of 310 nm (43). Release of diflunisal was characterized by the cumulative release percentage of diflunisal compared to the total loading in each foam sample.

Bacterial viability assay

Bacterial viability following exposure to varying concentrations of vancomycin and diflunisal was assessed in non-tissue cultured treated 24 well plates. *S. aureus* was cultured overnight and diluted to an initial inoculum of 10^5 colony forming units (CFUs)/cm^2. Diflunisal and vancomycin were solubilized by DMSO and diluted in TSB. Bacteria were exposed to varying concentrations of diflunisal and/or vancomycin for 24 hours at 37°C while agitated at 80 RPM. Adherent bacteria were then washed with sterile PBS and separated from the plate surface using a sonicator bath. Sonicated samples were serially diluted and plated on TSA plates for CFU enumeration per surface area of well plate.

Preparation of concentrated supernatants

Concentrated supernatants were prepared as previously reported (29). Briefly, 3 colonies were inoculated into triplicate 50-ml cultures in capped 250-ml Erlenmeyer flasks and grown for 15 hours in RPMI + 1% casamino acids together with PUR foams containing 0, 10, 20 mM diflunisal, 10 μg/ml diflunisal, or 10 μg/ml diflunisal + 0.1 μg/ml vancomycin. DMSO was used as a vehicle control for solubilized diflunisal and vancomycin delivery. Bacteria were grown at 37°C for 15 hours and 180 RPM, after which a sample was taken for CFU enumeration and supernatants were separated by centrifugation. Supernatants were sterilized by passage through a 0.22-μm filter, and

then concentrated to a final volume of ~1.5 ml using an Amicon Ultra 3 kDa nominal molecular weight column. Supernatants were again filter sterilized and frozen at -80°C.

Osteoblast cytotoxicity assay

Osteoblast cytotoxicity was assessed using MC3T3-E1 murine osteoblast cells as previously reported (29). Briefly, cells were seeded in 96 well tissue culture treated plates and grown at 37°C and 5% CO_2. Cells were intoxicated with prepared supernatants 12-24 hours after seeding and then incubated for 22 hours, at which time cell viability was determined using CellTiter Aqueous One solution (Promega, Madison, WI) according to manufacturer's instructions.

Murine model of osteomyelitis and systemic vancomycin treatment

This study was approved by the Institutional Animal Care and Use Committee of Vanderbilt University Medical Center and conducted in compliance with Animal Welfare Regulations and the principles of the Guide for the Care and Use of Laboratory Animals. Osteomyelitis was induced in 7-8 week female C57BL/6J mice as previously described (5). An inoculum of ~1×10^6 colony-forming units (CFU) in 2 µl phosphate-buffered saline (PBS) was delivered into murine femurs. To determine a systemic vancomycin dose that does not result in complete eradication of infection, mice (n=5) were subcutaneously injected with 50 µl of 0, 10, 20, or 30 mg/kg vancomycin in sterile PBS every 12 hours. Mice were euthanized 7 days post-infection, and the infected femur was removed and processed for CFU enumeration. Femurs were homogenized in a Bullet Blender® (Next Advance, Averill, NY) using the Navy Bead Lysis Kit and plated at limiting dilution on Tryptic Soy Agar (TSA). Results are reported as $\log_{10}$(CFUs/femur).

Combined systemic vancomycin and local diflunisal treatment in a murine model of osteomyelitis

Osteomyelitis was induced in 7-8 week female C57BL/6J mice as described above (5). 10 mg/kg of vancomycin was injected subcutaneously (SQ) every 12 hours. Sterile PBS was injected as a vehicle control. PUR foams (8 mm × 4.5 mm × 2 mm) containing 20 mM diflunisal were fabricated, sterilized, and wrapped around the femur at the inoculation site and sutured into place. Empty PUR foams served as a mock control. Groups are identified in **Table 1**. Mice that experienced >20% weight loss following infection were euthanized. For evaluation of bacterial burdens, mice were euthanized at 7 days post-infection, and the infected femur was removed and processed for CFU enumeration as above. To evaluate bacterial dissemination, livers, kidneys, and foams were also removed and processed for CFU enumeration. Residual PUR foam was separated from soft tissues and sonicated in an ultrasonic bath for 5 minutes prior to CFU enumeration. To evaluate cortical bone destruction, additional groups of mice were euthanized at day 14 post-infection and the infected femurs were analyzed by μCT as described previously (5). Briefly, axial images of each femur were captured with 5.0 μm voxels at 70 kV, 200 μA, 2000 projections per rotation and an integration time of 350 msec in a 10.24 mm field-of-view. Each imaging scan comprised 1635 slices (8.125 mm) of the length of the femur, centered on the inoculation site as visualized in the scout-view radiographs. Volume of interest (VOI) was limited to the original cortical bone and any destruction was selected by drawing inclusive contours on the periosteal surface, excluding contours on the endosteal surface.

Statistical evaluation

Differences in CFU counts and cortical bone destruction were analyzed by Student's *t* test. A *p*-value of ≤ 0.05 was considered significant.

Results

Porosity and drug release of diflunisal-loaded PUR foams

Scanning electron microscopy (SEM) was performed to determine the effects of diflunisal loading on porosity and pore size of PUR foams (**Fig. 4.2.1A-C**). Empty foams exhibited 89 ± 2% porosity (**Fig. 4.2.1D**) and pore diameter 190 ± 150 μm (**Fig. 4.2.1E**), consistent with previous studies (15, 44, 45). PUR foams loaded with 10 mM diflunisal demonstrated 85 ± 7% porosity and pore diameter 135 ± 130 μm , and PUR foams containing 20 mM diflunisal had 92 ± 3% porosity and pore diameter 190 ± 172 μm. To characterize diflunisal release, diflunisal-loaded PUR foams were incubated in PBS at 37°C for 14 days, and diflunisal concentration released from the foams was analyzed using a UV/vis plate reader. Diflunisal has an amphiphilic profile in water with a solubility of 14.5 mg/L and an octanol/water partition coefficient of 4.4. We therefore anticipated a slow release of diflunisal from the PUR foam (46). A bolus release of 5% (~8 μg) was observed on day 1, and ~20% of the total diflunisal in the PUR foam was released after 14 days (**Fig. 4.2.1F**).

Diflunisal does not inhibit vancomycin activity in vitro

Functional inactivation of the Agr system could theoretically decrease antibiotic efficacy through altered bacterial metabolism. We therefore investigated if quorum-quenching therapy with diflunisal inhibited the effectiveness of vancomycin *in vitro*. To investigate the effects of simultaneous delivery of vancomycin and diflunisal, both compounds were delivered in a solubilized form to a subculture of *S. aureus*. Vancomycin concentrations both above and below the MIC (1 μg/ml) were chosen for these experiments. Soluble diflunisal was delivered at 25 μg/ml, a concentration comparable to the total payload delivered by a diflunisal-loaded foam.

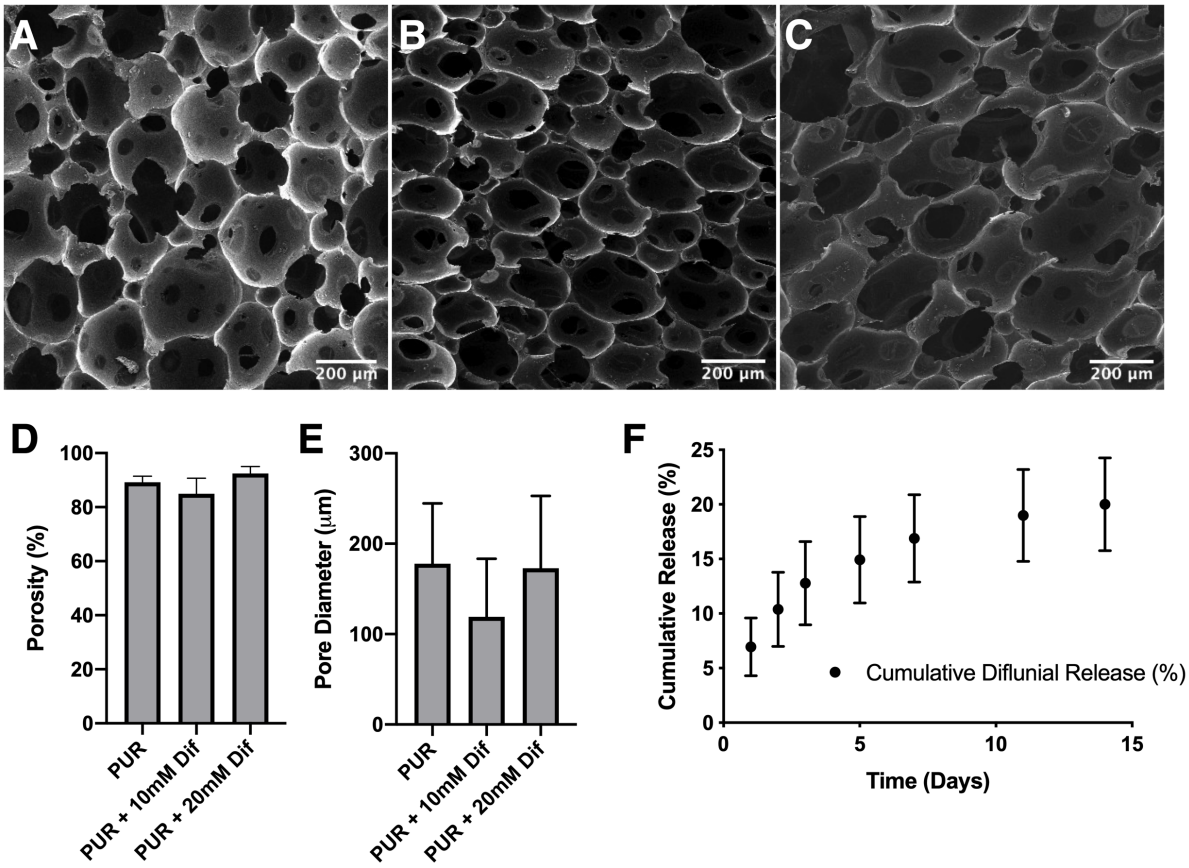

Figure 4.2.1. Characterization of PUR and diflunisal-loaded PUR. SEM images of PUR foams containing 0 (A), 10 (B), and 20 mM (C) diflunisal. Scale bar = 200 µm. SEM images of PUR foams were used to determine porosity (%) (D) and pore diameter (µm) (E). (F) Release of diflunisal from PUR. Cumulative release was quantified as the amount of diflunisal released in the leachate normalized by the original amount of diflunisal in the foams. Daily release was quantified as the amount of diflunisal in the leachate at each time point. Error bars represent SD. N=6 per group.

Enumeration of CFUs was performed 24 hours after simultaneous vancomycin and diflunisal therapy (**Fig. 4.2.2A**). To determine how pre-treatment of *S. aureus* with diflunisal might influence subsequent susceptibility to vancomycin, bacteria were cultured in the presence (25 µg/ml) or absence of diflunisal at 37°C with shaking for 15 hours. Bacteria were then subcultured into fresh media containing diflunisal at 25 µg/ml and vancomycin at concentrations above and below the MIC (**Fig. 4.2.2B**). Vancomycin remained effective in the presence of diflunisal co-treatment, both with simultaneous treatment and with pre-treatment of bacteria prior to

vancomycin. Collectively, these results indicate that diflunisal does not significantly impact the antibacterial activity of vancomycin *in vitro*.

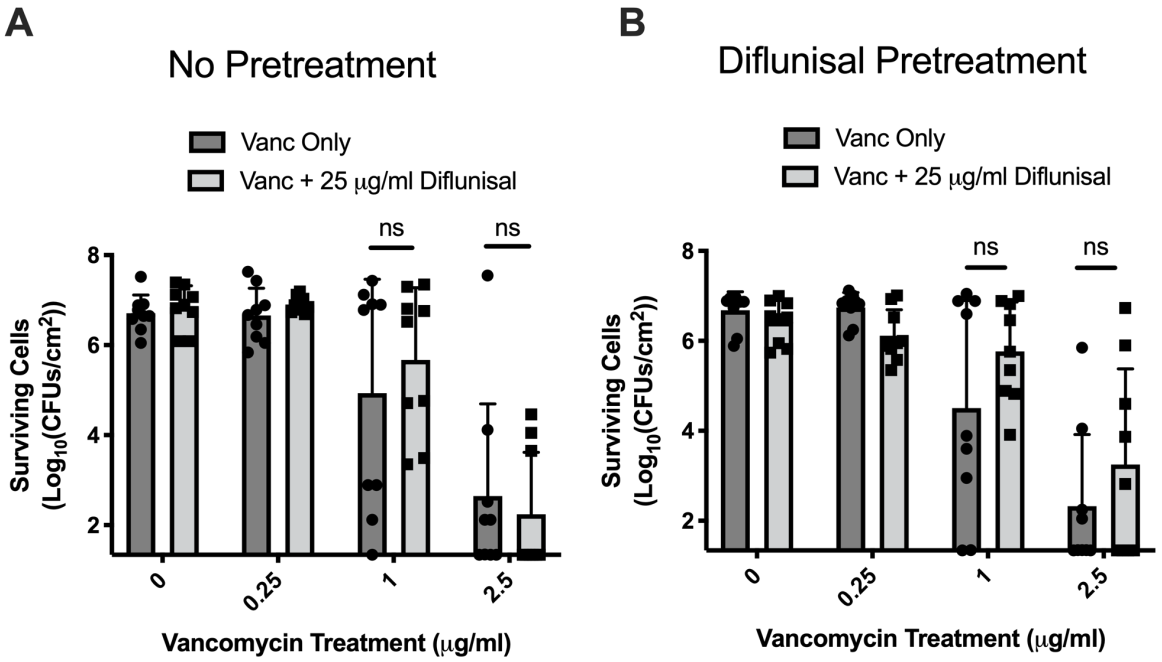

Figure 4.2.2. Diflunisal does not inhibit vancomycin activity against *S. aureus* in vitro. *S. aureus* was cultured overnight with (A) or without (B) 25 μg/ml diflunisal. Diflunisal concentration was based on the total amount of diflunisal released from the foams determined in Fig. 1. Vancomycin was delivered at concentrations near the minimum inhibitory concentration (MIC) with and without diflunisal to characterize the effect of combined delivery on the bactericidal capability of vancomycin. N=3 technical replicates per group and data are representative of 3 independent trials. Error bars represent standard deviation (SD). Significance determined by Student's *t* test.

Diflunisal released from PUR foams inhibits staphylococcal cytotoxicity in vitro

Avascular surfaces are readily colonized by bacteria at an infected site, particularly during bone grafting (22, 47). Therefore, in order to minimize the foreign body surface for bacterial colonization, PUR foam sizes were decreased compared to our previous study (29). To accommodate a smaller PUR foam and ensure a similar payload was delivered, PUR foams containing 0 mM, 10 mM (concentration of diflunisal previously tested (29)), and 20 mM (similar payload to previously tested foams) diflunisal were synthesized. *S. aureus* cultures were grown in

the presence of PUR foams containing each concentration of diflunisal, after which concentrated supernatants were prepared and tested for osteoblast cytotoxicity. Overnight cultures exhibited similar CFU concentrations suggesting diflunisal-loaded PUR did not affect bacterial growth (**Supp. Fig. 4.2.1A**). Diflunisal-loaded foams dose-dependently inhibited supernatant toxicity towards MC3T3 cells (**Supp. Fig. 4.2.1B**). Based on these results, PUR + 20 mM diflunisal foams were chosen for subsequent *in vivo* studies to minimize foam size while maintaining optimal diflunisal payload.

Vancomycin does not inhibit diflunisal activity in vitro

Diflunisal dose-dependently inhibits *S. aureus*-induced osteoblast cell death (29). Although we did not expect vancomycin to affect diflunisal activity, we prepared *S. aureus* supernatants grown in the presence of diflunisal or diflunisal + vancomycin for subsequent MC3T3 treatment. A concentration of 0.1 μg/ml vancomycin (below the vancomycin MIC) was chosen to ensure bacterial growth yields remained comparable. Overnight cultures containing vehicle control (DMSO), diflunisal, and diflunisal + vancomycin exhibited similar CFU concentrations (**Supp. Fig. 4.2.2A**). Treatment with diflunisal + vancomycin significantly limited the cytotoxicity of prepared supernatants compared to the vehicle control group (**Supp. Fig. 4.2.2B**). Furthermore, diflunisal + vancomycin treatment was not significantly different than diflunisal treatment. Thus, vancomycin did not affect diflunisal activity *in vitro*.

Subcutaneous vancomycin reduces bacterial burdens in vivo during osteomyelitis

Prior to evaluating the impact of local diflunisal therapy on antimicrobial activity of systemically administered vancomycin, we first sought to establish an effective subcutaneous dosing regimen

for vancomycin that decreased bacterial burdens without completely eradicating infection. To accomplish this, groups of mice (n=5) were intra-osseously infected with 10^6 CFUs of *S. aureus*, and vancomycin treatment was started immediately after infection via subcutaneous injection of 0, 10, 20, or 30 mg/kg every 12 hours. At 7 days post-infection, bacterial burdens were enumerated from the infected femur. Systemic vancomycin treatment at a dose of 30 mg/kg every 12 hours nearly eradicated the infection, with 2 mice exhibiting no detectable CFUs in the infected femur and the remaining three mice exhibiting bacterial burdens near the limit of detection. Decreasing the vancomycin dose resulted in a step-wise increase in bacterial burdens, with the 10 mg/kg dose resulting in an approximately 1 log reduction ($p<0.05$) in bacterial burdens (**Fig 4.2.3A**). This dose was chosen for subsequent experiments testing the impact of local diflunisal therapy. Together, these data reveal that subcutaneous vancomycin therapy is effective for control of experimental *S. aureus* osteomyelitis when given immediately following infection and identify an appropriate sub-therapeutic dose for testing additional adjunctive therapies.

Local diflunisal delivery does not improve vancomycin-mediated bacterial clearance in bone

Although we have previously demonstrated that local diflunisal treatment can decrease pathogen-induced cortical bone destruction in a murine osteomyelitis model (29), the efficacy of diflunisal in the setting of concurrent systemic antibiotic therapy is unknown. To test the impact of local diflunisal treatment on the antimicrobial efficacy of systemic vancomycin therapy, groups of mice (n=5) were subjected to experimental osteomyelitis and systemic vancomycin therapy at 10 mg/kg every 12 hours. Diflunisal was delivered locally by elution from a PUR foam (PUR-Dif) as previously reported (29). An empty PUR foam served as a control for local therapy. Bacterial burdens were determined at day 7 post-infection by homogenizing the infected femur as well as

residual PUR foam. Systemic vancomycin therapy was effective in decreasing bacterial burdens in the femurs from PUR + Vanc and PUR-Dif + Vanc mice (**Fig. 4.2.3B**). No additive effect was observed with combined vancomycin and diflunisal therapy in terms of decreasing bacterial burdens. Although systemic vancomycin therapy effectively reduced bacterial burdens in bone tissue, it failed to reduce bacterial burdens present on the surface of both PUR and PUR-Dif foams (**Fig. 4.2.3C)**, suggesting that the PUR foams are serving as a nidus of infection at the surgical site. Finally, because diflunisal inhibits Agr-mediated quorum sensing and therefore may impact dissemination of infection, we compared bacterial burdens in the kidneys and livers of infected mice. Although infection had disseminated to the kidneys and livers of some mice, no significant difference was observed between PUR + Veh and PUR-Dif + Vanc groups suggesting that the addition of diflunisal or vancomycin had no appreciable effect on bacterial dissemination from the femur (**Supp. Fig. 4.2.3**). Taken together, these data reveal that local diflunisal therapy does not impede the antimicrobial actions of systemic vancomycin therapy. However, local diflunisal delivery did not improve antibiotic killing by vancomycin under these experimental conditions. Moreover, the resorbable PUR foam, which was originally designed to function as an acellular scaffold to promote new bone formation (22), serves as an additional nidus for bacterial colonization.

Co-administration of local diflunisal treatment and systemic vancomycin therapy during osteomyelitis

To determine the effects of diflunisal therapy on *S. aureus*-mediated bone destruction in the context of systemic antibiotic therapy, we analyzed cortical bone destruction of infected femurs treated with PUR + Veh, PUR-Dif + Veh, PUR + Vanc, PUR-Dif + Vanc therapy (**Table 4.2.1**).

Vancomycin was administered subcutaneously every 12 hours at a dose of 10 mg/kg for 14 days post-infection. Diflunisal was delivered locally from a PUR foam with 20 mM diflunisal. At 14

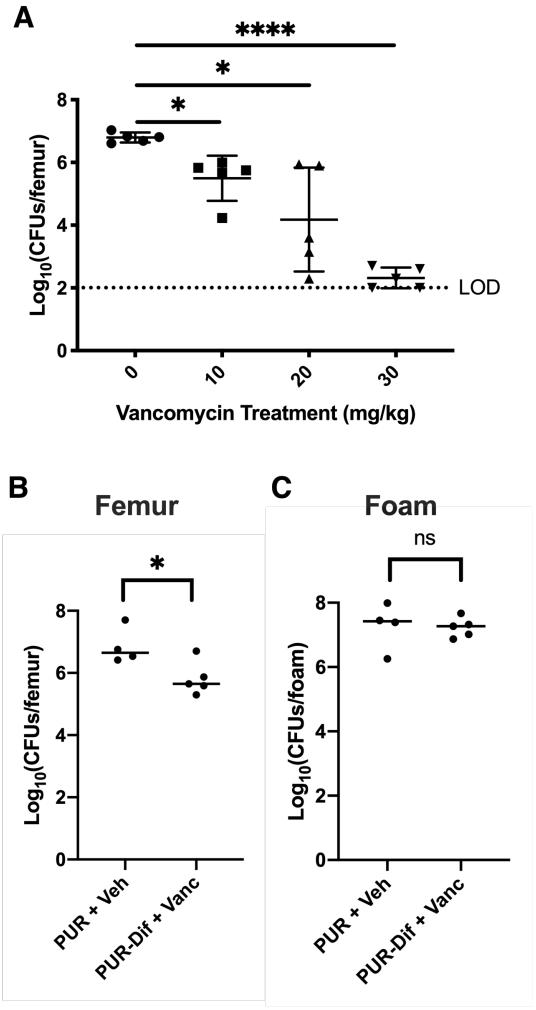

Figure 4.2.3. Local diflunisal therapy does not inhibit systemic vancomycin activity in vivo. (A) Vancomycin was delivered at 4 different concentrations to determine a sub-optimal dose that would significantly decrease the bacterial burdens in murine femurs infected with S. aureus. N=5 mice per group. Horizontal lines represent the mean. Dotted line depicts the limit of detection (LOD) for bacterial burdens. Error bars represent SD. * denotes $p<0.05$, **** denotes $p<0.0001$. (B-C) Mice were treated with either PUR + Veh or PUR-Dif (see Table 1). At 14 days post-infection, femurs (B) and foams (C) were harvested for CFU enumeration. N=4 or 5 mice per group (one mouse in the PUR+Veh group had to be euthanized according to humane endpoints). Control group demonstrates bacterial burdens consistent with separate trials (data not shown). * denotes $p<0.05$ relative to PUR + Veh treatment as determined by Student's t test.

days post-infection, infected femurs were removed and imaged by μCT. Mice treated with PUR + Veh demonstrated significant cortical bone destruction (**Fig. 4.2.4A-B**). Consistent with previous studies (29), mice treated with PUR-Dif exhibited a significant ($p<0.01$) decrease in cortical bone

destruction. Yet, both groups of mice treated with vancomycin demonstrated a significant decrease in cortical bone destruction regardless of whether local diflunisal therapy was given or not. Thus, combined therapy of diflunisal and vancomycin is capable of ameliorating the pathogenic bone destruction induced during staphylococcal osteomyelitis, but there was no additive osteo-protective benefit of local diflunisal delivery in the context of systemic antibiotic therapy.

Discussion

Treatment of osteomyelitis and other musculoskeletal infections is hindered by the relatively poor penetration of antibiotics into the infectious focus (48-51). This is in part due to the ability of *S. aureus* to induce bone destruction, which leads to devascularized and necrotic segments of bone that can serve as a niche for chronic infection (5). Osteomyelitis therefore requires prolonged antibiotic treatment in conjunction with surgical debridement to increase the chance of cure. New adjunctive therapies that decrease pathogen-induced bone destruction might improve antibiotic activity by maintaining tissue integrity and preventing complications such as pathologic fracture.

Table 0.3. Group identification of mice treated with vancomycin and diflunisal.

Group ID	Local Diflunisal dose (PUR foam)	Systemic Vancomycin Dose (SQ injection)	n
PUR + Veh	0 mM	0 mg/kg	5
PUR-Dif + Veh	20 mM	0 mg/kg	5
PUR + Vanc	0 mM	10 mg/kg	5
PUR-Dif + Vanc	20 mM	10 mg/kg	5

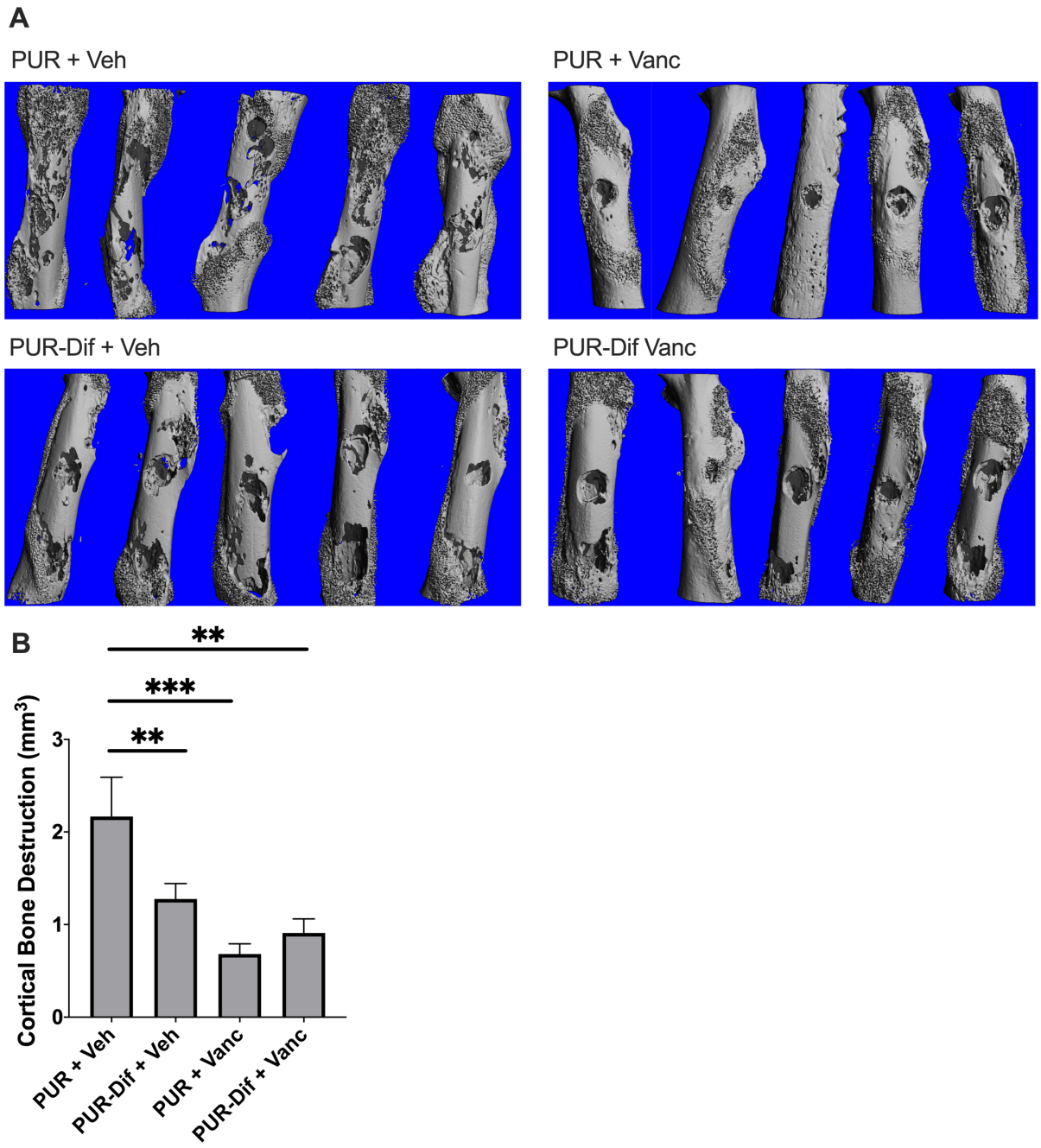

Figure 4.2.4. (A) MicroCT reconstructions of femurs treated with PUR + Veh, PUR-Dif + Veh, PUR + Vanc, or PUR-Dif + Vanc (see Table 1). N=5 mice per group. One control group mouse suffered pathologic fracture (second from left in PUR + Veh group). (B) Quantification of cortical bone destruction. Error bar represents SD. ** denotes $p<0.01$, *** denotes $p<0.001$ as determined by Student's t test.

In this study, we evaluated the efficacy of combined systemic antibiotic therapy with local delivery of the quorum-quenching compound diflunisal, which we previously demonstrated to

block *S. aureus* toxin-mediated cortical bone destruction (11, 29). We hypothesized that adjunctive diflunisal therapy would limit *S. aureus* induced bone destruction without interfering with systemic antibiotic activity at the infectious focus. However, functional blockade of the Agr quorum sensing system increases biofilm formation *in vitro*, and it was therefore conceivable that quorum-quenching therapy would decrease antibiotic efficacy *in vivo*. Reconciling this hypothesis and potential outcome in a model of invasive staphylococcal disease is important given the exciting preclinical results with several quorum-quenching therapies (30-34). We discovered that systemic vancomycin therapy dose-dependently decreases bacterial burdens in our murine model of post-traumatic osteomyelitis. Importantly, diflunisal did not significantly alter vancomycin efficacy; however, combined treatment failed to improve antimicrobial activity or further reduce cortical bone destruction. Therefore, local diflunisal therapy is likely safe in the setting of systemic antimicrobial therapy, but there are no additive benefits for bacterial eradication or prevention of bone pathology under the experimental conditions deployed in this study. Given that diflunisal and vancomycin can be delivered concurrently in this preclinical model, investigation into possible synergistic efficacy of the two compounds is necessary. Moreover, measurement of diflunisal concentration in mouse serum following local administration is an important component of the pre-clinical testing that has yet to be performed. Further research will also focus on delayed antibiotic therapy to model a more antibiotic-recalcitrant infection. Similarly, experimentation with varying doses of vancomycin, as well as other antibiotics, should be performed.

Compared to non-resorbable bone cements such as PMMA, resorbable scaffolds offer the advantage of reduced bone grafting procedures and presumably minimize the presence of foreign material that could serve as a nidus for infection (22, 47, 52-54). PUR foams augmented with recombinant human bone morphogenetic protein (rhBMP-2) have been reported to support the

regeneration of bone tissue (55, 56). While these foams degrade after 8 - 16 weeks *in vivo* (57, 58), our results suggest that even resorbable drug delivery platforms such as PUR foams can harbor significant numbers of bacteria during acute infection. Antibiotic-loaded PUR foams have been shown to decrease bacterial burdens (22, 29); however, tuning the release kinetics to deliver an effective dose for a sustained time period remains a major limitation. Dual delivery of diflunisal and antibiotic from a PUR foam has not yet been studied, yet the release of an antibiotic from the PUR surface may alleviate some of the bacterial colonization of the foreign body and effect the overall bone destruction outcome. As an alternative, bone-targeting antibiotics and nanoparticles have shown experimental promise and could be delivered systemically in patients requiring parenteral antibiotic therapy without the need for bone grafting (59, 60).

Further limitations of this study include the use of only one antibiotic, a single endpoint of 14 days, and use of a single infection model. Future studies should explore how quorum-quenching compounds might impact the activity of other anti-staphylococcal antibiotics to gain further understanding of potential synergistic combinations. Similarly, a focus on treatment timelines should be investigated to determine the effects of diflunisal therapy on antibiotic treatment duration. Diflunisal release from the PUR foams was slow (<1 wt%/day) after the initial burst release, and not all diflunisal loaded in the PUR released. It is unknown if more diflunisal released *in vivo* compared to the 20% of total loaded diflunisal released from a PUR foam *in vitro*. Although it is unclear if more diflunisal would ameliorate more bacteria-mediated bone destruction, alternative platforms that allow for repeat administrations of diflunisal should be investigated to understand the effect of higher doses on antibiotic activity at later time points. A limitation of the osteomyelitis model used in this study involved the high inoculum level required to induce infection. Although the exact bacterial load that initiates human osteomyelitis has yet to be

definitively determined and may vary significantly depending on the mechanism of disease, it is likely that many patients experience a much lower initial inoculum. Furthermore, other murine musculoskeletal infection models have shown qualitative differences in the immune responses to *S. aureus* in bone based on initial infectious burden (61). Another limitation of this study was the relatively small sample sizes used in the *in vivo* experiments, which may have limited our ability to detect more subtle clinical outcomes. A final limitation of this study is that we did not test the effect of diflunisal therapy on implant-associated osteomyelitis, where biofilm formation might play a greater role in treatment recalcitrance. Nevertheless, although the delivery of diflunisal and vancomycin can be improved, our work suggests that combined diflunisal and vancomycin treatment warrants further study as a potential adjunctive anti-virulence therapy for osteomyelitis.

Supplementary Figures:

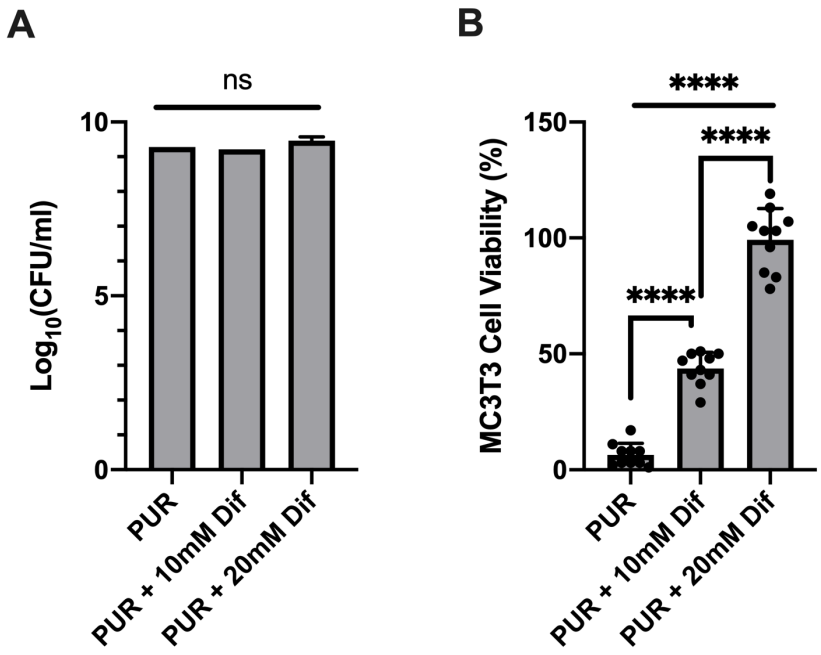

Supplementary Figure 0.4. PUR-eluted diflunisal inhibition of supernatant toxicity is dose-dependent. Concentrated supernatants were prepared by culturing bacteria in the presence of PUR containing 0, 10, or 20 mM foams. The effect of diflunisal treatment on bacterial viability was assessed by CFU enumeration (**A**) and supernatant toxicity by quantifying MC3T3 host cell viability (**B**). Error bars represent SD. Data representative of 3 independent trials. N=10 technical replicates per group. **** denotes $p<0.0001$ as determine by Student's *t* test.

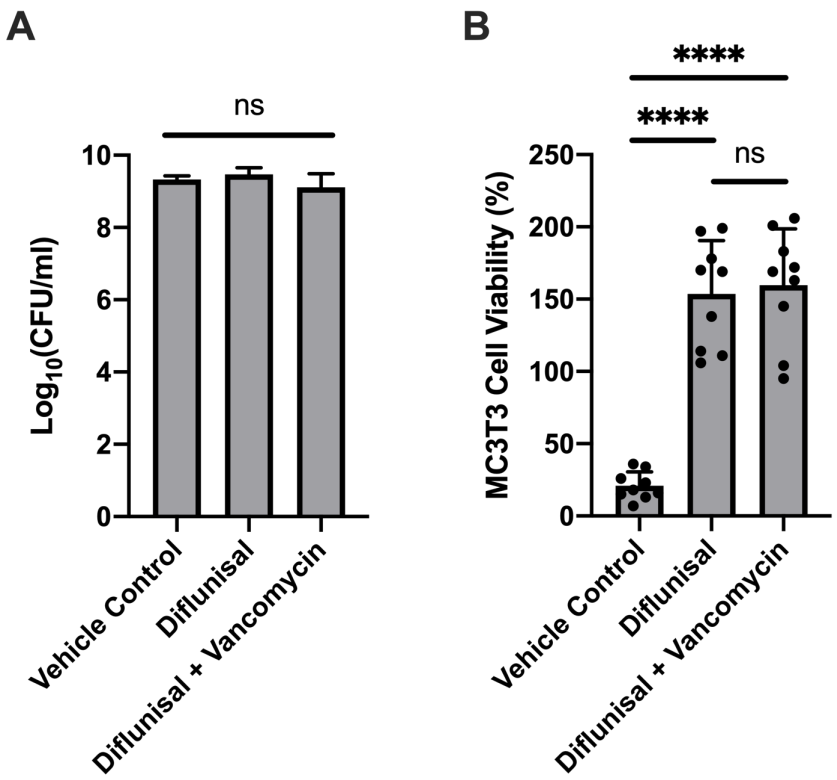

Supplementary Figure 0.5. Vancomycin does not affect diflunisal activity *in vitro*. Supernatants were prepared by culturing bacteria in the presence of either DMSO (Vehicle Control), 10 μg/ml diflunisal (Diflunisal), or 10 μg/ml diflunisal + 0.1 μg/ml vancomycin (Diflunisal + Vancomycin). The effect of diflunisal and vancomycin combined treatment on bacterial viability was assessed by CFU enumeration (**A**) and supernatant toxicity by quantifying MC3T3 host cell viability (**B**). Percent cell viability is depicted relative to mock intoxication with sterile RPMI. Error bars represent SD. N=9 technical replicates per group. Data representative of 2 independent trials. **** denotes $p<0.0001$ as assessed by Student's *t* test.

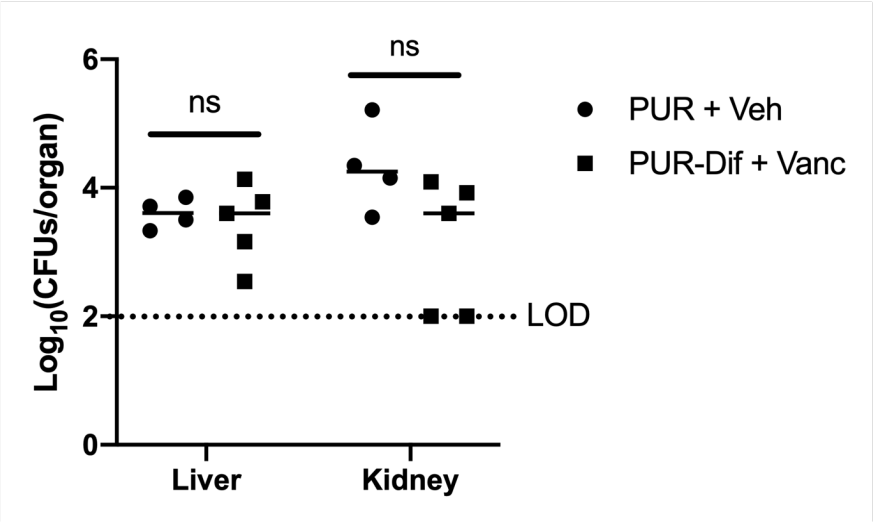

Supplementary Figure 0.6. Diflunisal does not alter bacterial dissemination from the infected femur during osteomyelitis. CFU burdens in the liver and kidneys from mice treated with either PUR + Veh or PUR-Dif + Vanc (See Table 1). N=4 or 5 mice per group (one mouse in the control group was euthanized according to humane endpoints). Dotted line depicts the limit of detection (LOD) for bacterial burdens. Statistical significance determined by Student's t test.

References

1. Lew DP, Waldvogel FA. 2004. Osteomyelitis. Lancet 364:369-79.
2. Copley LA. 2009. Pediatric musculoskeletal infection: trends and antibiotic recommendations. J Am Acad Orthop Surg 17:618-26.
3. Gerber JS, Coffin SE, Smathers SA, Zaoutis TE. 2009. Trends in the incidence of methicillin-resistant Staphylococcus aureus infection in children's hospitals in the United States. Clin Infect Dis 49:65-71.
4. Liu T, Zhang X, Li Z, Peng D. 2011. Management of combined bone defect and limb-length discrepancy after tibial chronic osteomyelitis. Orthopedics 34:e363-7.
5. Cassat JE, Hammer ND, Campbell JP, Benson MA, Perrien DS, Mrak LN, Smeltzer MS, Torres VJ, Skaar EP. 2013. A secreted bacterial protease tailors the Staphylococcus aureus virulence repertoire to modulate bone remodeling during osteomyelitis. Cell Host Microbe 13:759-72.
6. Queck SY, Jameson-Lee M, Villaruz AE, Bach TH, Khan BA, Sturdevant DE, Ricklefs SM, Li M, Otto M. 2008. RNAIII-independent target gene control by the agr quorum-sensing system: insight into the evolution of virulence regulation in Staphylococcus aureus. Mol Cell 32:150-8.
7. Sully EK, Malachowa N, Elmore BO, Alexander SM, Femling JK, Gray BM, DeLeo FR, Otto M, Cheung AL, Edwards BS, Sklar LA, Horswill AR, Hall PR, Gresham HD. 2014. Selective chemical inhibition of agr quorum sensing in Staphylococcus aureus promotes host defense with minimal impact on resistance. PLoS Pathog 10:e1004174.
8. Murray EJ, Crowley RC, Truman A, Clarke SR, Cottam JA, Jadhav GP, Steele VR, O'Shea P, Lindholm C, Cockayne A, Chhabra SR, Chan WC, Williams P. 2014. Targeting Staphylococcus aureus quorum sensing with nonpeptidic small molecule inhibitors. J Med Chem 57:2813-9.
9. George EA, Novick RP, Muir TW. 2008. Cyclic peptide inhibitors of staphylococcal virulence prepared by Fmoc-based thiolactone peptide synthesis. J Am Chem Soc 130:4914-24.
10. Nielsen A, Mansson M, Bojer MS, Gram L, Larsen TO, Novick RP, Frees D, Frokiaer H, Ingmer H. 2014. Solonamide B inhibits quorum sensing and reduces Staphylococcus aureus mediated killing of human neutrophils. PLoS One 9:e84992.
11. Khodaverdian V, Pesho M, Truitt B, Bollinger L, Patel P, Nithianantham S, Yu G, Delaney E, Jankowsky E, Shoham M. 2013. Discovery of antivirulence agents against methicillin-resistant Staphylococcus aureus. Antimicrob Agents Chemother 57:3645-52.
12. Boles BR, Thoendel M, Roth AJ, Horswill AR. 2010. Identification of genes involved in polysaccharide-independent Staphylococcus aureus biofilm formation. PLoS One 5:e10146.
13. Duthie ES, Lorenz LL. 1952. Staphylococcal coagulase; mode of action and antigenicity. J Gen Microbiol 6:95-107.
14. Wilde AD, Snyder DJ, Putnam NE, Valentino MD, Hammer ND, Lonergan ZR, Hinger SA, Aysanoa EE, Blanchard C, Dunman PM, Wasserman GA, Chen J, Shopsin B, Gilmore MS, Skaar EP, Cassat JE. 2015. Bacterial Hypoxic Responses Revealed as Critical Determinants of the Host-Pathogen Outcome by TnSeq Analysis of Staphylococcus aureus Invasive Infection. PLoS Pathog 11:e1005341.
15. Guelcher SA, Patel V, Gallagher KM, Connolly S, Didier JE, Doctor JS, Hollinger JO. 2006. Synthesis and in vitro biocompatibility of injectable polyurethane foam scaffolds. Tissue Eng 12:1247-59.
16. Sawhney AS, Hubbell JA. 1990. Rapidly degraded terpolymers of dl-lactide, glycolide, and epsilon-caprolactone with increased hydrophilicity by copolymerization with polyethers. J Biomed Mater Res 24:1397-411.
17. Wahbi AA, Mabrouk MM, Moneeb MS, Kamal AH. 2009. Simultaneous determination of the two non-steroidal anti-inflammatory drugs ; diflunisal and naproxen in their tablets by chemometric spectrophotometry and HPLC. Pak J Pharm Sci 22:8-17.
18. Hammer ND, Cassat JE, Noto MJ, Lojek LJ, Chadha AD, Schmitz JE, Creech CB, Skaar EP. 2014. Inter- and intraspecies metabolite exchange promotes virulence of antibiotic-resistant

Staphylococcus aureus. Cell Host Microbe 16:531-7.
19. Kupferwasser LI, Yeaman MR, Nast CC, Kupferwasser D, Xiong YQ, Palma M, Cheung AL, Bayer AS. 2003. Salicylic acid attenuates virulence in endovascular infections by targeting global regulatory pathways in Staphylococcus aureus. J Clin Invest 112:222-33.
20. Palma M, Bayer A, Kupferwasser LI, Joska T, Yeaman MR, Cheung A. 2006. Salicylic acid activates sigma factor B by rsbU-dependent and -independent mechanisms. J Bacteriol 188:5896-903.
21. Kupferwasser LI, Yeaman MR, Shapiro SM, Nast CC, Sullam PM, Filler SG, Bayer AS. 1999. Acetylsalicylic acid reduces vegetation bacterial density, hematogenous bacterial dissemination, and frequency of embolic events in experimental Staphylococcus aureus endocarditis through antiplatelet and antibacterial effects. Circulation 99:2791-7.
22. Guelcher SA, Brown KV, Li B, Guda T, Lee BH, Wenke JC. 2011. Dual-purpose bone grafts improve healing and reduce infection. J Orthop Trauma 25:477-82.
23. Harder AT, An YH. 2003. The mechanisms of the inhibitory effects of nonsteroidal anti-inflammatory drugs on bone healing: a concise review. J Clin Pharmacol 43:807-15.
24. Boles BR, Horswill AR. 2008. Agr-mediated dispersal of Staphylococcus aureus biofilms. PLoS Pathog 4:e1000052.
25. Valour F, Rasigade JP, Trouillet-Assant S, Gagnaire J, Bouaziz A, Karsenty J, Lacour C, Bes M, Lustig S, Benet T, Chidiac C, Etienne J, Vandenesch F, Ferry T, Laurent F, Lyon BJISG. 2015. Delta-toxin production deficiency in Staphylococcus aureus: a diagnostic marker of bone and joint infection chronicity linked with osteoblast invasion and biofilm formation. Clin Microbiol Infect 21:568 e1-11.
26. Beenken KE, Blevins JS, Smeltzer MS. 2003. Mutation of sarA in Staphylococcus aureus limits biofilm formation. Infect Immun 71:4206-11.
27. Beenken KE, Mrak LN, Griffin LM, Zielinska AK, Shaw LN, Rice KC, Horswill AR, Bayles KW, Smeltzer MS. 2010. Epistatic relationships between sarA and agr in Staphylococcus aureus biofilm formation. PLoS One 5:e10790.
28. Gillaspy AF, Hickmon SG, Skinner RA, Thomas JR, Nelson CL, Smeltzer MS. 1995. Role of the accessory gene regulator (agr) in pathogenesis of staphylococcal osteomyelitis. Infect Immun 63:3373-80.
29. Hendrix AS, Spoonmore TJ, Wilde AD, Putnam NE, Hammer ND, Snyder DJ, Guelcher SA, Skaar EP, Cassat JE. 2016. Repurposing the Nonsteroidal Anti-inflammatory Drug Diflunisal as an Osteoprotective, Antivirulence Therapy for Staphylococcus aureus Osteomyelitis. Antimicrob Agents Chemother 60:5322-30.
30. Cech NB, Horswill AR. 2013. Small-molecule quorum quenchers to prevent Staphylococcus aureus infection. Future Microbiol 8:1511-4.
31. Harraghy N, Kerdudou S, Herrmann M. 2007. Quorum-sensing systems in staphylococci as therapeutic targets. Anal Bioanal Chem 387:437-44.
32. Kaufmann GF, Park J, Janda KD. 2008. Bacterial quorum sensing: a new target for anti-infective immunotherapy. Expert Opin Biol Ther 8:719-24.
33. Khan BA, Yeh AJ, Cheung GY, Otto M. 2015. Investigational therapies targeting quorum-sensing for the treatment of Staphylococcus aureus infections. Expert Opin Investig Drugs 24:689-704.
34. Martin CA, Hoven AD, Cook AM. 2008. Therapeutic frontiers: preventing and treating infectious diseases by inhibiting bacterial quorum sensing. Eur J Clin Microbiol Infect Dis 27:635-42.
35. Sakoulas G, Moellering RC, Jr., Eliopoulos GM. 2006. Adaptation of methicillin-resistant Staphylococcus aureus in the face of vancomycin therapy. Clin Infect Dis 42 Suppl 1:S40-50.
36. Lauderdale KJ, Boles BR, Cheung AL, Horswill AR. 2009. Interconnections between Sigma B, agr, and proteolytic activity in Staphylococcus aureus biofilm maturation. Infect Immun 77:1623-35.
37. Suligoy CM, Lattar SM, Noto Llana M, Gonzalez CD, Alvarez LP, Robinson DA, Gomez MI,

Buzzola FR, Sordelli DO. 2018. Mutation of Agr Is Associated with the Adaptation of Staphylococcus aureus to the Host during Chronic Osteomyelitis. Front Cell Infect Microbiol 8:18.
38. Smyth DS, Kafer JM, Wasserman GA, Velickovic L, Mathema B, Holzman RS, Knipe TA, Becker K, von Eiff C, Peters G, Chen L, Kreiswirth BN, Novick RP, Shopsin B. 2012. Nasal carriage as a source of agr-defective Staphylococcus aureus bacteremia. J Infect Dis 206:1168-77.
39. Shopsin B, Drlica-Wagner A, Mathema B, Adhikari RP, Kreiswirth BN, Novick RP. 2008. Prevalence of agr dysfunction among colonizing Staphylococcus aureus strains. J Infect Dis 198:1171-4.
40. Gagnaire J, Dauwalder O, Boisset S, Khau D, Freydiere AM, Ader F, Bes M, Lina G, Tristan A, Reverdy ME, Marchand A, Geissmann T, Benito Y, Durand G, Charrier JP, Etienne J, Welker M, Van Belkum A, Vandenesch F. 2012. Detection of Staphylococcus aureus delta-toxin production by whole-cell MALDI-TOF mass spectrometry. PLoS One 7:e40660.
41. Diekema DJ, Richter SS, Heilmann KP, Dohrn CL, Riahi F, Tendolkar S, McDanel JS, Doern GV. 2014. Continued emergence of USA300 methicillin-resistant Staphylococcus aureus in the United States: results from a nationwide surveillance study. Infect Control Hosp Epidemiol 35:285-92.
42. Lu S, McGough MAP, Shiels SM, Zienkiewicz KJ, Merkel AR, Vanderburgh JP, Nyman JS, Sterling JA, Tennent DJ, Wenke JC, Guelcher SA. 2018. Settable polymer/ceramic composite bone grafts stabilize weight-bearing tibial plateau slot defects and integrate with host bone in an ovine model. Biomaterials 179:29-45.
43. Brittain HG, Elder BJ, Isbester PK, Salerno AH. 2005. Solid-state fluorescence studies of some polymorphs of diflunisal*. Pharm Res 22:999-1006.
44. Hafeman AE, Zienkiewicz KJ, Carney E, Litzner B, Stratton C, Wenke JC, Guelcher SA. 2010. Local delivery of tobramycin from injectable biodegradable polyurethane scaffolds. J Biomater Sci Polym Ed 21:95-112.
45. Hafeman AE, Li B, Yoshii T, Zienkiewicz K, Davidson JM, Guelcher SA. 2008. Injectable biodegradable polyurethane scaffolds with release of platelet-derived growth factor for tissue repair and regeneration. Pharm Res 25:2387-99.
46. Lowinger MB, Barrett SE, Zhang F, Williams RO, 3rd. 2018. Sustained Release Drug Delivery Applications of Polyurethanes. Pharmaceutics 10.
47. Wenke JC, Guelcher SA. 2011. Dual delivery of an antibiotic and a growth factor addresses both the microbiological and biological challenges of contaminated bone fractures. Expert Opin Drug Deliv 8:1555-69.
48. Stewart PS. 1996. Theoretical aspects of antibiotic diffusion into microbial biofilms. Antimicrob Agents Chemother 40:2517-22.
49. Stewart PS. 1998. A review of experimental measurements of effective diffusive permeabilities and effective diffusion coefficients in biofilms. Biotechnol Bioeng 59:261-72.
50. Stewart PS. 2003. Diffusion in biofilms. J Bacteriol 185:1485-91.
51. Stewart PS, White B, Boegli L, Hamerly T, Williamson KS, Franklin MJ, Bothner B, James GA, Fisher S, Vital-Lopez FG, Wallqvist A. 2019. Conceptual Model of Biofilm Antibiotic Tolerance that Integrates Phenomena of Diffusion, Metabolism, Gene Expression, and Physiology. J Bacteriol doi:10.1128/JB.00307-19.
52. Sanchez CJ, Jr., Prieto EM, Krueger CA, Zienkiewicz KJ, Romano DR, Ward CL, Akers KS, Guelcher SA, Wenke JC. 2013. Effects of local delivery of D-amino acids from biofilm-dispersive scaffolds on infection in contaminated rat segmental defects. Biomaterials 34:7533-43.
53. Johnson CT, Garcia AJ. 2015. Scaffold-based anti-infection strategies in bone repair. Ann Biomed Eng 43:515-28.
54. Johnson CT, Wroe JA, Agarwal R, Martin KE, Guldberg RE, Donlan RM, Westblade LF, Garcia AJ. 2018. Hydrogel delivery of lysostaphin eliminates orthopedic implant infection by Staphylococcus aureus and supports fracture healing. Proc Natl Acad Sci U S A 115:E4960-

E4969.
55. Li B, Davidson JM, Guelcher SA. 2009. The effect of the local delivery of platelet-derived growth factor from reactive two-component polyurethane scaffolds on the healing in rat skin excisional wounds. Biomaterials 30:3486-94.
56. Li B, Yoshii T, Hafeman AE, Nyman JS, Wenke JC, Guelcher SA. 2009. The effects of rhBMP-2 released from biodegradable polyurethane/microsphere composite scaffolds on new bone formation in rat femora. Biomaterials 30:6768-79.
57. Talley AD, Boller LA, Kalpakci KN, Shimko DA, Cochran DL, Guelcher SA. 2018. Injectable, compression-resistant polymer/ceramic composite bone grafts promote lateral ridge augmentation without protective mesh in a canine model. Clin Oral Implants Res 29:592-602.
58. Talley AD, Kalpakci KN, Shimko DA, Zienkiewicz KJ, Cochran DL, Guelcher SA. 2016. Effects of Recombinant Human Bone Morphogenetic Protein-2 Dose and Ceramic Composition on New Bone Formation and Space Maintenance in a Canine Mandibular Ridge Saddle Defect Model. Tissue Eng Part A 22:469-79.
59. Cong Y, Quan C, Liu M, Liu J, Huang G, Tong G, Yin Y, Zhang C, Jiang Q. 2015. Alendronate-decorated biodegradable polymeric micelles for potential bone-targeted delivery of vancomycin. J Biomater Sci Polym Ed 26:629-43.
60. Karau MJ, Schmidt-Malan SM, Greenwood-Quaintance KE, Mandrekar J, Cai J, Pierce WM, Jr., Merten K, Patel R. 2013. Treatment of Methicillin-resistant Staphylococcus aureus experimental Osteomyelitis with bone-targeted Vancomycin. Springerplus 2:329.
61. Vidlak D, Kielian T. 2016. Infectious Dose Dictates the Host Response during Staphylococcus aureus Orthopedic-Implant Biofilm Infection. Infect Immun 84:1957-1965.

CHAPTER 5

DIFLUNISAL-LOADED POLY(PROPYLENE SULFIDE) NANOPARTICLES OUTLINE A DRUG DELIVERY PLATFORM TO AMELIORATE *S. AUREUS*-INDUCED BONE LOSS DURING OSTEOMYELITIS

Abstract

Osteomyelitis is a debilitating infection of bone, often resulting in increased rates of morbidity and mortality. *Staphylococcus aureus* is the most commonly isolated pathogen causing bone infections and boasts an arsenal of virulence factors such as phenol soluble modulins that contribute to bone destruction. Previous studies have reported that diflunisal, a non-steroidal anti-inflammatory drug (NSAID), ameliorates bacterial-mediated bone destruction during osteomyelitis. However, due to the limited aqueous solubility of diflunisal, local delivery using a polyurethane drug depot was necessary. Despite standard-of-care antibiotic therapy during diflunisal delivery, bacterial colonization of the local delivery device was observed. Therefore, diflunisal delivery using parenterally-delivered poly(propylene sulfide) nanoparticles (PPS NPs) was assessed to circumnavigate infectious complications with local delivery. We first characterized the size and encapsulation of diflunisal-loaded PPS NP. Next, we demonstrated the ability for PPS NP to selectively accumulate at the infectious focus in a murine model of osteomyelitis. Finally, we determine that diflunisal-loaded PPS NP ameliorate *S. aureus*-mediated bone destruction during osteomyelitis. Thus, diflunisal delivery using PPS NP achieves previously reported osteomyelitis treatment without the complications associated with local delivery depots.

Introduction

Osteomyelitis, or inflammation of bone, is an infection-associated disease that afflicts 1 in 4,000 people annually and causes substantial morbidity and mortality (1). On a systems level, osteomyelitis causes high economic burden and strain on US healthcare in part due to the extreme difficulty of eliminating infections in the bone microenvironment (2, 3). *Staphylococcus aureus* is among the most common pathogens causing bone infection (4). Factors that contribute to the success of *S. aureus* as a pathogen include the asymptomatic nasal colonization in 30% of the human population, an array of adhesins that promote attachment to host tissue, and production of factors like Staphylococcal protein A that inhibit immune clearance (5-8). Furthermore, *S. aureus* boasts an arsenal of virulence factors such as phenol soluble modulins (PSMs) that lyse host cells, including bone-forming osteoblasts, thereby contributing to osteomyelitis-induced bone loss (9). Thus, effective therapies are necessary to eradicate osteomyelitis-related infections and ameliorate concomitant morbidity such as bone loss that may increase the risk of fracture.

The foundation of current osteomyelitis treatment is long-term, systemically-administered antibiotics such as intravenous vancomycin (2). Given increasing rates of antibiotic resistance resulting in treatment failure, alternative approaches are being investigated (10). However, it has been reported that up to 90% of the drugs in the developmental pipeline are considered poorly soluble, limiting the development of novel therapeutic strategies (11). Local delivery from scaffolds or drug depots provide a simple solution to hydrophobic agent delivery (12). Recently, our laboratory has demonstrated that local delivery of diflunisal, a nonsteroidal anti-inflammatory drug (NSAID) with limited aqueous solubility, from polyurethane foams ameliorates *S. aureus*-induced cortical bone destruction by inhibiting quorum sensing-induced toxin production during osteomyelitis (13, 14). However, this result was juxtaposed with bacterial colonization of the

polyurethane foam (14). Furthermore, avascular surfaces are known to be a haven for bacterial adherence and colonization (15). Consequently, infectious complications can be exacerbated when using a local delivery device to treat osteomyelitis.

Systemic nanoparticle (NP) delivery platforms have been proposed to circumvent limitations of systemic free-drug delivery by providing a vehicle for solubilizing hydrophobic compounds (16-19). Previous work in our laboratory has shown that polypropylene sulfide (PPS) NPs provide a reactive oxygen species (ROS)-responsive drug release platform for delivery of GANT-58, a hydrophobic chemotherapeutic compound, to sites of bone metastasis (20). PPS NPs accumulate at the tumor site by the well-known enhanced permeability and retention (EPR) effect (21). Because numerous diseases such as infection result in increased ROS levels, ROS-responsive materials provide an inflammation-mediated degradative release mechanism to accomplish more targeted release with demand-dependent release kinetics (22, 23). Thus, development of a NP platform capable of delivering hydrophobic compounds to treat osteomyelitis would allow for future investigation of multiple novel small molecules currently in the developmental pipeline.

In the present study, we hypothesized that systemic delivery of diflunisal encapsulated in PPS NPs to infectious foci would inhibit bacterial-mediated bone destruction during osteomyelitis. To test this, we analyzed the encapsulation of diflunisal within PPS NP and investigated the accumulation of PPS NP at an infectious focus using a murine osteomyelitis model. Next, we investigated the ability for PPS NP to ameliorate *S. aureus* cytotoxicity *in vitro*. Finally, we investigated the ability of diflunisal-loaded PPS NP to ameliorate *S. aureus*-induced bone loss during osteomyelitis *in vivo*.

Materials and Methods

Cell lines, bacterial strains, and reagents

The MC3T3-E1 subclone 14 cell line was obtained from the American Type Culture Collection (ATCC) and propagated in a humidified 37°C incubator at 5% CO_2 according to ATCC recommendations. The cells were maintained in α-MEM (Gibco #A1049001), supplemented with 10% fetal bovine serum (FBS, Atlanta Biologicals) and 1x penicillin-streptomycin (ThermoFisher). MC3T3 cells were seeded on 96-well plates at 5,000 cells/well for cytotoxicity assays. An erythromycin-sensitive USA300-lineage strain of LAC *S. aureus* was used for all experiments. For bacterial growth, unless otherwise noted 5-mL cultures were grown in tryptic soy broth (TSB) at 37°C and shaking at 180 rpm. Diflunisal, dimethyl formamide (DMF), dioxane, N,N-dimethylacrylamide (DMA), propylene sulfide, dimethylsulfoxide (DMSO), 2,2'-azobis(isobutyronitrile) (AIBN), and hydrogen peroxide (H_2O_2) were purchased from Sigma-Aldrich. CellTiter 96® AQ One Solution was purchased from Fisher Scientific, and Cy7-amine was purchased from Lumiprobe. DMA was purified by distillation under reduced pressure prior to polymerization. Polypropylene sulfide (10 kDa) and poly(benzoyloxypropyl methacrylamide) pHPMA-Bz were synthesized as described previously (24).

Synthesis and characterization of the fluorescent di-block co-polymer

Synthesis of the poly(propylene sulfide)-*b*-poly-(Cy7-*ran*-dimethylacrylamide) (PPS_{135}-*b*-P(Cy7-*ran*-DMA_{149})) was conducted as previously published with modifications as follows (20). Synthesis of poly(propylene sulfide)-4-cyano-4-(ethylsulfanylthiocarbonyl)sulfanylpentanoic acid (PPS_{135}-ECT, 10 kDa) was performed as previously described (20, 23). In brief, PPS was formed by anionic ring-opening polymerization and then conjugated to ECT via a Steglich esterification reaction. PPS_{135}-ECT serves as the macro-chain transfer agent (CTA) of the

reversible addition-fragmentation chain transfer (RAFT) polymerization of the second block. The RAFT polymerization of the second block of poly(propylene sulfide)-*b*-poly-(pentafluorophenyl acrylate-*ran*-dimethylacrylamide) PPS_{135}-*b*-P(PFPA-*ran*-DMA_{149}) was performed with a macroCTA:initiator (azobisisobutyronitrile, AIBN) molar ratio of 5:1. The polymerization was conducted in a 10-mL, round-bottom reaction vessel containing 0.02687 mmol (268.7 mg) macroCTA, 4.02 mmol (415 μL) DMA, 0.0067 mmol (1.1 μL) PFPA, 0.0054 mmol (88.3 μL of 10 mg/ml AIBN solution in dioxane) AIBN, and 4 mL of 1:1::dimethylformamide:dioxane solvent. The reaction vessel was nitrogen-purged for 30 minutes prior to stirring and heating the solution to 65°C for 24 hours before quenching the reaction by placing the reaction vessel at -80°C. Without opening the reaction vessel, the solution was thawed. To graft Cy7-Amine, 0.5 mL of thawed solution was removed and replaced with 0.5 mL DMSO containing 0.00672 mmol (4.8 mg) of Cy7-amine. Following 24 hours of stirring at room temperature, the green solution was dialyzed against methanol and deionized water for 24 hours each before freezing at -80°C and lyophilization.

Formation and characterization of nanoparticles

Polymeric micellar nanoparticles (NPs) were fabricated by microfluidics processes performed previously (25). Briefly, PPS_{135}-*b*-P(Cy7-*ran*-DMA_{149}) (60.0 mg) was co-dissolved with pHPMA-Bz (6.0 mg) and diflunisal (6.0 mg) in methanol (0.6 mL) and mixed with sterile PBS using a benchtop NanoAssemblr (Precision Nanosystems Inc., Vancouver, Canada). All formulations were prepared with a 10:1::aqueous:organic flow rate ratio (FRR) and 4 mL/min total flow rate (TFR). Methanol was removed from the resulting solution using a rotovap and a water bath heated to 40°C. The resulting micelle solution was passed through a 0.45-μm syringe filter producing the

final diflunisal-NP (Dif-NP) formulation. NP containing only pHPMA-Bz were also synthesized using the same technique (Empty-NP). Dynamic light scattering (DLS) was used to measure the hydrodynamic diameter (D_h) of the Dif-NP and Empty-NP in PBS using a Malvern Zetasizer Nano-ZS (Malvern Instruments Ltd., Worcestershire, UK) equipped with a 4 mW He Ne laser operating at λ = 632.8 nm. Diflunisal loading was quantified from the measurement of its fluorescence with reference to a standard curve. Dif-NPs in PBS (100 μL) were added in triplicate to a 96-well plate and dissolved by adding an equal volume of DMSO. On the same plate, a standard curve of diflunisal in the same solvent (1:1::DMSO:PBS) was prepared and measured. Fluorescence intensity of diflunisal (ex. 310 nm, em. 420 nm) was measured on a micro-plate reader (Tecan Infinite 500, Tecan Group Ltd., Mannedorf, Switzerland). For diflunisal loading experiments, smaller batches of Dif-NP and Empty-NP were synthesized using a bulk solvent evaporation procedure performed previously (20). Briefly, PPS_{135}-*b*-P(Cy7-*ran*-DMA_{149}) (10.0 mg) was co-dissolved with or without pHPMA-Bz and diflunisal (1.0 mg) in chloroform (0.1 mL) and added dropwise to a vial containing vigorously-stirring filter-sterilized (0.22 μm) PBS. Formulations containing pHPMA-Bz were prepared with a 1:1::pHPMA-Bz:diflunisal ratio. The oil-in-water biphasic solution was left stirring overnight to allow for chloroform evaporation and micelle formation. The resulting micelle solution was passed through a 0.45 μm syringe filter and analyzed as above.

ROS release from PPS NP

The ROS-responsive release profile of a loaded agent from PPS_{135}-*b*-P(Cy7-*ran*-DMA_{149}) (PPS) NPs was assessed as described previously (20, 26). Briefly, H_2O_2 was used as the ROS agent at concentrations of 0%, 0.03%, 0.3%, 3.3% (v/v) in PBS. Nile red-loaded NPs were prepared as

described using dropwise oil-in-water emulsion. Nile red-loaded NPs were exposed to 100 μL of various concentrations of H_2O_2 using a 96-well plate for up to 3 days. Fluorescence intensity of Nile red was monitored using a micro-plate reader (Tecan Infinite 500) at 0, 1, 2, and 3 days after initial exposure. Release of Nile red due to NP oxidation and destabilization was measured by decrease in Nile red fluorescence from the initial time point. Nile red emits a fluorescent signal only when in a hydrophobic environment (27). Therefore, the percent of fluorescent signal lost relative to the previous time point was calculated to characterize the release of a loaded agent from the NP.

Biodistribution of PPS NP

Empty PPS NP that did not contain pHPMA-Bz were delivered in 7-8 week old FVB mice by tail vein injection. Cy7 detection (Ex: 675, Em: 780) was used to characterize NP distribution in whole-body images with 5 s fluorescent exposure on high intensity and small binning with an f/stop value of 8. Mice were imaged at 1h and 24h post NP-injection and imaged using an IVIS imaging system (PerkinElmer, Waltham, MA). Images were analyzed using ROI analysis with Living Image Software (PerkinElmer, Waltham, MA).

Preparation of concentrated supernatants

To prepare concentrated *S. aureus* supernatants, one colony from a tryptic soy agar plate was used to inoculate 15 mL of RPMI (Corning) supplemented with 1% (m/m) Casamino Acids (MilliporeSigma) in a tightly capped 50-mL conical tube. The groups were grown in triplicate in four groups: 2 with free drug (DMSO vehicle [0 μg/mL diflunisal] or 10 μg/mL diflunisal) or 2 with diflunisal in nanoparticles (Empty-NPs as vehicle or Dif-NPs at a concentration of 10 μg/mL

encapsulated diflunisal). Bacteria were grown for 15 hours at 37°C and 180 rpm. A 90-µL sample was taken for CFU enumeration. The remaining sample was combined into a single sample of approximately 45 mL volume. The sample was centrifuged at 4°C for 10 minutes at 4,000g to collect the supernatant. Following sterilization by filtration through a 0.22-µm filter, supernatants were concentrated using Amicon Ultra 3-kDa nominal molecular mass columns. To achieve a final volume of 1.5 mL, unconcentrated supernatants were sequential centrifuged at 4°C for approximately 40 minutes at 4,000g with three consecutive 15-mL volumes, discarding the flow-through between spins. After concentration of the supernatants, the samples were aliquoted on ice and frozen at 80°C before thawing for use in cytotoxicity assays.

MC3T3 cytotoxicity assay

MC3T3 cells were seeded in technical replicates of 10 on a 96-well plate. After 24 hours, the media was removed and replaced with 100 µL media supplemented with 20% (v/v) RPMI with Casamino Acids (vehicle) or concentrated supernatants. An additional set of 10 wells did not have the media changed and served as a background for the colorimetric assay. After 22 hours of stimulation, 100 µL of media supplemented 10% (v/v) with CellTiter 96® AQ_{ueous} One Solution (Promega) was added to the wells receiving vehicle or bacterial supernatants following removal of supernatant media. The plate was incubated an additional 2 hours at 37°C before reading of the absorbance at 490 nm. The absorbance of the background wells was subtracted from that of the experimental wells. The percent viability was expressed as a percentage of the absorbance of the vehicle-treated wells. The experiment was performed in biologic triplicate.

Murine model of osteomyelitis

This study was approved by the Institutional Animal Care and Use Committee of Vanderbilt University Medical Center and conducted in compliance with Animal Welfare Regulations and the principles of the Guide for the Care and Use of Laboratory Animals. Osteomyelitis was induced in 7-8 week female C57BL/6J, FVB/nJ, or BALB/cJ mice (the Jackson Laboratory, Bar Harbor, ME) as previously described (9). An inoculum of ~1×10^6 colony-forming units (CFU) in 2 μL PBS was delivered into murine femurs. Mice that experienced >20% weight loss relative to the initial pre-operative weight were euthanized. Dif-NP and Empty-NP (n=12) were injected via tail vein daily at a volume of 100 μL starting approximately 1h post-infection. A PBS injection was used as a control (n=5) for comparison with empty PPS NP vehicle. Mice were euthanized 14 days post-infection and imaged by IVIS as above. The infected femur, contralateral femur, liver, kidneys, and spleen were then removed and imaged in the IVIS. Images were analyzed using ROI analysis as above. Infected femurs were then analyzed by μCT as described previously (9). Briefly, axial images of each femur were captured with 5.0 μm voxels at 70 kV, 200 μA, 2000 projections per rotation and an integration time of 350 msec in a 10.24 mm field-of-view. Each imaging scan comprised 1635 slices (8.125 mm) of the length of the femur, centered on the mid-diaphysis near the inoculation site as visualized in the scout-view radiographs. Volume of interest (VOI) was limited to the original cortical bone, and any destruction was selected by drawing inclusive contours on the periosteal surface, excluding contours on the endosteal surface. To compare a non-encapsulated diflunisal delivery to Dif-NP, a diflunisal free-drug solution was administered to infected mice via intraperitoneal (IP) injection. Diflunisal free-drug solutions were prepared from a 100 μg/ml stock solution of diflunisal in 100% ethanol (EtOH). Diflunisal stock was diluted in a 4.8 mM NaOH in PBS. HCl was added to the solution to a final concentration of 1.3 mM and the resulting solution was filter sterilized. Diflunisal was injected at a dose of 15 mg/kg in 200 μl

q12h starting the time of infection.

Statistical evaluation

Differences in diflunisal encapsulation was assessed by 2-way ANOVA. Differences in nanoparticle biodistribution analysis was assessed by paired student's *t* test. Differences in Nile red release was assessed by a paired student's *t* test with a *p*-value of ≤ 0.05 considered significant for all analyses. Differences in cortical bone destruction were compared using a 1-way ANOVA.

Results

PPS-DMA di-block co-polymers form nanoparticles and encapsulate diflunisal

To generate the building blocks necessary for fluorescent micellar NP synthesis, PPS-*b*-P(DMA-*ran*-Cy7) polymer was synthesized by RAFT polymerization as demonstrated previously (**Fig. 5.1A**) (20). Through an oil-in-water emulsion the polymer chains form micellar NPs in which the hydrophobic PPS block forms the core and the hydrophilic DMA block forms the hydrophilic corona as shown in the cartoon of **Fig. 5.1B**. The DMA block is a random copolymer originally containing PFPA, with which Cy7-amine was substituted. Within the hydrophobic core, water insoluble or minimally soluble drugs (e.g. diflunisal) can be effectively encapsulated for parenteral delivery. In ROS-rich environments (e.g. infectious sites), ROS-mediated oxidation of the sulfur within the PPS core increases hydrophilicity of the core, therefore destabilizing the NP structure resulting in the release of drug cargo (**Fig. 5.1B**). To characterize the encapsulation profile of diflunisal within the PPS NP, diflunisal and polymer were solubilized in the organic phase and emulsified within sterile PBS. Diflunisal loading was tested over two drug-to-polymer ratios to maximize drug loading while minimizing required polymer, characterized by loaded concentration and encapsulation efficiency. Additionally, poly(N-(2-benzoyloxypropyl)methacrylamide)

(pHPMA-Bz) was added to a subset of trials to determine the influence of facilitated π-π stacking on diflunisal encapsulation (28). Increasing the drug-to-polymer ratio from 1:10 to 1:4 was not found to improve drug loading (**Fig. 5.1C**). However, co-encapsulation with pHPMA-Bz approximately doubled the loading of diflunisal compared to mono-encapsulation (**Fig. 5.1D**). Thus, the optimal encapsulation profile of diflunisal in PPS NP was determined to be a drug-to-polymer ratio of 1:10 and co-encapsulation with pHPMA-Bz at a 1:1 diflunisal:pHPMA-Bz ratio. The unloaded (Empty-NP) and diflunisal-loaded nanoparticle (Dif-NP) formulations were evaluated by dynamic light scattering (DLS) to determine the average hydrodynamic diameter (D_h) (**Fig. 5.1E)**. The observed diameters for Empty-NPs and Dif-NPs were 65.4 ± 0.4 nm and 65.4 ± 0.4 nm, respectively, showing minimal changes upon loading of drug cargo. Similarly, the PDI values for Empty-NPs and Dif-NPs were 0.138 ± 0.004 and 0.163 ± 0.009, respectively, demonstrating a similar dispersity of NP size between both formulations. Therefore, diflunisal is most effectively encapsulated in PPS NP at a drug:polymer ratio of 1:10 with pHPMA-Bz, and this formulation does not alter NP size compared to Empty-NPs. Moreover, the size of both NP formulations is optimal for parenteral delivery (29).

Systemically administered PPS NPs accumulate at infected femurs during osteomyelitis

Having identified the optimal NP formulation, we evaluated systemic biodistribution *in vivo.* FVB/NJ mice were injected with Empty-NP by tail vein injection and imaged on IVIS at 1 and 24 hours post-injection. Using fluorescent imaging of the conjugated Cy7, it was observed that Empty-NPs rapidly distribute throughout the systemic circulatory system and are gradually cleared with continued fluorescent signal at 24 hours (**Fig. 5.2A**). Considering that nanoparticles with diameters <100 nm have been observed to accumulate at sites of primary and metastatic tumors

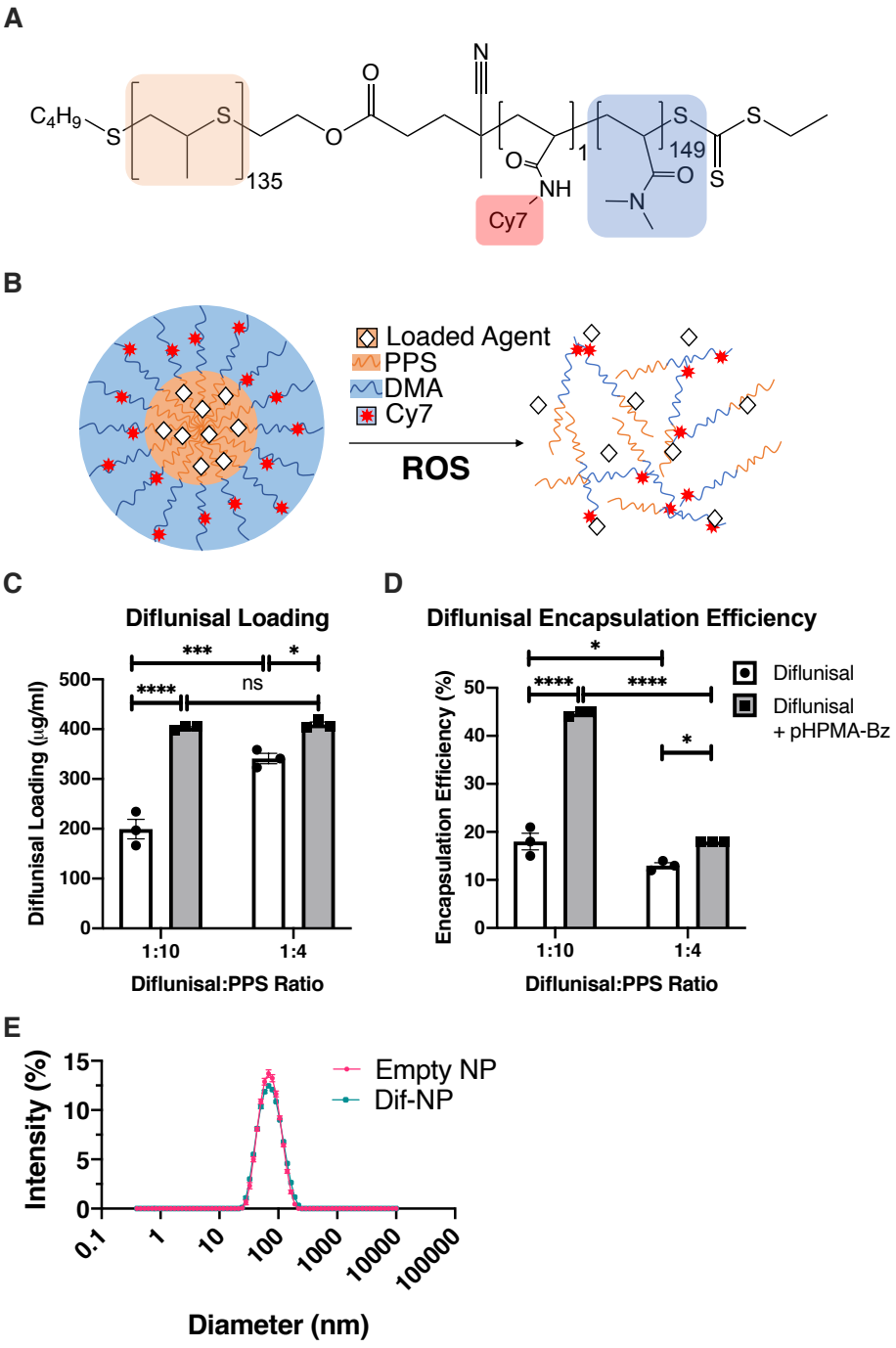

Figure 5.1. PPS_{135}-b-P(Cy7-ran-DMA_{149}) NPs load diflunisal with no effect on nanoparticle size. (A) PPS_{135}-b-P(Cy7-ran-DMA_{149}) structure contains repeat units of PPS (orange), Cy7 (red), and DMA (blue). (B) Schematic of micellar PPS NP encapsulating a loaded agent (diflunisal). Upon oxidation by reactive oxygen species (ROS), PPS NPs becomes unstable and degrade to release loaded agent. Diflunisal encapsulation was quantified by (C) loading and (D) encapsulation efficiency. N=3. Error bars represent SEM. * denotes $p < 0.05$, ** denotes $p < 0.01$, **** denotes $p < 0.0001$ as determined by two-way ANOVA. (E) Nanoparticle diameter (D_h) was analyzed for Empty-NP and Dif-NP.

through passive and active means (30), we anticipated that nanoparticles would target inflamed and injured bone tissue associated with post-traumatic osteomyelitis by similar mechanisms. FVB/NJ mice were infected in a post-traumatic osteomyelitis model with *S. aureus* and subsequently treated with Empty-NP to assess the biodistribution of NP during osteomyelitis and measure accumulation at the infectious site. Previously, we have tested C57Bl6 mice in this model but sought to use a non-pigmented mouse to improve imaging analysis. We first confirmed that bacterial burdens did not differ in the femurs of infected C57Bl6J mice and FVB mice (**Supp. Fig. 5.1**). At 24 hours post-infection, mice were intravenously administered Empty-NPs. Organs of the mice were then harvested and immediately assessed by IVIS to determine fluorescent signal intensity at 2 hours, 8 hours, and 24 hours, post-injection (**Supp. Fig. 5.2**). While raw values at 2 hours indicated that organs involved in nanoparticle clearance (i.e., livers, kidneys, and spleens) showed high signal intensity, the infected femurs showed gradual accumulation over the next 22 hours (**Fig. 5.2B**). The other organs tested exhibited gradual signal declines following the 2-hour timepoint, further suggesting that nanoparticles accumulate in infected femurs (**Fig. 5.2B**). On day 14 post-infection, following 14 daily NP administrations, animals were imaged and found to have substantial increases in fluorescent signal intensity in the infected limb compared to the contralateral limb (**Fig. 5.2C**). When assessed *ex vivo*, infected femurs at day 14 post-infection with daily NP injection showed significantly greater signal intensity compared to all other tested organs (**Fig. 5.2D**). Thus, repeated daily injections of Empty-NP demonstrate accumulation of PPS NPs at the infected femur.

ROS mediates degradation-controlled agent release from NP in vitro

A distinguishing characteristic of PPS compared to other NP-based delivery platforms (e.g. PLGA

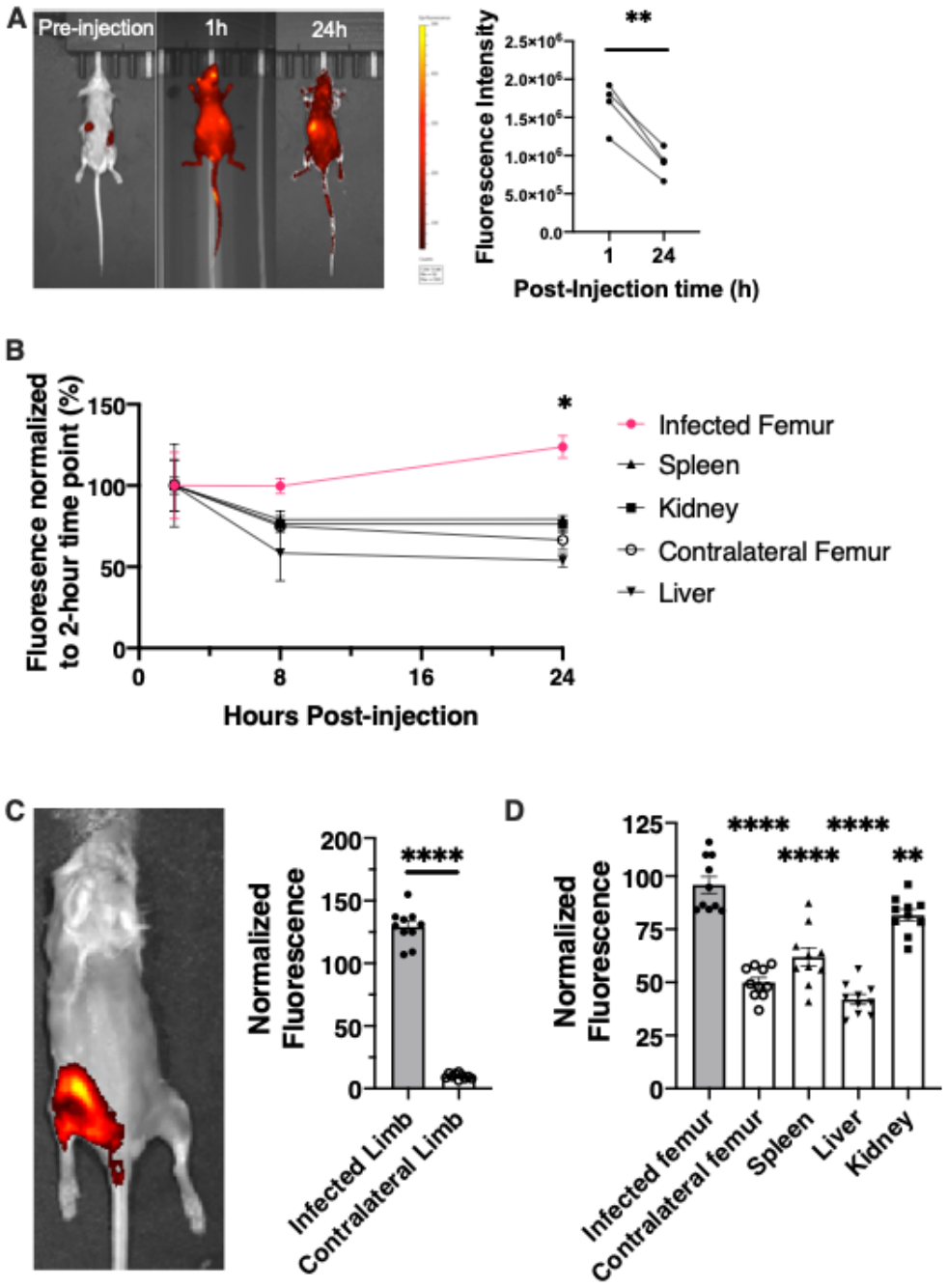

Figure 5.2. PPS_{135}-b-P(Cy7-ran-DMA_{149}) NPs selectively accumulate at infected femurs during osteomyelitis. (A) Whole-body IVIS images of Empty-NP in non-infected mice 1 and 24 h post-injection. ROI analysis of the entire animal was quantified at 1h and 24h post-injection. ** denotes $p<0.01$ as determined by a paired Student's t test. (B) Time course analysis of Cy7 fluorescent signal accumulated in organs during osteomyelitis. N=3 mice per group. Error bars represent SEM. * denotes $p < 0.05$ as determined by 2-way ANOVA. (C) IVIS image of mouse 14 days-post infection. Representative group received daily tail vein injections of Dif-NP or Empty-NP. Fluorescence of infected and contralateral femurs were assessed using ROI analysis of the limbs. N=10 mice per group. Error bars represent SEM. **** denotes $p < 0.0001$ as determined by Student's t test. (D) Quantification of organs ex vivo 14 days post-infection following daily tail vein injections of Dif-NP or Empty-NP. N=10 mice per group. Error bars represent SEM. ** denotes $p < 0.01$ and **** denotes $p < 0.0001$ as determined by 1-way ANOVA.

NP) is the ROS-responsive degradation-dependent release mechanism mediated by the oxidation of sulfur atoms in the PPS core (26). To assess the oxidative degradation release kinetics, Nile red was encapsulated in PPS NP and incubated in H_2O_2 solutions (0 - 3.3%) *in vitro*. Nile red fluorescence requires that the compound reside in hydrophobic environments such as the PPS core (27). Thus, the rate of release of Nile red into the oxidative medium was measured by the decrease in fluorescent signal over time. The release of Nile red from PPS NPs increased over time and with increasing H_2O_2 concentration over a 3-day period, demonstrating the ROS-mediated release kinetics of encapsulated drug from these NPs (**Fig. 5.3**). Thus, the release of loaded agents from PPS NP is mediated by an ROS degradation mechanism.

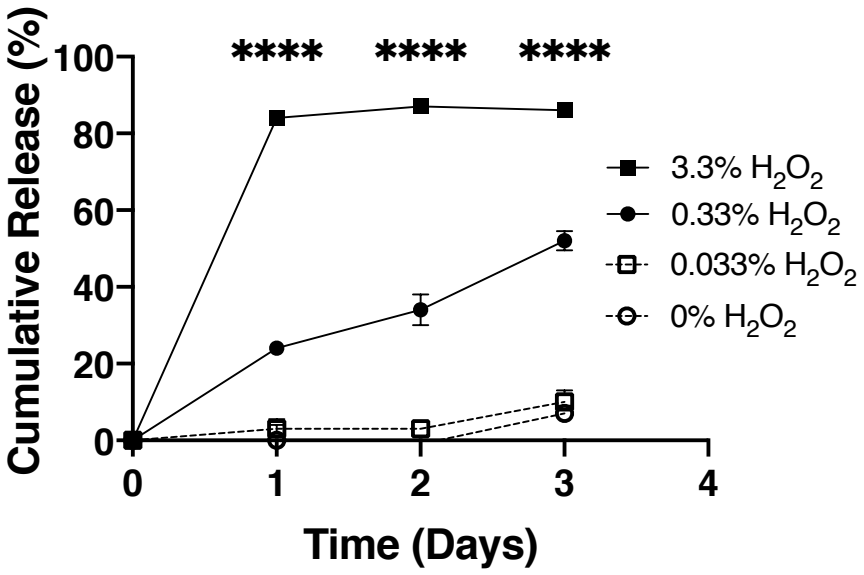

Figure 5.3. Release of loaded agent from PPS_{135}-b-P(Cy7-ran-DMA_{149}) NP is mediated by ROS concentration. Cumulative release of Nile red from Nile red-loaded NP exposed to various concentrations of H_2O_2. Error bars represent SEM. **** denotes $p<0.0001$ between the individual 0.33% and 3.3% H_2O_2 groups and all other groups at the given timepoint as determined by 2-way ANOVA.

Dif-NPs limit S. aureus cytotoxicity without impacting bacterial burden

Before assessing whether PPS NPs efficaciously deliver diflunisal, we used a previously published *in vitro* assay to measure functional changes in cytotoxicity of *S. aureus* supernatants (13). We

added Empty-NPs and Dif-NPs to overnight cultures of *S. aureus* in RPMI supplemented with casamino acids and grew the cultures anaerobically to increase production of cytolytic factors as previously shown (13, 31). We treated MC3T3 cells with the concentrated supernatants for 24 hours and observed that diflunisal as a free drug or encapsulated in PPS NPs significantly inhibited cytotoxicity of *S. aureus* supernatants (**Fig. 5.4A**). We observed a minor but significant difference between bacterial burden after the 15 hour growth of cultures for supernatant preparation; however, because bacterial burdens *in vivo* were unaffected in previous studies, we anticipated Dif-NPs would not affect bacterial burdens *in vivo* (**Fig. 5.4B**). Further investigation into the effects of diflunisal on bacterial growth demonstrated that a significant difference between bacterial growth was observed between 7-10 hours post-inoculation (**Supp. Fig. 5.3**). Yet, this difference was not observed after 10 hours post-inoculation. Moreover, Empty-NPs did not demonstrate a significant decrease in bacterial burden after 15 hours of bacterial growth. Thus, diflunisal released from Dif-NP inhibits *S. aureus* cytotoxicity.

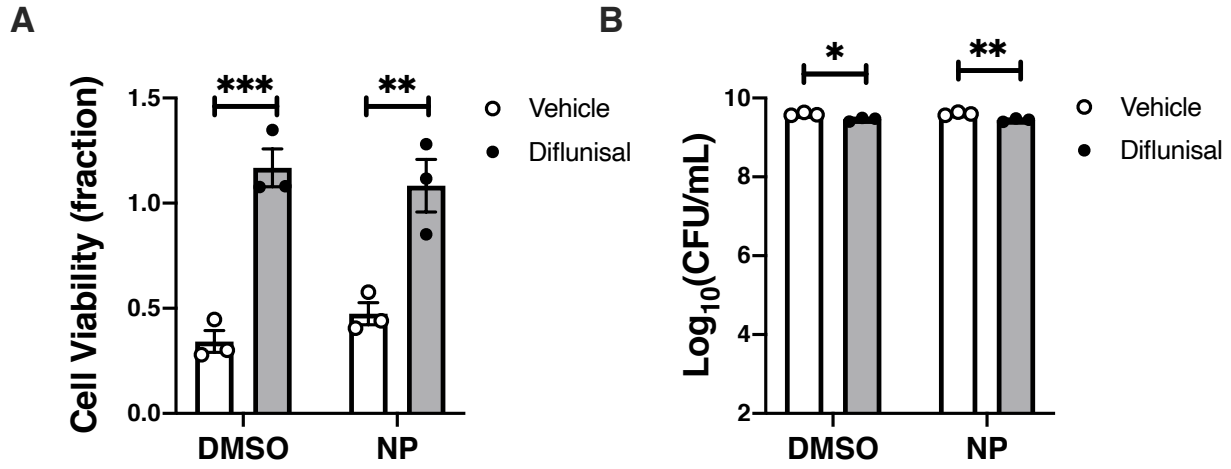

Figure 5.4. Dif-NP inhibits S. aureus cytotoxicity toward murine osteoblasts. (A) MC3T3 murine pre-osteoblast cells were intoxicated with 20% (v/v) of concentrated supernatant from S. aureus grown in the presence of vehicle control (DMSO), NP vehicle control (Empty-NP), diflunisal (10 µg/ml in DMSO), or diflunisal (10 µg/ml encapsulated in NP). Fractional MC3T3 viability is depicted relative to mock intoxication with sterile RPMI. N=3. Error bars represent SEM. ** denotes $p<0.01$ and *** denotes $p<0.001$ as determined by 2-way ANOVA. (B) CFU enumeration of S. aureus cultured in same groups as (A). N=3. Error bars represent SEM. * denotes $p<0.01$ and ** denotes $p<0.001$ as determined by 2-way ANOVA.

Dif-NPs ameliorate S. aureus-induced cortical bone loss during osteomyelitis

Given the observation that diflunisal released from Dif-NP inhibited the production of cytolytic factors from *S. aureus in vitro*, and given the biodistribution results demonstrating preferential accumulation to the infected femur, we sought to determine the ability for Dif-NP to ameliorate *S. aureus*-induced bone loss during osteomyelitis. Prior to implementing PPS NPs, we attempted to limit cortical bone destruction through the administration of diflunisal by intraperitoneal (IP) injection. Due to limited solubility in aqueous buffers, IP injection allows a greater total delivery of diflunisal compared to tail vein injection because it permits delivery of larger volumes. Although showing efficacy in limiting cytotoxicity *in vitro*, systemically delivered free diflunisal does not impact cortical bone destruction (**Supp. Fig. 5.4A-B**). However, IV delivery of diflunisal encapsulated in PPS NPs causes significant reduction in cortical bone destruction during

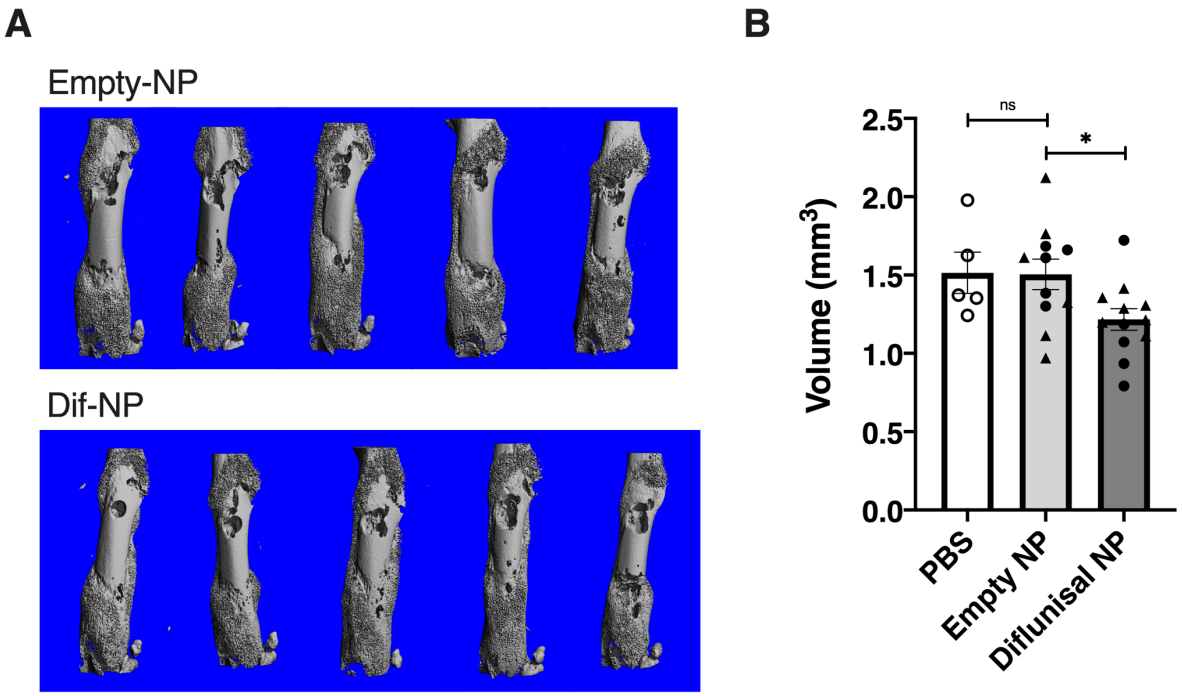

Figure 5.5. Dif-NPs ameliorate S. aureus-induced bone destruction during osteomyelitis. (A) Representative µCT reconstructions of infected femurs 14 days post-infection treated with Empty-NP or Dif-NP via tail vein injection. N=12 mice per group. One mouse in the Empty-NP experienced >20% weight loss and was euthanized. (B) Quantification of cortical bone destruction for mice treated with Empty-NP or Dif-NP via tail vein injection. Error bars represent SEM. * denotes $p<0.05$ as determined by 1-way ANOVA.

osteomyelitis (**Fig. 5.5A-B**). Thus, PPS-NPs provide a parenteral platform for diflunisal therapy to ameliorate *S. aureus*-induced bone loss in an infected femur during osteomyelitis.

Discussion

Poor solubility of novel compounds that are currently in development for disease treatment limits our ability to inhibit morbidity and mortality associated with osteomyelitis and other infectious diseases. It has been reported that up to 90% of the drugs in the developmental pipeline are considered poorly soluble (11). Solubilization approaches such as polymeric micelles (*e.g.* Genexol-PM) have improved the safety and tolerability of chemotherapy medications such as paclitaxel and cisplatin (16). These polymeric micelles not only improve agent solubility allowing for parenteral delivery, but also reduce host exposure to toxic compounds and extend agent circulation times (30, 32). Currently, limited solubilities of clinical and experimental small molecule antibiotics require reformulation with aqueous compatible carriers (33). For example, ciprofloxacin is an antibiotic used to treat different types of severe infections. Due to a limited solubility in water at neutral pH, addition of lactic acid as a pH modifier in each infusion is necessary to improve ciprofloxacin solubility. Therefore, development of delivery platforms capable of delivering hydrophobic compounds systemically is critical to potentiate the activity of novel therapeutics for osteomyelitis treatment.

In this study, we evaluated the efficacy of synthetic NPs to deliver diflunisal, a quorum-quenching compound with limited aqueous solubility, to an infection in bone using an established mouse model of osteomyelitis. Previous studies have reported that local diflunisal therapy inhibited *S. aureus*-mediated bone destruction during osteomyelitis (13); however, bacterial colonization of the delivery device and delivery of a single, diffusion-controlled dose necessitated the development of an alternative delivery strategy (14). Therefore, we sought to develop an

improved method that could accomplish distribution of local administration without the complicating factors associated with local delivery. Due to the limited aqueous solubility of diflunisal, we hypothesized that PPS NPs would allow for parenteral diflunisal delivery, eliminating the need for a local delivery device and permitting the possibility for repeated administrations without sacrificing therapeutic potency. Testing this hypothesis in a model of invasive staphylococcal disease is important given the limited solubility of several clinically-used (e.g. ciprofloxacin) and experimental antibiotics (11, 33). We discovered that PPS NPs preferentially distribute to the infectious focus in our murine model of post-traumatic osteomyelitis. Importantly, NPs augmented with diflunisal demonstrated a substantial reduction in bone destruction 14 days post-inoculation similar to previous studies. Therefore, PPS NPs effectively deliver diflunisal to the infectious focus in a preclinical murine model of post-traumatic osteomyelitis. Moreover, ROS-mediated release of Nile red outlines the uniform release profile of loaded agents. During infections, the antibacterial immune responses produce ROS en masse (34). Furthermore, ROS are frequently produced in injured tissues such as traumatic fracture in the pretext to post-traumatic osteomyelitis (22). Thus, enhanced release of loaded compounds from PPS NPs at the infected femur is anticipated compared to other sites within the body due to elevated concentrations of ROS. Given that hydrophobic agents will be effectively encapsulated within PPS NPs, delivery of other hydrophobic small molecules using this platform should be investigated in the context of infection treatment. Specifically, further research will focus on improving antibiotic delivery for osteomyelitis therapy to understand the ability for antibiotic-loaded PPS NPs to eradicate infections from the bone microenvironment.

NPs were utilized primarily to improve the solubility of diflunisal in this study; however, synthetic biomaterials resembling PPS NPs offer various other advantages for small molecule

delivery (20). Synthetic NPs offer an intrinsic modularity to accommodate diverse requirements. Alendronate (a nitrogenous bisphosphonate) has been used previously as a conjugated, bone-targeting moiety in a PPS NP composition to increase the concentration of GANT-58 in the bone microenvironment (24). Bisphosphonates are used clinically to reduce osteoclast-mediated bone resorption and serve as an optimal targeting agent due to a high affinity to hydroxyapatite in bone (35). Since inflammatory states such as osteomyelitis induce bone loss in part by accelerated osteoclastogenesis (36), addition of alendronate into the NP corona should be studied as a dual-purpose bone-targeting moiety and anti-resorptive agent in osteomyelitis treatment with PPS-NPs as has been done with alternative drug delivery systems (18, 19, 37). In the case of recurrent infections associated with biofilm formation, significant improvement of antibiotic delivery is necessary to identify and eradicate these bacterial communities. Drug penetration of biofilms is currently limited due to the formation of an extracellular matrix (ECM) encasing a sessile bacterial community (38-44). Further engineering of this NP platform should be investigated for the ability to potentiate antibiotic penetration into the biofilm. The modular basis of this NP platform not only allows for the preferential accumulation of a broad range of hydrophobic therapeutic agents loaded in the nanoparticle, but also establishes a platform for targeted delivery to improve small molecule infection treatment through conjugation of ECM- or bacteria-targeted moieties to the NP corona.

Limitations of this study include the use of only one bacterial strain, a single endpoint of 14 days, and use of a single infection model. Due to the different pathogenic profiles of various bacterial species, future studies should explore the use of alternative bacterial species to understand PPS NP delivery to different infectious foci. *S. aureus* was chosen to model infection in bone due to its high association with bone infection, yet PPS NP delivery to infections in other organs has yet to be studied. Similarly, a focus on treatment timing should be investigated to understand PPS

NP therapy with loaded agents at various times post-inoculation to understand the effect of infection establishment on preferential distribution. Although NP platforms are commonly used to decrease host exposure to toxic compounds, this was not an outcome assessed during this study due to the relative safety of loaded diflunisal. Therefore, future studies should focus on the ability of PPS NPs to decrease deleterious exposure of the host to toxic agents. Although ROS-mediated release was demonstrated *in vitro*, more extensive *in vivo* analyses must be performed to conclude that ROS-mediated release is the primary mechanism of drug release at the infectious site. Nevertheless, this work suggests that PPS NPs provide a robust small molecule delivery platform for osteomyelitis therapy.

References

1. Kremers HM, Nwojo ME, Ransom JE, Wood-Wentz CM, Melton LJ, 3rd, Huddleston PM, 3rd. 2015. Trends in the epidemiology of osteomyelitis: a population-based study, 1969 to 2009. J Bone Joint Surg Am 97:837-45.
2. Lew DP, Waldvogel FA. 2004. Osteomyelitis. Lancet 364:369-79.
3. Kurtz SM, Lau E, Watson H, Schmier JK, Parvizi J. 2012. Economic burden of periprosthetic joint infection in the United States. J Arthroplasty 27:61-5 e1.
4. Hatzenbuehler J, Pulling TJ. 2011. Diagnosis and management of osteomyelitis. Am Fam Physician 84:1027-33.
5. Foster TJ, Hook M. 1998. Surface protein adhesins of Staphylococcus aureus. Trends Microbiol 6:484-8.
6. Sakr A, Bregeon F, Mege JL, Rolain JM, Blin O. 2018. Staphylococcus aureus Nasal Colonization: An Update on Mechanisms, Epidemiology, Risk Factors, and Subsequent Infections. Front Microbiol 9:2419.
7. Dossett JH, Kronvall G, Williams RC, Jr., Quie PG. 1969. Antiphagocytic effects of staphylococfcal protein A. J Immunol 103:1405-10.
8. Forsgren A, Nordstrom K. 1974. Protein A from Staphylococcus aureus: the biological significance of its reaction with IgG. Ann N Y Acad Sci 236:252-66.
9. Cassat JE, Hammer ND, Campbell JP, Benson MA, Perrien DS, Mrak LN, Smeltzer MS, Torres VJ, Skaar EP. 2013. A secreted bacterial protease tailors the Staphylococcus aureus virulence repertoire to modulate bone remodeling during osteomyelitis. Cell Host Microbe 13:759-72.
10. Ghosh C, Sarkar P, Issa R, Haldar J. 2019. Alternatives to Conventional Antibiotics in the Era of Antimicrobial Resistance. Trends Microbiol 27:323-338.
11. Loftsson T, Brewster ME. 2010. Pharmaceutical applications of cyclodextrins: basic science and product development. J Pharm Pharmacol 62:1607-21.
12. Guelcher SA, Brown KV, Li B, Guda T, Lee BH, Wenke JC. 2011. Dual-purpose bone grafts improve healing and reduce infection. J Orthop Trauma 25:477-82.
13. Hendrix AS, Spoonmore TJ, Wilde AD, Putnam NE, Hammer ND, Snyder DJ, Guelcher SA,

Skaar EP, Cassat JE. 2016. Repurposing the Nonsteroidal Anti-inflammatory Drug Diflunisal as an Osteoprotective, Antivirulence Therapy for Staphylococcus aureus Osteomyelitis. Antimicrob Agents Chemother 60:5322-30.
14. Spoonmore TJ, Ford CA, Curry JM, Guelcher SA, Cassat JE. 2020. Concurrent local delivery of diflunisal limits bone destruction but fails to improve systemic vancomycin efficacy during Staphylococcus aureus osteomyelitis. Antimicrob Agents Chemother doi:10.1128/AAC.00182-20.
15. Zimmerli W, Waldvogel FA, Vaudaux P, Nydegger UE. 1982. Pathogenesis of foreign body infection: description and characteristics of an animal model. J Infect Dis 146:487-97.
16. Oerlemans C, Bult W, Bos M, Storm G, Nijsen JF, Hennink WE. 2010. Polymeric micelles in anticancer therapy: targeting, imaging and triggered release. Pharm Res 27:2569-89.
17. Danhier F, Ansorena E, Silva JM, Coco R, Le Breton A, Preat V. 2012. PLGA-based nanoparticles: an overview of biomedical applications. J Control Release 161:505-22.
18. Cong Y, Quan C, Liu M, Liu J, Huang G, Tong G, Yin Y, Zhang C, Jiang Q. 2015. Alendronate-decorated biodegradable polymeric micelles for potential bone-targeted delivery of vancomycin. J Biomater Sci Polym Ed 26:629-43.
19. Karau MJ, Schmidt-Malan SM, Greenwood-Quaintance KE, Mandrekar J, Cai J, Pierce WM, Jr., Merten K, Patel R. 2013. Treatment of Methicillin-resistant Staphylococcus aureus experimental Osteomyelitis with bone-targeted Vancomycin. Springerplus 2:329.
20. Vanderburgh JP, Kwakwa KA, Werfel TA, Merkel AR, Gupta MK, Johnson RW, Guelcher SA, Duvall CL, Rhoades JA. 2019. Systemic delivery of a Gli inhibitor via polymeric nanocarriers inhibits tumor-induced bone disease. J Control Release 311-312:257-272.
21. Greish K. 2010. Enhanced permeability and retention (EPR) effect for anticancer nanomedicine drug targeting. Methods Mol Biol 624:25-37.
22. Dunnill C, Patton T, Brennan J, Barrett J, Dryden M, Cooke J, Leaper D, Georgopoulos NT. 2017. Reactive oxygen species (ROS) and wound healing: the functional role of ROS and emerging ROS-modulating technologies for augmentation of the healing process. Int Wound J 14:89-96.
23. Gupta MK, Meyer TA, Nelson CE, Duvall CL. 2012. Poly(PS-b-DMA) micelles for reactive oxygen species triggered drug release. J Control Release 162:591-8.
24. Vanderburgh J, Hill JL, Gupta MK, Kwakwa KA, Wang SK, Moyer K, Bedingfield SK, Merkel AR, d'Arcy R, Guelcher SA, Rhoades JA, Duvall CL. 2020. Tuning Ligand Density To Optimize Pharmacokinetics of Targeted Nanoparticles for Dual Protection against Tumor-Induced Bone Destruction. ACS Nano 14:311-327.
25. Elsana H, Olusanya TOB, Carr-Wilkinson J, Darby S, Faheem A, Elkordy AA. 2019. Evaluation of novel cationic gene based liposomes with cyclodextrin prepared by thin film hydration and microfluidic systems. Sci Rep 9:15120.
26. Poole KM, Nelson CE, Joshi RV, Martin JR, Gupta MK, Haws SC, Kavanaugh TE, Skala MC, Duvall CL. 2015. ROS-responsive microspheres for on demand antioxidant therapy in a model of diabetic peripheral arterial disease. Biomaterials 41:166-75.
27. Greenspan P, Fowler SD. 1985. Spectrofluorometric studies of the lipid probe, nile red. J Lipid Res 26:781-9.
28. Shi Y, van Steenbergen MJ, Teunissen EA, Novo L, Gradmann S, Baldus M, van Nostrum CF, Hennink WE. 2013. Pi-pi stacking increases the stability and loading capacity of thermosensitive polymeric micelles for chemotherapeutic drugs. Biomacromolecules 14:1826-37.
29. Moghimi SM, Hunter AC, Murray JC. 2001. Long-circulating and target-specific nanoparticles: theory to practice. Pharmacol Rev 53:283-318.
30. Albanese A, Tang PS, Chan WC. 2012. The effect of nanoparticle size, shape, and surface chemistry on biological systems. Annu Rev Biomed Eng 14:1-16.
31. Wilde AD, Snyder DJ, Putnam NE, Valentino MD, Hammer ND, Lonergan ZR, Hinger SA, Aysanoa EE, Blanchard C, Dunman PM, Wasserman GA, Chen J, Shopsin B, Gilmore MS, Skaar

EP, Cassat JE. 2015. Bacterial Hypoxic Responses Revealed as Critical Determinants of the Host-Pathogen Outcome by TnSeq Analysis of Staphylococcus aureus Invasive Infection. PLoS Pathog 11:e1005341.
32. Patra JK, Das G, Fraceto LF, Campos EVR, Rodriguez-Torres MDP, Acosta-Torres LS, Diaz-Torres LA, Grillo R, Swamy MK, Sharma S, Habtemariam S, Shin HS. 2018. Nano based drug delivery systems: recent developments and future prospects. J Nanobiotechnology 16:71.
33. Kalepu S, Nekkanti V. 2015. Insoluble drug delivery strategies: review of recent advances and business prospects. Acta Pharm Sin B 5:442-53.
34. Fang FC. 2011. Antimicrobial actions of reactive oxygen species. mBio 2.
35. Bilezikian JP. 2009. Efficacy of bisphosphonates in reducing fracture risk in postmenopausal osteoporosis. Am J Med 122:S14-21.
36. Mbalaviele G, Novack DV, Schett G, Teitelbaum SL. 2017. Inflammatory osteolysis: a conspiracy against bone. J Clin Invest 127:2030-2039.
37. Rotman SG, Thompson K, Grijpma DW, Richards RG, Moriarty TF, Eglin D, Guillaume O. 2020. Development of bone seeker-functionalised microspheres as a targeted local antibiotic delivery system for bone infections. J Orthop Translat 21:136-145.
38. Flemming HC. 2016. EPS-Then and Now. Microorganisms 4.
39. Flemming HC, Wingender J. 2010. The biofilm matrix. Nat Rev Microbiol 8:623-33.
40. Jefferson KK, Goldmann DA, Pier GB. 2005. Use of confocal microscopy to analyze the rate of vancomycin penetration through Staphylococcus aureus biofilms. Antimicrob Agents Chemother 49:2467-73.
41. Stewart PS. 1996. Theoretical aspects of antibiotic diffusion into microbial biofilms. Antimicrob Agents Chemother 40:2517-22.
42. Stewart PS. 1998. A review of experimental measurements of effective diffusive permeabilities and effective diffusion coefficients in biofilms. Biotechnol Bioeng 59:261-72.
43. Stewart PS. 2003. Diffusion in biofilms. J Bacteriol 185:1485-91.
44. Stewart PS, White B, Boegli L, Hamerly T, Williamson KS, Franklin MJ, Bothner B, James GA, Fisher S, Vital-Lopez FG, Wallqvist A. 2019. Conceptual Model of Biofilm Antibiotic Tolerance that Integrates Phenomena of Diffusion, Metabolism, Gene Expression, and Physiology. J Bacteriol doi:10.1128/JB.00307-19.

Supplemental Figures:

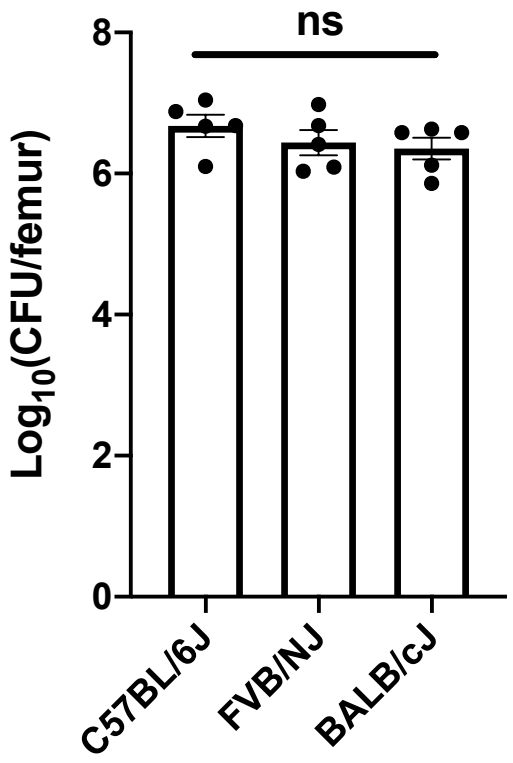

Supplementary Figure 5.1. Bacterial burdens in C57BL/6J, FVB, and BALB/cJ mice 7 days post-infection. N=5 mice per group. Error bars represent SEM. Ns denotes no significance as determined by Student's t test with a p value of 0.05.

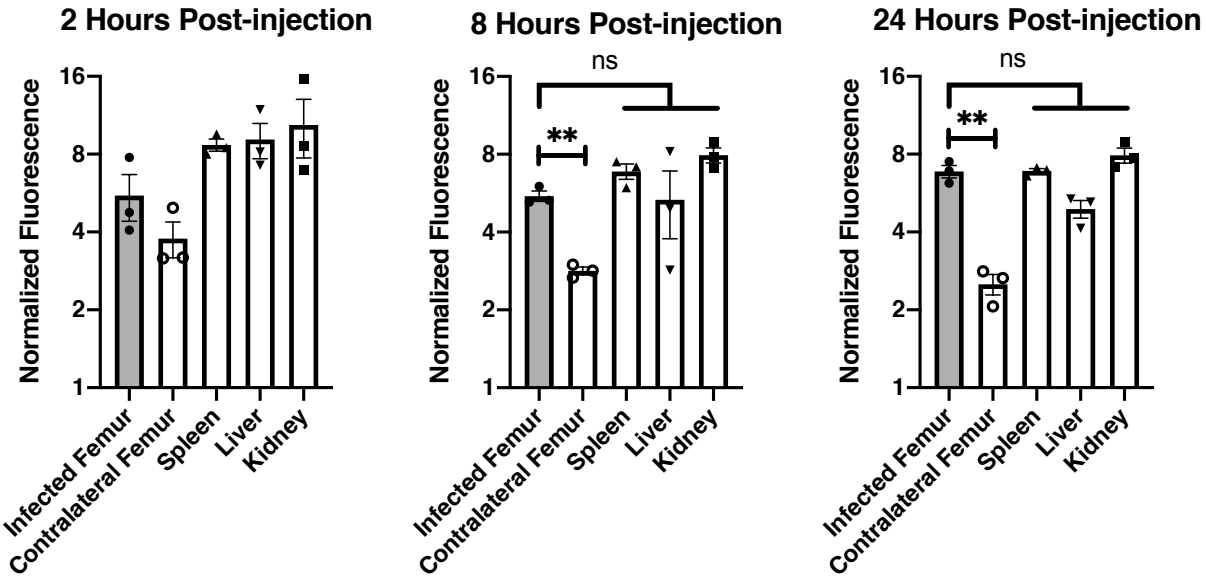

Supplementary Figure 5.2. Cy7 signal in organs 2, 8, and 24 hours post-injection. All organs were compared to the infected femur at each respective time. N=3 for each time point. Error bars represent SEM. ** denotes $p<0.01$ as determined by 1-way ANOVA.

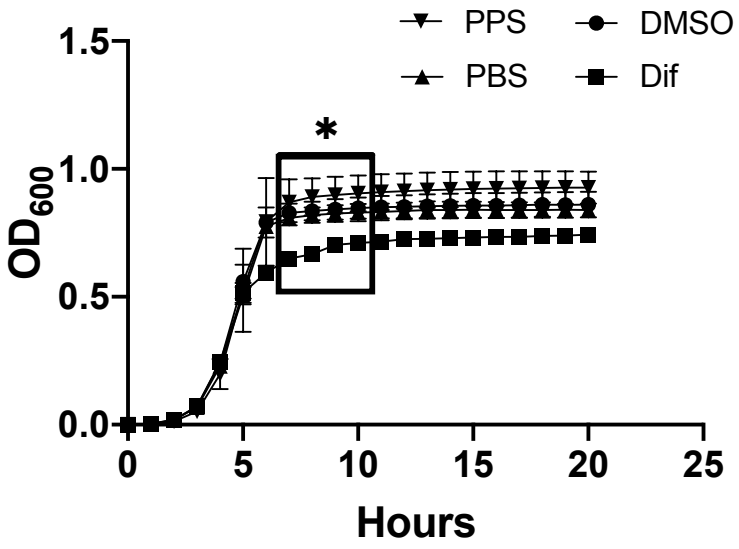

Supplementary Figure 5.3. Diflunisal affects bacterial growth in RPMI + 1% Casamino acids at the end of exponential growth. Bacterial growth in RPMI + 1% Casamino acids containing PBS (vehicle), DMSO (vehicle), 100 µg/mL PPS, or 10 µg/mL diflunisal. N=3. Error bars represent SEM. * denotes $p<0.05$ as determined by 2-way ANOVA.

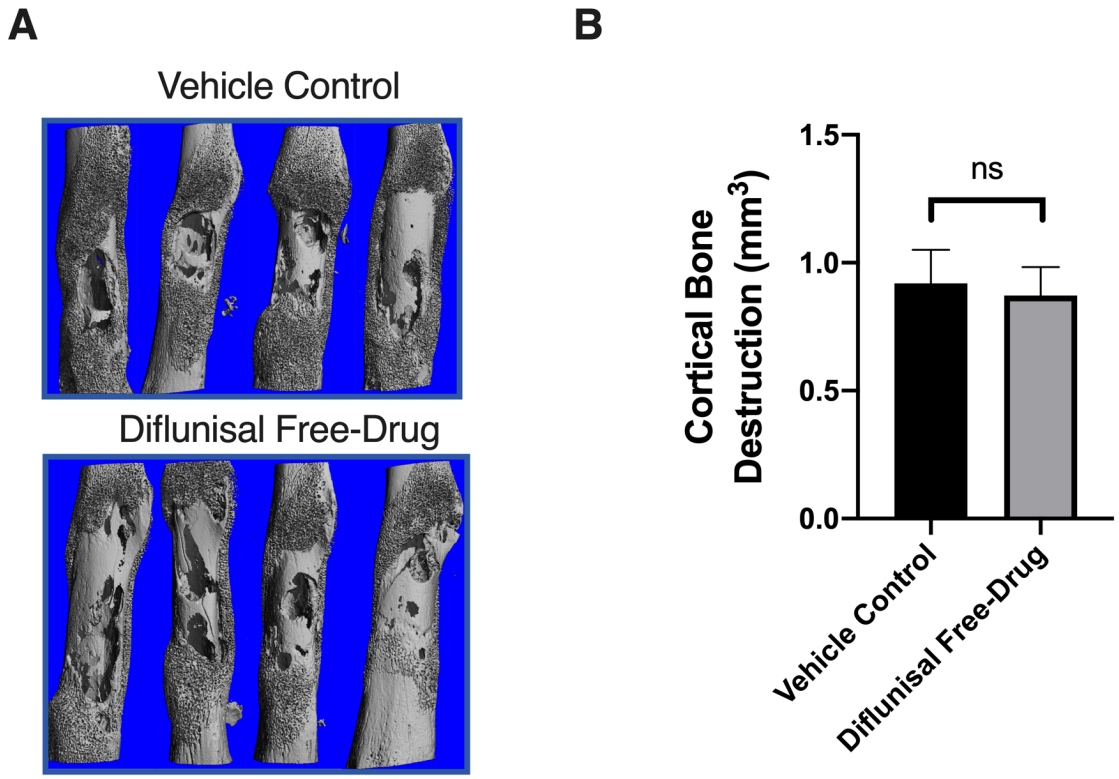

Supplementary Figure 5.4. Parenteral free-drug diflunisal does not inhibit bacterial-mediated bone destruction during osteomyelitis. Mice infected with S. aureus were treated with 15 mg/kg diflunisal via intraperitoneal (IP) delivery. (A) µCT reconstructions of femurs treated with either a vehicle control or diflunisal free drug solution. (B) Quantification of cortical bone destruction for mice treated with Empty-NP or Dif-NP via tail vein injection. Error bars represent SEM. N=4 mice per group. Ns denotes no significance as determined by Student's t test.

CHAPTER 6

SUMMARY AND CONCLUSIONS

This dissertation focused on the investigation of Bacterial biofilms *in vitro* and osteomyelitis treatment *in vivo* with the overall goal of inhibiting bacterial presence in the body and mitigating morbidity associated with osteomyelitis.

Chapter 3 of this dissertation focused on bacteria surviving vancomycin exposure on 2D and 3D surfaces *in vitro*. Vancomycin was used as a surrogate marker for antibiotic recalcitrance. Bacteria populations adherent to a well plate surface was characterized over a 24 h time period and demonstrated the most significant bacterial presence and vancomycin-recalcitrance 24 h post-inoculation. Bacteria separated from the well plate revealed a non-resistant phenotype determined by the minimum inhibitory concentration (MIC) and a susceptibility to vancomycin in the planktonic state at doses that were incapable of killing adherent bacteria. Further investigation determined that a vancomycin and adherent bacteria do not colocalize 100%, and bacteria treated with vancomycin in the planktonic state demonstrate significant increase in bound vancomycin. Therefore, adherent bacterial communities on the well plate surface demonstrate an assemblage of bacteria that are recalcitrant to vancomycin treatment suggesting the presence of a biofilm. These results were further studied on 3D substrates that demonstrated significant morphological differences in trabecular spacing (Tb.Sp.) and structure model index (SMI, representative of surface curvature). UAMS-1 bacteria grown on concave (CV) morphologies representing lower Tb.Sp. and SMI values exhibited a greater vancomycin-tolerant population 24h post-inoculation than convex (CX) morphologies representing higher Tb.Sp. and SMI values. This phenomenon was also investigated on the surface of trabecular reconstructions representing the trabecular networks of different anatomical sites within the human anatomy and revealed a similar effect of

morphology on the vancomycin-recalcitrant populations 24 h post-inoculation. Therefore, **Chapter 3** determined that bacteria adherent to 3D substrates with increased Tb.Sp. and SMI values have lower vancomycin-recalcitrant populations compared to substrates with lower values.

Chapter 4 of this dissertation focused on local administration of a repurposed non-steroidal anti-inflammatory drug (NSAID), diflunisal, to ameliorate *S. aureus*-mediated bone loss during osteomyelitis. Diflunisal demonstrated an ability to inhibit *S. aureus* cytotoxicity *in vitro* toward both murine and human osteoblasts without affecting bacterial growth. Compared to other NSAIDs, diflunisal demonstrated unique activity to potently inhibit *S. aureus* cytotoxicity. Polyurethane (PUR) drug delivery foams proved effective for diflunisal therapy in a murine osteomyelitis model resulting in a significant decrease in bacterial-induced bone destruction. Further research focused on diflunisal as an adjunctive therapy in the context of antibiotic standard-of-care. Bacterial burdens surviving subcutaneously-delivered vancomycin therapy was characterized to develop an antibiotic standard-of-care model in the murine osteomyelitis model. A sub-optimal dose of 10 mg/kg vancomycin was identified with which diflunisal adjunctive therapy would be studied. Vancomycin activity was determined to be unaffected by diflunisal presence *in vitro* proving the possibility for concurrent delivery of diflunisal and vancomycin. Subcutaneous vancomycin combined with local diflunisal therapy did not demonstrate an effect on vancomycin activity. Similarly, diflunisal was unaffected by vancomycin delivery. However, PUR foams used for local diflunisal therapy were colonized by bacteria despite vancomycin treatment. Therefore, **Chapter 4** furthers the field osteomyelitis research by introducing a novel therapy to mitigate the deleterious effects of osteomyelitis during standard-of-care antibiotic therapy. Furthermore, **Chapter 4** also discusses the significant problem of bacterial colonization of materials associated with local drug delivery.

Chapter 5 of this dissertation focused on an improved delivery platform for hydrophobic small molecule osteomyelitis treatment. Because bacterial burdens on the surface of PUR used for local delivery in **Chapter 4** were unaffected by parenteral vancomycin treatment, a nanoparticle (NP) delivery approach was developed to achieve diflunisal delivery without the presence of a foreign device. Reactive oxygen species (ROS)-responsive poly(propylene sulfide) (PPS) NP used previously in cancer therapy were used in this study. Diflunisal was used as a model hydrophobic compound for encapsulation and delivery to osteomyelitis due to the proven activity in **Chapter 4**. Diflunisal loading within the PPS NP was enhanced with the presence of pHPMA-Bz due to π-π stacking. IVIS imaging of Cy7-conjugated PPS NP injected in infected mice demonstrated accumulation of PPS NP at the infected femur. Release of Nile red from PPS NP *in vitro* demonstrated the ROS-responsive degradation release mechanism of loaded agent. Diflunisal-loaded PPS NP demonstrated a significant mitigation of bacterial-mediated bone destruction during osteomyelitis. Therefore, PPS NP can be used as a platform for hydrophobic small molecule delivery to an infectious focus during osteomyelitis.

CHAPTER 7

FUTURE DIRECTIONS

Bacterial biofilms continue to contribute to the chronicity of infections such as osteomyelitis, encumbering the healthcare system. This dissertation furthered the field of biofilm research by investigating the development of antibiotic tolerance within adherent bacterial communities on 2D and 3D substrates and furthered osteomyelitis research by demonstrating the ability for diflunisal to ameliorate *S. aureus*-induced bone loss. Development of a NP platform for improved parenteral delivery of hydrophobic compounds to an infectious focus also furthered the field of osteomyelitis treatment and related drug delivery research. The methods and platforms developed in this dissertation provide a basis for future research to further expand the understanding of biofilm progression and develop tools and techniques to mitigate the adverse effects of bacterial infections. The following section outlines future directions of study.

In vitro investigation of antibiotic-tolerant biofilm development

Enhancements to current approach

Chapter 3 outlined the development of an *in vitro* assay that used vancomycin as a surrogate marker for antibiotic recalcitrance within bacterial communities that were adherent to various 2D and 3D substrates. Ongoing biofilm research is currently investigating the multiple different mechanisms for antibiotic tolerance as discussed above. Questions still remain regarding antibiotic diffusion into a biofilm and the binding of vancomycin to actively growing or dormant ‘persister’ cells within the community (1). The direct exposure of biofilms on 2D and 3D substrates to antibiotics *in vitro* allows for the further investigation of antibiotic penetration within a biofilm using confocal microscopy similar to previous studies (2). Similarly, further research can be

performed to test for the presence of metabolically dormant cells within an adherent community to further understand the effect of 'persister' cells on biofilm recalcitrance. Tolerance to other clinically-relevant antibiotic compounds can also be investigated to understand the antibiotic tolerance to compounds such as rifampin (inhibition of RNA synthesis) or erythromycin (inhibition of protein synthesis). This assay can also be expanded to understand the influence of surface morphology on biofilm development of other bacteria such as *Pseudomonas Aeruginosa*, a gram-negative bacterium able to form robust biofilms on various biomaterials and responsible for an array of diseases such as cystic fibrosis (3). Overall, this assay can be used to screen the antibiotic recalcitrance of various bacterial species on different morphological substrates.

Although the primary focus of this *in vitro* assay was to characterize antibiotic tolerance within adherent communities, further investigation using this tool could also lead to a library of effective anti-biofilm compounds. Previous reports have demonstrated the extensive exposure time necessary for vancomycin to eradicate an *in vitro* biofilm on a 3D substrate (4). Future studies should focus on alternative or adjunctive compounds that shorten the time necessary for antibiotic-mediated bacterial eradication. A specific adjunctive strategy has been suggested previously to kill 'persister' compounds that evade traditional antibiotic activity using specific small molecule compounds called anti-persister agents that are reported to be active against dormant bacteria (5). Therefore, a secondary treatment of adherent bacteria following vancomycin will characterize anti-persister activity. Taken together, further investigation with this *in vitro* model seeks to develop a screened library of anti-biofilm compounds as well as a further understanding of substrate morphology influence on other gram-positive and gram-negative bacterial species.

Intravital imaging of bacteria on 3D substrates

While antibiotic recalcitrance of biofilm bacteria requires further investigation *in vitro*, antibiotic delivery to biofilms on avascular surfaces *in vivo* remains a major question. Antibiotic delivery is complicated *in vivo* by the immune response such as the formation of neutrophil extracellular traps (NETosis) (6). Neutrophils release DNA to form a neutrophil extracellular trap (NET) that surrounds and immobilizes invading pathogens (6, 7). Given that diffusion through a biofilm extracellular matrix is a major limitation to antibiotic efficacy (1, 8, 9), additional diffusion through NETs may hinder antibiotic exposure even further. Previous studies have described a 'dead zone' that results from NETosis around *P. aeruginosa* biofilms between bacteria and neutrophils (7). While NETosis response to *S. aureus* is currently being investigated to understand the exchange of signaling factors at the host-pathogen interface, further understanding in regards to the effect of NETosis on antimicrobial delivery is necessary. Therefore, investigation of biofilm development, immune response to bacterial presence, and antibiotic delivery should be studied *in vivo* using the 3D substrates outline in Chapter 3. Utilizing fluorescent dyes to identify host and bacterial cells as well as fluorescently-conjugated antibiotic compounds such as BODIPY-FL vancomycin, an understanding of antibiotic limitations can be developed. Furthermore, this approach can characterize the effect of substrate morphology on bacterial recalcitrance *in vivo*.

Poly(propylene sulfide) Nanoparticle Delivery Platform

Enhancements to Current Approach

Chapter 4 discussed the beneficial effect of locally delivered diflunisal on *S. aureus*-induced bone loss during osteomyelitis. Chapter 5 utilized the outcomes from Chapter 4 to demonstrate to outline the ability for PPS NP to deliver a hydrophobic small molecule to an infectious site during

osteomyelitis. The goal of chapter 5 was to demonstrate the potential for an ROS-responsive NP platform to deliver hydrophobic small molecule compounds to an infectious focus in bone. With up to 90% of developmental drugs reported to have solubility limitations, development of a small molecule carrier is necessary (10). In the search for Paul Ehrlich's magic bullet, overcoming solubility limitations may result in more efficient study of developmental antibiotics and development of more effective treatments. Previous studies have investigated the use of poly(lactic-*co*-glycolic acid) (PLGA) NP as a delivery vehicle for small molecule antibiotics to eradicate bacteria from the bone microenvironment (11). Whereas PLGA NP have proven beneficial in sustained delivery of loaded agents, PPS NP release hydrophobic agents rapidly due to the ROS-mediated degradative release kinetics (12-14). Therefore, PPS NP delivered to a site of increased inflammation, such as in infected bone, could potentially release an increased payload at the target site within a short time. Although diflunisal has proven to have no effect on bacterial burdens (15, 16), we believe that this study demonstrated our ability to use PPS NP as a platform for small molecule delivery to an infected femur. Therefore, future studies will investigate the ability for NP loaded with various bactericidal small molecules to decrease or eradicate bacterial burdens *in vivo*.

Bone- and infection-targeted NP to reduce bacterial burdens during Osteomyelitis

Addition of targeting moieties is frequently utilized to improve NP distribution at the target site (17). The PPS NP used for this study did not contain any targeting or binding ligands in the corona and therefore relied solely on the enhanced permeability and retention (EPR) effect to accumulate at the site of infection. However, previous studies in our laboratory have determined the beneficial effect of conjugating alendronate, a bisphosphonate with an affinity to the inorganic

component in bone, as a targeting ligand in the PPS NP corona (14). Use of alendronate-conjugated NP in an osteomyelitis model should be investigated to determine the benefit of bone-targeted osteomyelitis therapy. Similarly, it has been reported that conjugated phosphate groups promote nanoparticle binding to peptidoglycan in bacterial cell wall of gram-positive pathogens such as *S. aureus* (18). Whereas bone-targeting may improve nanoparticle delivery to the bone microenvironment, targeting the bacteria specifically may optimize delivery to the infected site. Therefore, further investigation is needed to understand the ability and effect of bacterial-targeted NP.

Chapter 5 focused on acute NP delivery for osteomyelitis therapy. However, further study of NP delivery in a chronic osteomyelitis model is also necessary. Recent results were obtained that outlined a recalcitrant infection in an osteomyelitis model due to delayed therapy of free-drug vancomycin (**Fig. 7.2.1**). Briefly, bacterial burdens were assessed 7 days post-inoculation in the murine osteomyelitis model as described in Chapters 4. Mice were injected subcutaneously every 12 h at a dose of 30 mg/kg vancomycin, resembling the protocol described in Chapter 4. The "Acute" group was injected immediately following infection, while the "Delayed" group was injected 24 h post-infection. Interestingly, we observed a difference in bacterial burdens between the two groups treated with 30 mg/kg vancomycin at day 7, while bacterial burdens were not significantly different between groups treated with a vehicle control. We therefore concluded that delayed vancomycin therapy resulted in a recalcitrant infection. Further investigation is necessary to understand the mechanism associated with the recalcitrant infection, followed by an investigation into antibiotic-loaded NP delivery to the recalcitrant infection. Collectively, this NP platform should be used to investigate the effect of PPS NP delivery to eradicate infectious complications from bone.

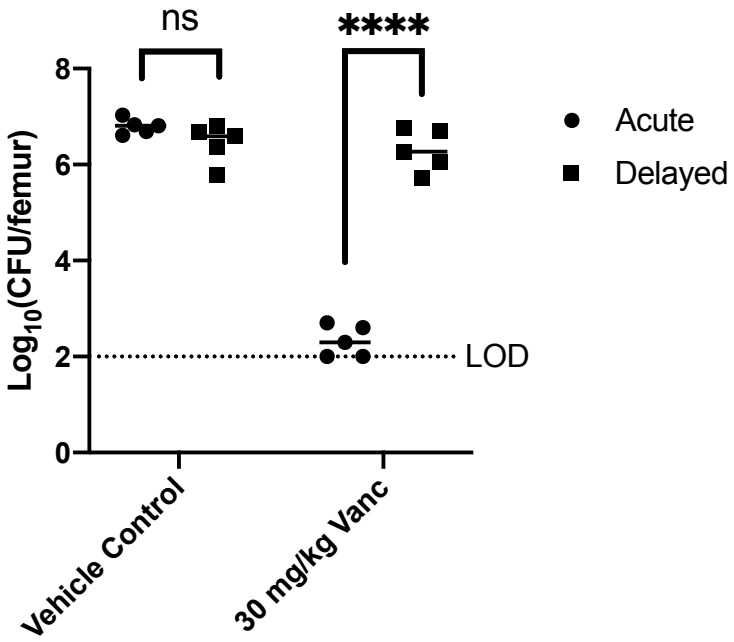

Figure 7.1. Delayed antibiotic therapy results in treatment-recalcitrant infection. Mice infected with S. aureus were treated with 0 (Vehicle Control) or 30 mg/kg vancomycin injected subcutaneously either immediately after infection (Acute) or 24 h post-infection (Delayed). Bacterial burdens were assessed 7 days post-infection. N=5 mice per group. Lines represent the calculated mean. Limit of detection (LOD) = 10^2 CFU/femur. **** denotes $p<0.0001$ as determined by 2-way ANOVA.

References

1. Stewart PS. 2002. Mechanisms of antibiotic resistance in bacterial biofilms. Int J Med Microbiol 292:107-13.
2. Jefferson KK, Goldmann DA, Pier GB. 2005. Use of confocal microscopy to analyze the rate of vancomycin penetration through Staphylococcus aureus biofilms. Antimicrob Agents Chemother 49:2467-73.
3. Mulcahy LR, Isabella VM, Lewis K. 2014. Pseudomonas aeruginosa biofilms in disease. Microb Ecol 68:1-12.
4. Post V, Wahl P, Richards RG, Moriarty TF. 2017. Vancomycin displays time-dependent eradication of mature Staphylococcus aureus biofilms. J Orthop Res 35:381-388.
5. Defraine V, Fauvart M, Michiels J. 2018. Fighting bacterial persistence: Current and emerging anti-persister strategies and therapeutics. Drug Resist Updat 38:12-26.
6. Brinkmann V, Reichard U, Goosmann C, Fauler B, Uhlemann Y, Weiss DS, Weinrauch Y, Zychlinsky A. 2004. Neutrophil extracellular traps kill bacteria. Science 303:1532-5.
7. Thanabalasuriar A, Scott BNV, Peiseler M, Willson ME, Zeng Z, Warrener P, Keller AE, Surewaard BGJ, Dozier EA, Korhonen JT, Cheng LI, Gadjeva M, Stover CK, DiGiandomenico A, Kubes P. 2019. Neutrophil Extracellular Traps Confine Pseudomonas aeruginosa Ocular Biofilms and Restrict Brain Invasion. Cell Host Microbe 25:526-536 e4.
8. Stewart PS. 1996. Theoretical aspects of antibiotic diffusion into microbial biofilms. Antimicrob Agents Chemother 40:2517-22.
9. Stewart PS. 2003. Diffusion in biofilms. J Bacteriol 185:1485-91.
10. Loftsson T, Brewster ME. 2010. Pharmaceutical applications of cyclodextrins: basic science and product development. J Pharm Pharmacol 62:1607-21.
11. Cong Y, Quan C, Liu M, Liu J, Huang G, Tong G, Yin Y, Zhang C, Jiang Q. 2015. Alendronate-decorated biodegradable polymeric micelles for potential bone-targeted delivery of vancomycin. J Biomater Sci Polym Ed 26:629-43.
12. Gupta MK, Meyer TA, Nelson CE, Duvall CL. 2012. Poly(PS-b-DMA) micelles for reactive oxygen species triggered drug release. J Control Release 162:591-8.
13. Poole KM, Nelson CE, Joshi RV, Martin JR, Gupta MK, Haws SC, Kavanaugh TE, Skala MC, Duvall CL. 2015. ROS-responsive microspheres for on demand antioxidant therapy in a model of diabetic peripheral arterial disease. Biomaterials 41:166-75.
14. Vanderburgh J, Hill JL, Gupta MK, Kwakwa KA, Wang SK, Moyer K, Bedingfield SK, Merkel AR, d'Arcy R, Guelcher SA, Rhoades JA, Duvall CL. 2020. Tuning Ligand Density To Optimize Pharmacokinetics of Targeted Nanoparticles for Dual Protection against Tumor-Induced Bone Destruction. ACS Nano 14:311-327.
15. Hendrix AS, Spoonmore TJ, Wilde AD, Putnam NE, Hammer ND, Snyder DJ, Guelcher SA, Skaar EP, Cassat JE. 2016. Repurposing the Nonsteroidal Anti-inflammatory Drug Diflunisal as an Osteoprotective, Antivirulence Therapy for Staphylococcus aureus Osteomyelitis. Antimicrob Agents Chemother 60:5322-30.
16. Spoonmore TJ, Ford CA, Curry JM, Guelcher SA, Cassat JE. 2020. Concurrent local delivery of diflunisal limits bone destruction but fails to improve systemic vancomycin efficacy during Staphylococcus aureus osteomyelitis. Antimicrob Agents Chemother doi:10.1128/AAC.00182-20.
17. Steichen SD, Caldorera-Moore M, Peppas NA. 2013. A review of current nanoparticle and targeting moieties for the delivery of cancer therapeutics. Eur J Pharm Sci 48:416-27.
18. Boucard J, Linot C, Blondy T, Nedellec S, Hulin P, Blanquart C, Lartigue L, Ishow E. 2018. Small Molecule-Based Fluorescent Organic Nanoassemblies with Strong Hydrogen Bonding Networks for Fine Tuning and Monitoring Drug Delivery in Cancer Cells. Small 14:e1802307.

APPENDIX

Relevant protocols

Biofilm *in vitro* assay

Before starting: Read and understand the MSDS of the reagents listed below

- Personal Protective and Safety Equipment required:
    - Disposable nitrile gloves

Reagents:

- Freezer stock of *S. aureus* (UAMS-1 or LAC)
- Tryptic soy agar (TSA) plates
- Phosphate buffered saline (PBS)
- Tryptic soy broth (TSB)
- Vancomycin (10 mg/ml in DMSO)
- Drug/encapsulated species
- Organic solvent
    - Solvent evaporation: water-immiscible solvent ($CHCl_3$, DCM)
    - Nanoprecipitation: water-miscible solvent: (methanol, THF, acetone)
- Aqueous solvent: PBS

Materials and Equipment:

- Sterile wooden sticks
- 1.5 mL microcentrifuge tubes
- 4 mL glass vial (w/ cap)
- Small (0.5”) stir bar
- Rotovap (if nanoprecipitation used)
- Glass Pasteur pipettes
- Auto-pipettors
- 1 mL syringes
- 0.4 μm syringe filter

Procedure:

Streaking bacterial plate

1. In a sterile environment, scrape freezer stock of *S. aureus* bacteria and transfer to one quadrant of TSA plate
2. Spread initial streak to other 3 quadrants using different sterile wooden stick for each spread
3. Place plate in 37°C incubator overnight to grow

Preparation of overnight culture

1. Pick colony from TSA plate and transfer to 5 mL TSB in 15 mL conical tube
2. Place in 37°C with shaking at 180 RPM for at least 12 h (optimally 16 h)

Inoculation

3. Remove overnight culture from incubator and centrifuge at 4,000 RPM for 5 min
4. Aspirate TSB and resuspend bacteria in sterile PBS for washing step
5. Set aside 500 µL for OD_{600} analysis
6. Centrifuge at 4,000 RPM for 5 min
7. Aspirate PBS and resuspend bacteria in fresh TSB
8. Dilute bacteria to desired inoculation concentration in TSB
9. Transfer 1 mL/well of bacteria subcultures and place plate in 37°C incubator with agitation at 80 RPM
    - For colonization studies, proceed to step 14

Vancomycin treatment

10. Aspirate media from well plates and wash 3X with sterile PBS (1 mL/well)
11. Dilute 10 mg/mL vancomycin solution into TSB for desired concentrations
    - 1:100 dilution for 100 µg/ml solution
12. Transfer 1 mL/well of vancomycin solutions to wells with adherent bacteria and place plate in 37°C incubator with agitation at 80 RPM
13. For bacterial resuspension experiments:
    a. Transfer 1 mL/well of sterile PBS to well after step 10
    b. Sonicate plate using a sonicator bath for 5 minutes
    c. Transfer resuspensions from each well to a 1.5 mL microcentrifuge tube
    d. Centrifuge at 14,000g for 5 min
    e. Aspirate PBS
    f. Resuspend bacteria in vancomycin media prepared in step 11
    g. Place in 37°C incubator with agitation at 180 RPM to maintain planktonic state

Bacterial Enumeration

14. Aspirate media from well plates and wash 3X with sterile PBS (1mL/well)
15. Transfer 1 mL/well of sterile PBS to well
16. Sonicate plate using a sonicator bath for 5 minutes
17. Serial dilute (10X) resuspended solutions using sterile PBS in a 96-well plate
18. Plate 10 µL of each serial dilution on TSA plate
    - Calculation: Bacterial enumeration = (# of bacteria counted)$*10^{(\text{Dilution factor})}*10^2$
    - 10^2 represents the 10 µL plated for each serial dilution

Clean-up:

1. Dispose of any solutions containing bacteria into a bleach bucket
2. Collect all glass waste (pipettes, vials, or broken glass) and dispose in the broken glass container (box)
3. Collect all sharps and dispose in the sharps waste container (red box)
4. Collect all solid waste and dispose in the solid waste container
5. Collect all liquid waste and dispose in the appropriate liquid waste container (acetone or halogenated)

6. Clean glassware:
    a. Wash with soap and water
    b. Rinse with acetone and dry in the oven

Bone Scanning

Scanco Medical µCT50 – using µT Tomography V6.3-4
Contact: Sasidhar Uppuganti
Located on the 2nd floor in the Imaging Center, room AA2101

To sign up for time, calculated 60 minutes per scan of each femur + 15 minutes/femur to move the carousel + any extra time to set up the experiment

For load murine femurs:

1. Take the smallest yellow tube in holder, and choose as many tubes as necessary (Each tube fits 3 femurs)
    a. Note the tube numbers (also referred to as carousel #s) and the order of bones to be loaded into each tube (Bone 1-1, 1-2, etc)

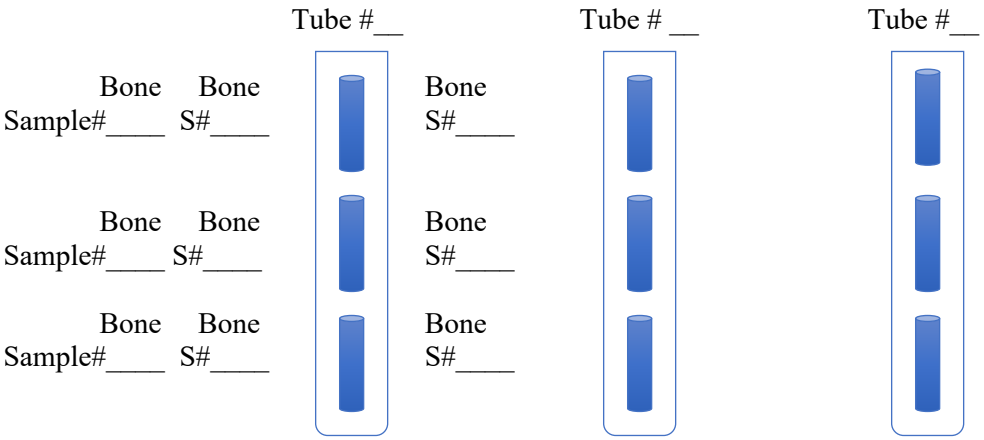

2. Cut out thin squares of foam, can always trim back
    a. Roll foam around femur and load (knee down) into tube in the appropriate order
    b. Push to bottom, and add 10% formalin from Eppendorf tube on top
    c. Use side of tool/spatula to remove bubbles (OK if bone is exposed)
3. Repeat the loading of bones by *gently* stacking on top of each other, paying careful attention not to overlap the bones – try not to squeeze the bone
4. Top off tube with 10% formalin, wipe off any liquid from outer tube!
5. Seal tops with parafilm carefully

µT Tomography V6.3-4

1. Bottom left, click the Scanco button to allow the machine to warm up (~15 minutes); Log in as Jim Cassat
2. Set tubes in holder (should only go in a specific way)
    a. Insert Samples [Yes] → Wait for detection (these carousels should now be recognized by the software
3. Hit [Cancel] [New] to add new information to each sample being run
    a. "JEC_Scan-Date_LAC_Bacteria_Mouse_1-1" etc…

    b. Will give you a Sample# * Record this information in the diagram above
4. To tell Scanco where Sample #s are:
    a. [Other]
    b. Add first Sample#
    c. Click carousel #

   d. Load Controlfile **286: CASSAT, 10mm, 10.0µm, 70kV, 200µA**
   e. [Scout View] of tube
      i. Bottom femur (35-51mm), middle femur (19-35mm), top femur (1-19mm)
   f. [Reference Line] 60.8 minutes, 1088 slices, 10.8mm – center over the area that is most deformed without getting ends
   g. [Add Scan] → Will give you a Task #
   h. Repeat: Change Sample # and Carousel #s when necessary
5. If an extra task is added, can remove after they have all been added by looking at order of tasks under [Task List]
6. [Submit Scans]
7. Will hear a thud noise, screen will close → Samples are running!

Analysis
Contouring or Sequential bone density calculations – Make dots/connecting lines every 50-100 planes, allowing computer fit to double check these.

Bone Scanning Analysis

3D Reconstruction contouring

1. Left click, drag circle around bone
2. Edit → Copy
3. Paste on last slice
4. [C…] [Morph]
5. [T…] Select evaluation script [19: Recon only] and [Default VOI]
6. [Start evaluation]
7. Save
8. Close

3D Reconstruction image generation

1. Hit [3D analysis] button in bottom left corner
2. Select sample #
3. <> All files Seg.Aim:1 [OK]

Misc. info: Buttons to change orientation/view

4. Translation – horizontal and vertical
5. Elevation – pitches forward or backward
6. Roll – rolls 180°
7. *** Do not manipulate light or shadows
8. Scale to 1.1
9. Perspective @ 3.5

10. Load [Start]
11. Orient with the drill hole directly facing forward
12. Save .tiff files
13. File – Print; Print format: TFF
    <> fill <> color
    File name: Scan [Okay]

To make movies

Options → Animations
# of frames = # of pics it will take
Get Settings A: Start point
Get Settings B: End point

Analysis of Cortical Bone (Destruction)

1. Click the 'Graph' button on the bottom left screen to open the Evaluation Program V6.5-3
2. Open the file by looking up the Sample # recorded during the scanning process
3. Contour every 50 to 100 slices; more often within the first 100-150 slices
4. *** Be conservative with contours – better to exclude some than include non-bone
    a. Non-bone will be calculated as bone destruction
5. Clockwise inside the cortical bone – excludes inside of the contour
6. Counterclockwise outside the cortical bone – includes inside the contour

Misc info: Several buttons with red Xs – used to remove contours that have been drawn (can remove individual contour lines, all contours from a slice, all contours from all the slices in a scan)

1. Contour out a total of 818 slices (0-818)
2. Middle click – zoom
3. Right click – move on screen
4. [C…] Select [<> All] and [Morph]
    - Red – indicated this was contoured by the computer between 2 manually contoured areas
    - Yellow – if one of the contours on the ends have been changed, but the intervening slices haven't been [Morph]'d yet to represent this change
5. Save files often (GOBJ file)! Computer may crash.
6. Double check slices in between contours!!
7. [T…] Opens Evaluation panel
7. Select [39: Cassat Lysis Eval]
8. [Start]
9. Save Contours if haven't already

PPS-*b*-P(Aln-*co*-DMA) SYNTHESIS PROTOCOL

Before starting: Read and understand the MSDS of the reagents listed below

- Personal Protective and Safety Equipment required:
    - Disposable nitrile gloves

Reagents:

- PPS-ECT 10kDa (Duvall lab)
- PFPA (pentafluorophenyl acrylate)
- DMA (dimethyl acrylamide, distilled)
- Aln (alendronate)
- DMF
- Dioxane
- AIBN (10 mg/mL solution in dioxane)
- DMSO

Materials and Equipment:

- RAFT calculation spreadsheet
- 4 mL glass vials
- Pipette + pipette tips
- 10 mL reaction flask or Schlenk tube (note: larger reaction flask and solvent volume needed for batch sizes > 500 mg)
- Rubber septum
- Heater/stirrer + thermocouple
- Glass Pasteur pipettes
- Septum penetration needles
- Analytical balance
- 1 kDa Dialysis Tubing
- Dialysis clips
- Large glass beaker (0.5-1 L)
- Saran wrap

Procedure:

PPS-b-P(PFPA-co-DMA) Intermediate Synthesis

1. Set oil bath to 75ºC on heater/stirrer and set stirrer to sufficient rpm (usually 300-600 rpm)
2. Determine batch size and use RAFT calculation spreadsheet to calculate mass of reagents needed
3. Clean out reaction flask/Schlenk tube, rinse with acetone, and place in oven to dry. Add small (1/2") stir bar to reaction flask
4. Weigh out appropriate amount of 10k PPS-ECT into glass vial and dissolve in 4 mL 1:1 DMF:Dioxane – add contents to reaction flask
5. Pipette appropriate amount of PFPA and DMA to reaction flask based on RAFT calculation sheet
    a. These amounts will depend of ratio of Aln:DMA required in the final polymer – ensure RAFT calculation sheet reflects desired final Aln content
6. Pipette appropriate amount of 10 mg/mL AIBN solution into reaction flask based on RAFT calculation sheet

7. Seal reaction flask with rubber stopper and wrap rubber band around neck to secure
8. Degas reaction mixture with argon (or nitrogen) using septum penetration needle for 15 min. Immerse needle into bottom of reaction mixture to "bubble" through the mixture. Be sure to put another syringe needle in top of septum for gas purge
9. Turn off argon and remove purge and septum penetration needle
10. Submerge reaction flask into oil bath and allow reaction to proceed for 24 hr
11. Remove reaction flask from oil bath and remove septum
    a. Set some crude reaction mixture aside (~50-100 μL) for ^{19}F-NMR if desired
12. Precipitate reaction mixture in cold diethyl ether
    a. Add ~30 mL diethyl ether to 50 mL conical
    b. Chill diethyl ether in -80ºC for 5-10 min
    c. Add reaction mixture dropwise to diethyl ether – observe polymer precipitating from solution and settling into bottom of conical
    d. Vortex resulting solution after all reaction mixture added to ether
    e. Centrifuge conical at 1500 rpm for 5 min
    f. Decant and dispose of the supernatant. Precipitated polymer should remain at bottom of centrifuge tube
        i. Be careful not to lose product. Pipette off the supernatant if necessary
    g. Repeat precipitation process by adding ~30 mL of cold diethyl ether to conical and repeating steps 12d-f
13. Dry precipitated polymer in vacuum oven overnight (vacuum, no heat)
14. Save small amount (~10 mg) for NMR and GPC analysis

PPS-b-P(Aln-co-DMA) Synthesis

15. Set oil bath to 50ºC on heater/stirrer and set stirrer to sufficient rpm
16. Determine batch size and use RAFT calculation spreadsheet to calculate mass of reagents needed
17. Clean out reaction flask/Schlenk tube, rinse with acetone, and place in oven to dry. Add small (1/2") stir bar to reaction flask
18. Weigh out appropriate amount of PPS-b-P(PFPA-co-DMA) and Aln and add directly to reaction flask (use weigh paper & funnel)
19. Add 4 mL DMSO (anhydrous) to reaction flask
20. Seal reaction flask with rubber stopper and wrap rubber band around neck to secure
21. Degas briefly with argon using septum penetration needle to clear head space. Be sure to put another syringe needle in top of septum for gas purge
22. Turn off argon and remove purge and septum penetration needle
23. Submerge reaction flask into oil bath and allow reaction to proceed for 24 hr. Ensure stirrer is vigorously stirring to facilitate solubilization of polymer and Aln
24. Dialyze PPS-b-P(Aln-co-DMA)
    a. Cut sufficient amount of 1 kDA MW cutoff dialysis tubing
    b. Prepare large beaker filled with DI water and stir bar
    c. Pre-wet dialysis tubing in DI water, fold one side over and clip with dialysis clip (preferably a weighted clip) or twist-tie
    d. Pipette reaction mixture into open end of dialysis tube (re-wet the tubing and rub tubing between fingers if having difficulty opening the tubing)

e. Fold over excess tubing and apply dialysis clip to other end
f. To ensure clips are secured, wrap rubber band around open ends of dialysis clips
g. Add dialysis tube to beaker containing DI water and stir
    i. Suspend above stir bar by tethering to side of beaker or rod laying over top of beaker
    ii. Cover beaker with saran wrap to prevent significant evaporation
    iii. Note: clear DMSO should be observed diffusing through dialysis membrane. If colored liquid (i.e. polymer solution) is observed diffusing out near the tube ends, remove and ensure dialysis tubing is securely clipped
h. Allow dialysis to proceed for 48 h, changing the dialysis DI water at least twice
i. Remove dialysis tube from beaker and unclip one end of the tube
    i. Tube should be swelled up and a murky yellow-brown color (depending on Aln content)
j. Pipette out contents into 50 mL conical tube and freeze in -80ºC for > 30 min

25. Lyophilize for at least 24 hr. Resulting polymer should be an off-white/yellow/light brown (depending on Aln content) solid
26. Save small amount (~10 mg) for NMR and GPC analysis

Fluorescent labeling

19. Perform same steps until Step 18. Instead, weigh out appropriate amount of PPS-b-P(PFPA-co-DMA) and amine-functional fluorescent label (have successfully used Cy5-amine and Cy7-amine from Lumiprobe)
    a. Typically 1:1 polymer:fluorophore mole ratio
20. Proceed with Steps 19-23
21. After reaction proceeds for 24 h, add appropriate amount of Aln directly to reaction flask containing reaction mixture (use weigh paper & funnel)
22. Allow this reaction to proceed for 24 h
23. Continue with Step 24, however start with methanol as dialysis solvent instead of DI water to dialyze excess fluorophore. After 24 h in methanol, allow dialysis to proceed for 48 h in DI water, changing the dialysis DI water at least twice
24. Proceed with remaining dialysis steps and Steps 25-26

Clean-up:

7. Collect all glass waste (pipettes, vials, or broken glass) and dispose in the broken glass container (box)
8. Collect all sharps and dispose in the sharps waste container (red box)
9. Collect all solid waste and dispose in the solid waste container
10. Collect all liquid waste and dispose in the appropriate liquid waste container (acetone or halogenated)
11. Clean glassware:
    a. Wash with soap and water
    b. Rinse with acetone and dry in the oven

POLYMER MICELLE SYNTHESIS PROTOCOL

Before starting: Read and understand the MSDS of the reagents listed below

- Personal Protective and Safety Equipment required:
  - Disposable nitrile gloves
- Prep rotovap
  - Add liquid N_2 to cold trap and start cooling tower

Reagents:

- Polymer
- Drug/encapsulated species
- Organic solvent
  - Solvent evaporation: water-immiscible solvent ($CHCl_3$, DCM)
  - Nanoprecipitation: water-miscible solvent: (methanol, THF, acetone)
- Aqueous solvent: PBS

Materials and Equipment:

- 1.5 mL microcentrifuge tubes
- 4 mL glass vial (w/ cap)
- Small (0.5") stir bar
- Rotovap (if nanoprecipitation used)
- Glass Pasteur pipettes
- Auto-pipettors
- 1 mL syringes
- 0.4 μm syringe filter

Procedure:

Organic/Aqueous Phase Prep

27. Weigh out approximately 10 mg of polymer into 1.5mL microcentrifuge tube
28. Weigh out appropriate amount of drug (often >1:10 drug:polymer ratio) in separate tube
29. Add 0.1 mL organic solvent to polymer tube
    a. Vortex/sonicate to dissolve thoroughly
30. Add contents of polymer tube to tube containing drug
    a. Vortex to dissolve drug and polymer thoroughly and set aside
31. Add 1 mL PBS to glass vial (can scale up, but keep 1:10 organic:aqueous solvent ratio, and 10 mg polymer/mL aqueous solvent)

Micelle Formation

32. Add organic phase dropwise to vigorously-stirring vial of PBS
33. Micelle formation:
    k. Solvent Evaporation: allow to stir overnight (>8h) to allow organic solvent to evaporate
    l. Nanoprecipitation: stir > 10 min, put glass vial on rotovap to remove organic solvent. If volatile solvent is used (e.g. acetone), same technique as solvent evaporation may be used

Filtration

25. Resulting solution should be just PBS + micelles. Although not required, it is recommended that the solution is filtered to remove unencapsulated drug and aggregates prior to use.
26. Take up solution with 1 mL syringe and pass through 0.4 μm syringe filter

27. If planning on long-term storage, freeze NP solution in -80 for 20 min and lyophilize overnight. Otherwise, fresh NPs are ready for use or may be stored in fridge for ~2 weeks.

Clean-up:

12. Collect all glass waste (pipettes, vials, or broken glass) and dispose in the broken glass container (box)
13. Collect all sharps and dispose in the sharps waste container (red box)
14. Collect all solid waste and dispose in the solid waste container
15. Collect all liquid waste and dispose in the appropriate liquid waste container (acetone or halogenated)
16. Clean glassware:
    a. Wash with soap and water
    b. Rinse with acetone and dry in the oven

SUPERNATANT PREPARATION PROTOCOL

Make bacterial growth medium to intoxicate cells: RPMI + 1% casamino acids
+ 10g Casamino acids to 1L RPMI-1640
Filter sterilize with 0.22µm Millex filter vacuum container

Preparation of bacterial supernatants:

1. Day 1: Streak out bacteria on agar plate (+/- required AbX), incubate overnight at 37°C
2. Day 2: Set up overnight culture in RPMI + 1% casamino acids
    a. 50ml conical (set up in triplicate): +15ml RPMI + a single colony
    b. 250ml Erlenmeyer flask: + 50ml RPMI + 3 colonies
    c. 1L Erlenmeyer flask: + 200ml RPMI + 12 colonies
3. Seal for desired oxygenation condition
    a. "Hypoxic": Use stopper
    b. "Aerobic": Leave cap vented with tin foil
4. Put in 37°C shaker for 15 hours (5pm → 8am)
5. Fill 50ml conicals with bacterial supernatants
    a. Keep bacterial supernatants on ice during **all** remaining steps
6. Centrifuge tubes @ 8000xg, 8 minutes at 4°C with a fixed angle rotor
    a. Or 4000xg, 10 minutes at 4°C with a swinging bucket rotor
7. Decant supernatant into new tube, discard bacterial pellet
8. Filter sterilize supernatant with 0.22µM Millex Luer-lok filter attached to a 60ml BD syringe or 0.22µM Millex filter vacuum container for larger volumes
9. Add 15ml of filter sterilized supernatant to Amicon Ultra 50ml concentration tubes; Spin at 4000xg, 45 minutes at 4°C (swinging bucket rotor)
10. Decant flow through; Repeat #9 adding 15ml directly to same filter tube
11. Decant flow through; Spin at 4000xg, **30 minutes** at 4°C (swinging bucket rotor)
    a. Check volume remaining of concentrated supernatant
    b. To standardize supernatant concentration, remove filter tubes when 1.5ml of concentrated supernatant remains
    c. If > 1.5ml remains in the tube, spin for shorter intervals, checking tubes until they reach 1.5ml
12. Pool concentrated supernatants, if using more than one Amicon Ultra filter tube per supernatant condition
13. Filter sterilize supernatant with 0.22µM Millex Luer-lok filter attached to a 10ml BD syringe
14. Aliquot and freeze at -80°C

MC3T3 SUPERNATANT INTOXICATION ASSAY PROTOCOL

Prior to starting experiments:

NOTE:

- **Before doing cell culture work – spray down hood with ethanol.**
- **Before introducing new objects into the cell culture hood, spray down with ethanol.**
- **Ethanol gloves well and always wear a lab coat.**
- **Warm all media that will touch cells to 37 degrees prior to starting work.**

Media Recipe

MC3T3 Media: 1 container of 500mls α-MEM. Two aliquots of 27.5mls of HI-FBS. 5.5mls of Pen/strep. Filter sterilize after adding.

RPMI + 1% CA: 1 liter of RPMI + 10gs of Cassamino acids. Filter Sterilize after adding.

Starting MC3T3s

1. Add 11mls of MC3T3 media to a T75 flask.
2. Remove a mid-passage number (8-9) from liquid nitrogen. Thaw briefly in 37, then immediately split evenly between 3 flasks.
3. Change media every 2-3 days. Allow to grow until 85-95 percent confluent.

Example Timeline:

Intoxication Experiment:

Day 1: Pull out MC3T3s from liquid nitrogen
Day 3: Seed plates
Day 4: Intoxicate Plates
Day 5: Dye plates

Sup preps

Day 2: Streak plate
Day 3: Make 15 hour culture
Day 4: Prep Sups

Seeding MC3T3s

1. To seed around 5 plates, need 2 confluent flasks of MC3T3s.
    1. Pour off media into waste bucket.
    2. Add 5mls of PBS, rock to rinse flask, and pour off into waste bucket.
    3. Add trypsin (2ml for T75).
    4. Incubate at 37 for 5 minutes. Then check for floating cells in the microscope. Incubate for 1-2 more minutes if cells are not all detached.
        i. Alternative method, tap the side of the flask to detach cells.
    5. Add fresh MC3T3media (4mls to each flask). (There are now 6mls total).
    6. Put the 6mls of cells in 15ml conicals and spin for 5 min at 1500rpm, 25 degrees.
    7. Pour off supernatant in cell culture hood in waste bucket.
    8. Add 1ml of fresh MC3T3 media to one tube, resuspend, then using the same media, resuspend the second pellet.

9. In a separate tube, add 50microls of typan blue.
10. To trypan blue, add 50 µLs of resuspended cells
11. Count cells on hemocytometer (add 10 microliters per side).
    i. Total # of cells on both sides *10,000 = cells/ml
    ii. Target is 5,000 cells per well in a 96 well plate.
        1. For 200 microliters per well, this is 25000 cells/ml.
    iii. Calculate amount of media needed for the number of plates being used.
        1. 200µL of media per well*60wells per plate*# of plates=total media needed
    iv. Calculate amount of concentrated cells needed to add to media
        1. Concentration of cell stock*Volume of cell stock=25000cells/ml*desired amount of media
    v. Add calculated amount of cells to calculated amount of media and mix thoroughly.
12. Plate 200 microliters per well using cell culture basin and multichannel pipette.
    i. Outer ring of plate should be filled with PBS instead of cells/media to prevent evaporation.
13. In 12-24 hours, intoxicate cells.

To split cells for later use,

14. Follow procedure to step 5.
15. Then inoculate 3 new T75 flasks with 2mls of cells each.
16. Add 10 mls of fresh MC3T3 media to each flask.

MC3T3 Intoxication

17. Thaw prepared supernatants
18. Calculate amount of media needed per condition
    i. 200microliters *11 wells usually. (10 wells, plus extra)
    ii. Subtract amount of bacterial supernatant that will be added per well.
        1. Typically use 60, 40 and 20 microliters of sup/well
            a. For 60 microliters, subtract 60*11= 660 sup/condition
            b. For 40 microliters, subtract 40*11 = 440 sup/condition
            c. For 20 microliters, subtract 20*11 = 220 sup/condition

        2. So for 1 condition, need 1540 microliters media + 660 microliters of sup
            a. Ex: 60 microliters/well = 1540 media + 660 sup
            b. Ex: 40 microliters/well= 1760 media + 440 sup
            c. Ex: 20 microliters/well = 1980 media + 220 sup
19. Add media + sup to labeled 15 ml conicals.
20. Aspirate off old media from cells in 96 well plates
21. Add 200 microliters of new media/sup mix to each well
22. Incubate at 37 for 22 hours.

Dyeing Plates

23. After 22 hours, mix enough MC3T3 media for all of your plates to have 100 microliters per well (100*60 wells*# of plates-media needed + 100*10wells for a blank).

24. Add to media enough cell titer dye for all of your plates to have 10 microliters per well (10*60 wells*# of plates + 10*10wells for blank) **NOTE: Keep cell titer in the dark, reagent is light sensitive!**
25. Aspirate off media from cells, changing tips between different conditions
26. Add 110µLs of dye/media mix to each well.
    i. If doing 5 plates or less, pipette each well individually, to lessen the amount of reagent needed. If doing a large amount of plates, a multichannel and basin can be used. Be sure to account for extra media needed in steps 23 and 24.
    ii. Be sure to include a row of media in wells that have had no cells in them. This will be your blank when reading the plate.
27. Allow to incubate at 37 degrees for 2 hours.
28. If bubbles are present, spin down plate at 1500rpm for 2 minutes at 25 degrees.
29. Gently vortex plate to make sure dye is well mixed.
30. Read plate in Biotek using A490 program.

Supernatant Preparation

1. Streak out plates for strains of interest.
2. 15 hours prior to prepping supernatant, inoculate 3 colonies of desired strain into a 250ml flask, filled with 50mls of desired media. Grow at 37 in the shaking incubator for **15 hours exactly**.
3. Put fixed rotor on tabletop centrifuge
4. Move 50ml cultures to 50ml conicals; spin @ 8,000xg, 8min at 4°C.
5. Filter-sterilize supernatants using 0.22µM Millex filters on a 60ml syringe and immediately place on ice. All remaining steps are completed on ice.
    1. Optional for use in unconcentrated sup assays: Remove a 2ml aliquot of supernatant, repeat step 5 using a 10ml syringe, and freeze in a screw cap tube.
6. Change rotor to normal, swinging bucket.
7. Add 15ml of sup to Amicon Ultra 50 ml concentration tube
8. Spin @ 4,000xg, 45min at 4°C. Dump the flow through in the bottom into waste.
9. (Repeat step 7 and 8)
10. Repeat step 7 (Spin @ 4,000xg at 4°C for around **30** minutes. Remove supernatants that are at desired concentration. Repeat short spins (3-5 minutes) so all sups are equally concentrated.
11. Repeat step 5 using a 10ml syringe.
12. Freeze sups at -80°C